

# Lawrence Berkeley National Laboratory

## Recent Work

### Title

Studies of Surfaces Using Optical Sum-Frequency Generation

### Permalink

<https://escholarship.org/uc/item/37z9p0sr>

### Author

Hunt, J.H.

### Publication Date

1988

c.2

Center for Advanced Materials

# CAM

RECEIVED  
LAWRENCE  
BERKELEY LABORATORY

APR 19 1988

LIBRARY AND  
DOCUMENTS SECTION

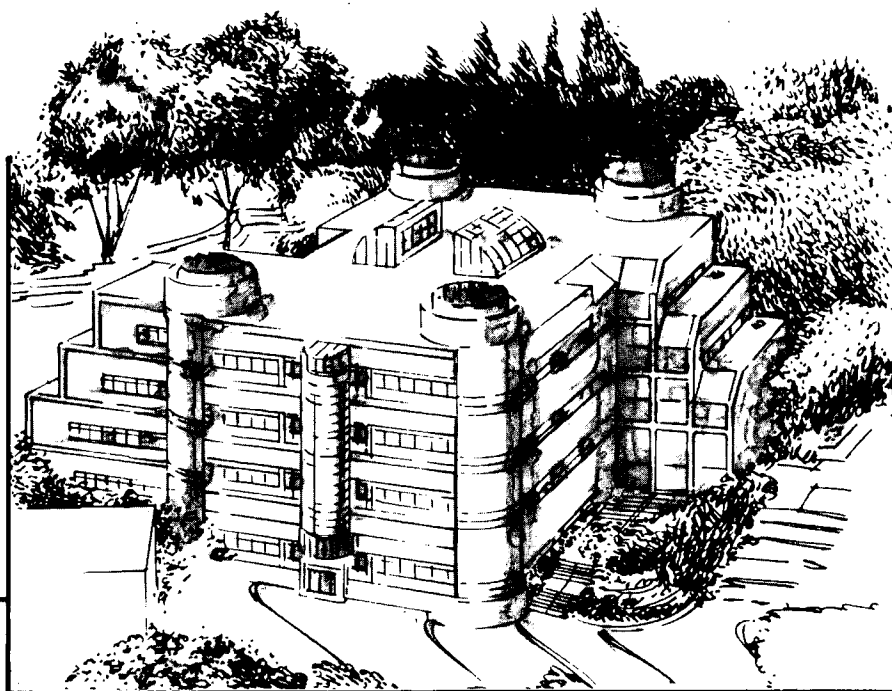
## Studies of Surfaces Using Optical Sum-Frequency Generation

J.H. Hunt  
(Ph.D. Thesis)

January 1988

### TWO-WEEK LOAN COPY

*This is a Library Circulating Copy  
which may be borrowed for two weeks.*



## Materials and Chemical Sciences Division

### Lawrence Berkeley Laboratory • University of California

ONE CYCLOTRON ROAD, BERKELEY, CA 94720 • (415) 486-4755

LBL-24692

c.2

## **DISCLAIMER**

This document was prepared as an account of work sponsored by the United States Government. While this document is believed to contain correct information, neither the United States Government nor any agency thereof, nor the Regents of the University of California, nor any of their employees, makes any warranty, express or implied, or assumes any legal responsibility for the accuracy, completeness, or usefulness of any information, apparatus, product, or process disclosed, or represents that its use would not infringe privately owned rights. Reference herein to any specific commercial product, process, or service by its trade name, trademark, manufacturer, or otherwise, does not necessarily constitute or imply its endorsement, recommendation, or favoring by the United States Government or any agency thereof, or the Regents of the University of California. The views and opinions of authors expressed herein do not necessarily state or reflect those of the United States Government or any agency thereof or the Regents of the University of California.

Studies of Surfaces Using Optical Sum-Frequency Generation

Jeffrey H. Hunt

Ph.D. Thesis

Lawrence Berkeley Laboratory  
University of California  
Berkeley, California 94720

January 1988

This work was supported by the U.S. Department of Energy  
under Contract Number DE-AC03-76SF00098.

# Studies of Surfaces Using Optical Sum-Frequency Generation

Jeffrey H. Hunt

## Abstract

This thesis contains the first series of experiments in which sum-frequency generation (infrared-visible) was used as probe of molecular species at interfaces. The fact that the process is a second order non-linear optical process causes the technique to be surface specific when used at an interface between two centrosymmetric media. The resonant enhancement of  $\chi^{(2)}$  that occurs when the infrared input is tuned through a vibrational resonance allows one to determine the vibrational spectrum of the species adsorbed to the surface. Under certain conditions, the polarization dependence of the spectrum can be used to deduce the molecular orientations of the species at the interface.

Since the second-order susceptibilities are quite small, the laser system used must simultaneously produce an intense fixed-frequency visible pulse and an intense tunable IR pulse. The laser system designed and constructed for this purpose uses an amplified single pulse selected from the output train of a active/passive mode-locked Nd:YAG oscillator. The pulse contains sufficient energy to generate both an intense visible pulse via second-harmonic generation and an intense infrared pulse via optical parametric amplification.

The first experiments were performed on series of alcohols at an air-glass interface. These experiments demonstrated that the basic technique produced spectra several orders of magnitude above the bare glass background. Although the spectra did not extend far enough into the infrared to uniquely identify the adsorbed species, the spectra were quite distinct and were correlated with spectra taken in bulk samples.

The technique was used to examine the spectra of a Langmuir film (air-water

interface) of pentadecanoic acid at several surface densities. It was found that in the high density phase, the molecular hydro-carbon tails were fully extended and aligned nearly normal to the surface. At lower densities, the tail was free to bend and evidence of trans-gauche conformations was observed. The experiment makes use of the ability of sum-frequency generation to do in-situ spectral measurements not possible with other techniques.

Difference-frequency generation was discussed as an alternative to sum-frequency generation when the desired infrared frequency cannot be produced at the intensities needed for sum-frequency generation. The subsequent detection of the difference-frequency generation's infrared output via up-conversion (optical mixing) was discussed. A detection apparatus using  $\text{LiIO}_3$  was demonstrated which had sufficiently low noise signal and sufficiently high conversion efficiency to be able to detect the signal levels produced in a difference-frequency generation measurement. The use of  $\text{AgGaS}_2$  was discussed. Also, the use of KTP as an up-conversion crystal was demonstrated for the first time.

## ACKNOWLEDGEMENTS

Over the past few years, a Shen group tradition seems to have been established whereby the acknowledgements section of each thesis becomes an avenue for each finishing Ph.D. student to provide a stream of consciousness of his feelings at the time of graduation. This tradition may be broken one day. It will not be broken by me.

I cannot thank my advisor, Y. Ron Shen, enough. He has seen me all the way from a fledgling newcomer to a grown-up scientist. I will remember him for his patience, clarity of thinking, and his uncanny ability to examine a complex problem in its simplest and most understandable physical form. Having started to go out into the scientific community and seeing how competitive it can be, I can appreciate why he always pushes his students to be perfectionists in their understanding of a problem. I will always try to be as demanding of myself as he has been of me.

If Ron is first on this list, Ruilin Ma is second. Many group members never quite understood the high volume (literally) relationship I had with Ruilin, especially when someone had to pry our hands off of each others necks. But Ruilin appeared at a time that, in retrospect, proved to be the turning point in my time here. His inexhaustible enthusiasm and love of work made it impossible to be unmotivated in the laboratory. He's the sort of person who, once interacted with, can never be forgotten.

What can I say about Philippe Guyot-Sionnest? If Ruilin's presence started me moving, Philippe threw me into high gear. More important than any physics I have learned in discussions with him, I learned from Philippe what might be called the psychology of winning in the laboratory. He also has come to be a dear friend and has provided me with some wonderful memories. ( Don't worry, I won't tell anyone about doing the Viennese waltz down the Birge basement hallway at 4 A.M.)

More recently, Rich Superfine has been deemed the inheritor of what has become

known as "Jeff's laser". Rich is a pretty neat guy to work with and I hope he has as much fun with the laser as I did.

I would like to thank the gentlemen of the physics department machine shops and electronics shops with whom I've worked. There have been many rush jobs often done without the benefit of mechanical drawings or schematics, but always finished in a timely manner and finished correctly. On a project of the technical massivity (so to speak) that this laser was, there are too many people involved to list all of them here individually, but they know who they are, and more importantly, I know who they are, and I will always remember them kindly.

Thanks to Rita Jones for the various tasks she has performed over the years. Thanks to Huanan Zhu for getting me started and for teaching me basic electronics. Thanks also to the various Shen group members I've interacted with over the years, not only professionally, but also as friends. I would like to specifically mention Hui Hsiung, Harry Tom, and Xiang-Dong Zhu (who will always be X.D. to me) for being especially sweet. They were always willing to drop what they were doing to talk about things in the lab or life in general when things seemed to be going particularly badly.

I want to thank my purchasing agent / dance partner / girlfriend / fiancée / wife / soulmate, Rebecca, for bringing so much love into my life. She, more than anything or anyone, has encouraged and helped me to find new meaning in my existence. She has also helped me discover a different side of myself that I honestly didn't think existed.

Thanks to Mary Donaghue (wherever you are) for suggesting to me on a very cold Cambridge morning in February of 1979 that I might like Berkeley.

Lastly, I would like to thank to God / mother nature / or whatever higher order that may exist in the universe for allowing the microscopic properties of a Langmuir film of PDA to be probe-able by surface sum-frequency generation.



## Table of Contents

	PAGE
I. Introduction	1
References	3
II. Laser System	4
A. Introduction	4
B. Oscillator	4
1. Principles of Operation	4
2. Elements Composing the System	9
3. Technical Operation	10
4. System Performance	14
C. Single Pulse Selector	15
1. Principles of Operation	15
2. Elements Composing the System	17
3. Technical Operation	21
4. System Performance	23
D. Double Pass Amplifier	23
1. Principles of Operation	23
2. Elements Composing the System	24
3. Technical Operation	24
4. System Performance	25
E. Optical Parametric Amplifier	26
1. Principles of Operation	26
2. Elements Composing the System	30
3. Technical Operation	31
4. System Performance	34

	PAGE
F. Second Harmonic Generation	35
1. Principles of Operation	35
2. Elements Composing the System	37
3. Technical Operation	37
4. System Performance	38
G. Integrated System	39
References	41
Figure Captions	43
Figures	45
III. Introduction to Sum Frequency Generation: Spectroscopy of Alcohols at Air-Solid Interfaces	54
A. General Considerations	55
B. Experimental Set-Up	61
C. Resulting Data	62
D. Interpretation	63
References	65
Figure Captions	66
Figures	67
IV. Sum Frequency Generation Spectroscopy of Pentadecanoic Acid at an Air/Water Interface	70
A. Introduction	70
B. Theoretical Considerations	70
C. Experimental Considerations	72
D. Interpretation I: High Density Case	73
E. Interpretation I: Low Density Case	79

	PAGE
F. Conclusion	81
Tables	82
References	84
Figure Captions	85
Figures	86
V. Difference Frequency Generation and Up - Conversion	90
A. Introduction	90
B. Experimental Set-Up	95
C. Results	96
D. Other Crystals	98
1. AgGaS <sub>2</sub>	98
2. KTP	100
E. Conclusion	106
References	107
Figure Captions	109
Figures	110
VI. Conclusion	118
References	120

## I. Introduction

Second harmonic generation (SHG) has been well established as a versatile surface-sensitive probe.<sup>1</sup> It has been used to study electrochemical processes at electrode surfaces, molecular adsorption and desorption at metal and semiconductor surfaces, orientational phase transition of molecular monolayers on water, surface reconstruction and epitaxial growth, and so on. More recently, it has been employed as a tool to monitor monolayer polymerization and other surface reactions,<sup>2</sup> as a means to probe polar order of molecules at interfaces,<sup>3</sup> and for the measurement of molecular nonlinearity.<sup>4</sup> While most surface techniques are restricted to the solid/vacuum environment, SHG is applicable to any interface that is accessible by light. Because it is an optical technique, SHG is capable of in-situ measurements with high temporal, spatial, and spectral resolutions.

The resonant behavior of  $\chi^{(2)}(2\omega)$  can provide spectroscopic information about a surface or molecules adsorbed at the surface.<sup>5</sup> This has been demonstrated in a number of cases. However, since the optical wavelengths involved in the surface SHG experiments are generally in the .2-1  $\mu\text{m}$  range, only electronic transitions of the molecules or surface structure can be probed. They usually have relatively broad bandwidths, making SHG not particularly useful for identification or selective monitoring of surface molecular species. Vibrational spectroscopy is more suitable for selective studies of adsorbed molecules and their interaction with the substrate. Unfortunately, vibrational modes appear in the infra-red (IR) range, and SHG in this part of the spectrum is not practical because of the poor sensitivity of photodetectors at the IR wavelengths. This problem can be solved by using IR-visible sum-frequency generation (SFG).<sup>6</sup>

In the SFG process, the IR input beam is tuned through the vibrational resonances, and the visible input beam up-converts the excitation to a sum-frequency output also in the visible, which can then be detected by photomultipliers. As a second-order process, SFG has all the advantages of SHG for surface probing, but in addition, allows the studies of

surface resonant excitations in the IR.

This thesis will discuss the use of SFG as surface vibrational spectroscopic tool. The various principles will be explained in such a way that someone who wishes to use this technique will be able to do so after reading this thesis. Therefore, explanations will concentrate on intuitive physical arguments. Mathematical expressions will be interjected when they illuminate particular aspects of an idea. Chapter II will discuss all aspects of the laser system including both the principles of operation and the technical procedure needed to make it work. Chapter III will cover the basic theoretical ideas of the SFG technique and give the first results obtained at an air/solid interface. In chapter IV, the technique will be used to study a more exotic system, that of a Langmuir film at an air/ water interface. This system will demonstrate how SFG can determine orientational as well as spectroscopic information. Chapter V will discuss DFG which can be used to study longer wavelength resonances, concentrating on the special detection necessary. Chapter VI will briefly summarize the present SFG status and outline future research directions for the technique.

## References

1. Y. R. Shen, *Ann. Rev. Mat. Sci.* 16, 69 (1986).
2. G. Berkovic, Th. Rasing, and Y. R. Shen, *J. Chem. Phys.* 85, 7374 (1986).
3. P. Guyot-Sionnest, H. Hsiung, Y. R. Shen, *Phys. Rev. Lett.* 57, 2963 (1986).
4. Th. Rasing, G. Berkovic, and Y. R. Shen, *Chem. Phys. Lett.* 130, 1 (1986).
5. T. F. Heinz, C. K. Chen, D. Ricard, and Y. R. Shen, *Phys. Rev. Lett.* 48, 478 (1982).
6. X. D. Suhr, and Y. R. Shen, *Phys. Rev. B* 35, 3047 (1987); J. H. Hunt, P. Guyot-Sionnest, and Y. R. Shen, *Chem. Phys. Lett.* 133, 189 (1987).

## II. Laser System

### A. Introduction

In this chapter, the laser system will be described in detail. Its explanation will be broken down into several sub-systems, those being: 1) oscillator, 2) single pulse selector, 3) double pass amplifier, 4) optical parametric amplifier, and 5) second harmonic generator. Each sub-system will be broken into four sections. Principles of Operation will treat the theoretical operation of the system, emphasizing physical explanations, interjecting mathematical formulae only when necessary. Elements Composing the System will list the optical components in the system, describing their physical characteristics and explaining their individual operating behavior when needed. Technical Operation will be a hands-on type of explanation which will list step-by-step instructions to aid the system user in the alignment of the optics in question. Performance of the System will give a description of the output characteristics of the sub-system and explain any day-to-day maintenance advisable for most reliable laboratory use.

### B. Oscillator

#### 1. Principles of Operation

The oscillator is an active/passive mode-locked Nd:YAG laser. The basic design is described in a paper by Kortz.<sup>1</sup> It combines the best features of passive and active mode-locking. It produces pulses that are bandwidth limited, while giving good shot-to-shot stability in the amplitude of the output train envelope. Being a pulsed system, it also produces much larger energies per pulse than are produced in a cw mode-locked system.

In order to understand the oscillator's principles of operation, one must first understand the operation of both the purely passively mode-locked and purely actively mode-locked system. The concept of mode-locking is described as follows.<sup>2</sup> All lasing mediums have a certain bandwidth which can sustain oscillation. The actual frequencies

which an oscillator can support are determined by the longitudinal modes of the cavity in which the mediums are placed. The longitudinal restriction can be described alternately by saying that the cavity only will support frequencies subject to the constraint that the cavity length be equal to integral multiples of the  $1/2$  wavelength. That is,  $N(\lambda/2)=L$ , where  $\lambda$  is the laser wavelength in question,  $L$  is the cavity length, and  $N$  is an integer. Normally, these longitudinal modes oscillate with random phases. However, if the phases can be made equal, then the intensity distribution inside the cavity will cancel out in all places except for a small temporal area which is limited by the bandwidth of the pulse.

One can examine this mathematically by expressing the electric field of the cavity lasing as a sum over all the longitudinal modes in the lasing bandwidth. Specifically,

$$E(x,t)=\sum E_i \cos(k_i x - \omega_i t + \phi_i), \quad (1)$$

where the sum runs over all the  $i$  frequencies within the lasing bandwidth. Suppose one imposes the modelocking condition, that all the  $\phi_i$  be equal. The summation over a large number of  $\omega_i$  will cause  $E(x,t)$  to cancel out everywhere except for a small region near  $k_i x - \omega_i t + \phi_i = 0$ , the size of this region being determined by the number of longitudinal modes that contribute. This short pulse results from "locking" the modes of the laser cavity together. Consequently, the resulting intracavity lasing is actually one short pulse which is being reflected back and forth between the two mirrors inside the cavity. Each time this pulse reflects off the output mirror, a certain amount exits the cavity, giving rise to the pulse train associated with a mode-locked system. Obviously, the output pulses will be separated in time by the cavity round trip time.

Of active and passive mode-locking, the former is conceptually easier to understand and will therefore be explained first. In the theory of active mode-locking, the basic model assumes a periodic loss modulation. In the case about to be described, the modulation is being generated by a standing wave acousto-optic modulator. This device is driven by an rf



$\sin(\omega_{\text{rf,mod}} t)$  modulation. The intensity of the light diffracted out of the cavity,  $D_{\text{mod}}(t)$ , is proportional to the square of the rf driving field.<sup>3</sup> Consequently,  $D_{\text{mod}}(t)$  is given by<sup>1</sup>

$$D_{\text{mod}}(t) = a \{ \sin^2[(\omega_{\text{rf,mod}} t)] \} \quad (2)$$

Since this function will have two maxima during one period of the rf drive modulation, (maximums occur at  $\omega_{\text{rf,mod}} t = \pi/2$  and  $\omega_{\text{rf,mod}} t = 3\pi/2$ ), the rf drive frequency is set to 1/2 the desired optical modulation frequency. The desired optical modulation frequency is determined by the round trip time in the cavity. Consequently,  $2\omega_{\text{rf,mod}} = \omega_{\text{Res}} = 2\pi(c/2L)$ , where  $L$  is the cavity length. Since the transmitted light is given by  $T_{\text{mod}}(t) = 1 - D_{\text{mod}}(t)$ , the transmitted light is given by

$$T_{\text{mod}}(t) = 1 - D_{\text{mod}}(t) = [1 - (a/2)] + (a/2) \cdot \cos(\omega_{\text{Res}} t). \quad (3)$$

Note that in this expression the modulation depth is  $a$ . (Modulation depth is the maximum fraction of light intensity that is diffracted.) After  $N$  round trips in the cavity, the transmission function that is formed will be equal to  $[T_{\text{mod}}(t)]^{2N}$ . If the full width half-maximum of the "window" formed by this function is  $\Delta t_a$ , then

$$\{T_{\text{mod}}[t = (1/2)\Delta t_a]\}^{2N} = .5 \quad (4)$$

Using equation (4) in equation (3) and solving, one finds

$$\Delta t_a = (1/\pi) (\Delta t_{\text{Res}}) \arccos\{(2/a)[(0.5)^{1/(2N)} - 1] + 1\} \quad (5)$$

where  $\Delta t_{\text{Res}} = 2\pi/(\omega_{\text{Res}})$ . In a typical solid-state laser system, approximately  $10^3$  round trips are required for the cavity radiation to evolve from noise to the point where a cavity pulse is formed.<sup>4</sup> This implies  $N = 10^3$  in equation (5). Suppose one assumes that the

initial radiation distribution in the cavity is uniform. Then, for a typical modulation depth of  $a = 50\%$ , using equation (5), one finds  $\Delta t_a = \sim 120\text{ps}$ .

The understanding of passive mode-locking in solid-state lasers, greatly improved after a time-domain description was introduced by Letohkov.<sup>5</sup> Passive mode-locking is accomplished by introducing a saturable absorber into the laser cavity. The saturable absorber is a medium, typically a dye, which has a finite single pass absorption (30%) at low intensity values at the laser wavelength. However, the absorption will saturate at higher intensities, to the point where complete bleaching is achieved when the cavity is completely mode-locked.

The introduction of the saturable absorber into the cavity changes the way the initial noise burst evolves into a laser output. The evolution can be broken into three stages, those being linear amplification, non-linear amplification, and giant-pulse formation.<sup>5</sup> The linear amplification stage lasts the longest time and is the conceptually simplest. At this stage, the noise burst, although being amplified, is still in the intensity range where the absorption in the saturable absorber is still a constant value. That is to say, the noise gains amplitude, but the intensity distribution in the cavity is unchanged. In the non-linear amplification stage, the larger peaks in the noise distribution begin to saturate the dye. Since the loss for these peaks will be lower than for the rest of the distribution, they will grow much faster than the rest of the noise. The saturable absorber also begins to temporally narrow the noise pulses. In the giant pulse formation stage, the intensity reaches a point where it completely saturates the absorber. At this point all the energy stored in the gain medium will go into the circulating pulse. Consequently, the intensity rises very quickly to its equilibrium output level. If the laser is being run in pulsed operation (as is the case in the system described in this chapter), the amplifying medium ultimately is depleted leading to a fall in the intensity. This results in the characteristic envelope on the output train seen in pulsed mode-locked oscillators.

Due to the nonlinear nature of the saturable absorber, an analytical solution is difficult. If one assumes that all the pulse narrowing occurs during the second phase and that

the third phase strictly amplifies the pulse, an analytical solution is possible.<sup>5</sup> However, numerical calculations show that this assumption is incorrect because a considerable amount of narrowing still occurs during the third stage.<sup>6</sup>

The characteristics of the output pulses are also largely determined by intensity-dependent index of refraction effects. There will be a considerable amount of self-phase modulation and chirping of the pulse, in particular by the time the center of the train has been reached. This leads to both temporal and frequency broadening of the pulse.<sup>7</sup> However, numerical modeling techniques are presently sophisticated enough to describe the evolution of the laser output.<sup>8-12</sup>

Note that one can speak of two thresholds here.<sup>13</sup> The lasing threshold occurs as soon as gain exceeds loss in the cavity. But, there is a second, higher, mode-locking threshold which must be surpassed to bleach the saturable absorber.<sup>13</sup> Since the laser pulse starts from noise, the fact that the lasing medium has sufficient energy to mode-lock some pulses does not guarantee that all pulses are mode-locked. Consequently, there is a tradeoff between the probability of producing a mode-locked output and the size of the fluctuations in the train envelope. Pumping the laser rod with sufficient energy to obtain >90% modelocking probability usually results in 50% fluctuations in the envelope amplitude.

The problem with pure passive mode-locking is the fact that during the linear amplification stage, nothing is being done to shape the intensity distribution. In the active/passive scheme, an active mode-locking element is introduced into the cavity (e.g. an acousto-optic modulator) whose modulation period is tuned to the cavity round trip time. In this case, the system still follows the passive development, but with the following exception. By the end of the linear amplification stage (typically  $10^3$  round trips, a 170 ps window has already been established in the cavity due to the presence of the active modulator. At this point, the saturable absorber only has to narrow the pulse (to nominally 30 ps for YAG). It is as if the laser has a way to "seed" itself with an already partially mode-locked pulse.

When running properly, the envelope fluctuations should be <5%. The reason that

these fluctuations are so small is that the pump energy difference between mode-locking threshold and 100% mode-locking probability is much smaller than the purely passive case ( $7 \times 10^{-3} \text{J}$  difference for active passive as compared to  $7 \times 10^{-1} \text{J}$  for pure passive). As with any laser oscillator, operation closest to threshold provides the most reproducible results.

## 2. Elements composing the system

The optical elements which compose the oscillator are rear mirror/ saturable absorber assembly, Nd:YAG pumping head with laser rod (2 inches long with a .25 inch diameter), acousto-optic modulator, and output mirror. Before discussing the system construction and alignment there will be a brief description of the purpose and construction of each of these individual elements.

The back mirror is a dielectric coated optic which is 99.9% reflecting at  $1.064 \mu\text{m}$  and has a 10 meter center of curvature. The curvature was chosen to provide better stability (compared to a flat mirror) and minimum of beam divergence outside the cavity (compared to that caused by a 3 meter center of curvature).<sup>2</sup> The mirror also forms one surface of the saturable absorber cell, the other surface being formed by a wedged anti-reflection (AR)-coated window. The dye cell formed is spaced by a .010 inch stainless steel spacer between the two pieces. All other pieces in the dye flow system are either stainless, glass, teflon, or viton rubber (the seals on the dye cell). It should be noted that the optics themselves are not sealed to the cell with viton o-rings, but are sealed with indium o-rings. This is necessary to avoid shifting of the optics inside the cell when the dye is flowing. The spacer is actually slotted to insure that the flow will be approximately laminar (i.e. there is no obvious place for turbulent flow to form). The filter system is completely teflon, including the filters.<sup>14</sup> The solvent will dissolve any material other than those listed here, including silicone o-rings or paper or polypropylene filters, resulting in potentially damaging coatings on the optics.

The laser head is composed of the Nd:YAG rod, double ellipse aluminum coated pumping cavity, xenon flashlamps (2 inch arc length and 4 millimeter bore), and tubing to

circulate the cooling water. The lamps and rod are o-ring sealed. The tubing is connected so that the water circulates first past the Nd:YAG rod and then past the lamps. There is a glass tube which surrounds the rod over the length of the head. This tube is present to shield the rod from uv radiation emitted by the flashlamps. This is because the radiation in that wavelength regime does not pump the lasing levels efficiently, but does contribute to heating in the rod potentially leading to thermal distortions and reduction in the stability of the output.<sup>15</sup> There are also two nylon tubes which fit over the faces of the rod. These are extremely important for reducing the beam wander caused by local air currents generated near the faces of the rod when it is warm.

The acousto-optic modulator is a 5mmx5mm Brewster-cut quartz piece which has a thin  $\text{LiNbO}_3$  transducer evaporated onto the side of it. There is a BNC connection for the electrical input and swage water input and output connections. It is situated on a modified NRC commercial mount which allows tilt about two axes for adjustment of Bragg and Brewster angles and lateral displacement in the cavity if needed during alignment.

The output mirror is a 30% dielectric reflector with no curvature and an AR coating on the second surface.

### 3. Technical Operation

Two of the oscillator components, the back mirror/saturable absorber assembly and the acousto-optic modulator (AOM) require some preliminary explanation. This is because each has something external to the cavity connected to it for proper operation.

The saturable absorber cell has an external pump, filter, and dye reservoir which sits in a temperature controlled water bath. All metal pieces are stainless steel and all plastic pieces are teflon, including the filter itself. The circulation of the solvent should be set to approximately 100 ml per minute. When initiating the oscillator alignment, one should start with pure laser grade 1,2 dichloroethane.

The AOM requires a slow (100 to 150 ml per minute) temperature controlled (25°C)

water flow. Without cooling, the crystal will eventually overheat and be irreparably damaged. Also, the frequency of the AOM is a function of temperature. The rf-driver for it is composed of a synthesizer and amplifier. The synthesizer amplitude should be set to approximately .1 volt RMS input to the amplifier. This can be accomplished with some combination of synthesizer output control and in-line attenuation box. Between the amplifier output and AOM there is another electronic box which is used to measure the amount of energy flowing to the AOM (forward setting) and from the AOM (backward setting). The synthesizer frequency (approximately 50 MHz) should be adjusted to minimize the reflected power from the AOM.

To align the oscillator, begin by passing a He-Ne laser (red beam) through all the cavity elements (see figure 1). The saturable absorber cell should be flowing pure solvent and the AOM modulator should be turned off initially. For easiest alignment, the red-beam should be aligned parallel to the invar rods. The iris mounts can slide on the invar rods; this is the best way to check the degree of parallelism.

The AOM is the next focus of attention. With the synthesizer turned on, an acoustic standing wave is established in the modulator. If one looks at the transmitted red beam, it will be seen that some fraction of the beam has been scattered into one or more spots above or below the unscattered beam. These spots correspond to various orders of Bragg scattering. One should adjust the angle until the intensity of the first order spot is maximized. (The first order spot is the one closest to the unscattered beam, either immediately above or below it.) First order Bragg scattering is necessary to obtain the maximum diffraction efficiency.<sup>1,3</sup> It should be noted that when this first order spot intensity is maximized, it will be possible to see a second order diffraction spot and a minus first order spot (first order spot on the opposite side of the unscattered beam), although these will be quite faint. (By changing the angle, one can optimize the scattering into these higher order spots, to the detriment of the first order scattering intensity. It is then possible to see even higher order (third, fourth, etc.) spots. However, since the maximum diffraction efficiency

is obtained for first order scattering, the Bragg angle should be re-aligned to maximize the intensity in the first order spot.) The first order Bragg scattering angle,  $\theta_B$ , is defined such that the angle between the diffracted beam and the undiffracted beam is equal to  $2\theta_B$ . However, this angle is a function of the laser wavelength.<sup>3</sup> Specifically,  $2\theta_B = \lambda/\Lambda$ , where  $\lambda$  is the optical wavelength and  $\Lambda$  is the acoustic wavelength. With an operating temperature of 25°C, the Bragg angle will be 4.45 milliradian for the He-Ne beam. This tilt angle must be scaled from the He-Ne beam (.633 $\mu$ m) to the Nd:YAG wavelength (1.064 $\mu$ m). This Bragg angle will be 7.48 milliradian for the Nd:YAG wavelength. Given the mount construction, this change in angle, 3.30 milliradian, can be accomplished by changing the mount's micrometer setting by .29 millimeter = .011 inch from the angle setting found by using the He-Ne beam. (The mount is constructed so that the angular motion is equal to the micrometer distance motion divided by 3.625 inches = 92.075 millimeter.)

Once the red-beam beam has established the oscillator alignment direction, it should be used to align the back and output mirrors. This is fairly simple as it merely involves positioning reflected spots from each mirror at the He-Ne output. There is one note of caution; there are three reflected spots from the back mirror/saturable absorber assembly caused by the air/glass, glass/saturable absorber, and glass/air interfaces. The reflection spot from the back mirror reflecting surface will be the most diffuse, since it is reflected from a curved surface. This is the spot to be used for alignment.

At this point, the laser can be turned on. One should start at a reasonably large pump energy (45 Joules, 800 volts charging on the power supply) and gradually adjust the back mirror until there is some laser output. Gradually reduce the pumping energy, while adjusting the mirror to maximize the signal. When the minimum pumping energy has been reached, the adjustment should be directed to the output mirror.

The output mirror, AOM, and cavity length adjustment are somewhat coupled in terms of movement of one affecting the performance of others. This means that any adjustments made on these micrometers should be done slowly. Large motions, especially

near the optimum alignment, can only hurt the situation.

The alignment should be conducted in the following manner. First, align the output mirror for maximum signal. Then, align the AOM angle for maximum signal amplitude or stability when the alignment is near the optimum position. Lastly, adjust the translation stage under the output mirror to attain the correct cavity length, trying once again to maximize signal amplitude and stability. Several iterations may be required to achieve proper alignment. When correctly mode-locked, the oscilloscope signal should show a smooth train of pulses with a symmetrical envelope and fewer than 5% fluctuations from shot-to-shot.

Once this level of operation is achieved the saturable absorber dye is ready to be added. Typically, Kodak 9740 Q-switch #1 is used. Its chemical properties are not fantastic (performance usually degrades within a week), but it is inexpensive and weekly flushing of the system will keep the laser functioning well.

(In regard to the preparation of the dye solution, the following procedure has proved to be most reliable. A solution should be prepared which combines 20mg of the dye in 30 ml of solvent. The saturable absorber circulation system can be used to flush the solution once through a clean filter without circulating it past the optics. Change the dirty filter before adding clean solvent to the system again. This once-filtered dye can be added to the pure solvent in the saturable absorber circulation system. This cleaning procedure considerably lessens the probability of burning the optics in the cell.)

Once the laser is running satisfactorily in a mode-locked fashion, gradually add concentrated dye solution to the circulation system. Normally 3 to 5 cc of the concentrate in 870 ml of pure solvent is enough to mode-lock the laser. (This corresponds to concentrations between 2.3mg/liter and 3.8mg/liter.)

Ideally one should add 1cc at a time, increasing the pumping energy to bring the laser back above threshold after each increase in dye concentration. Too much dye will result in a reduction in stability, break-up of the pulse train, and in extreme cases, damage to the optics. Ideally, the laser output train should have 12-13 pulses FWHM and approximately



3-5 mJ per train. Optimally, the pumping energy should be 30 Joules (660 volts charging). It may be necessary to make small adjustments in the output mirror or AOM alignment after adding the dye. Once again, these adjustments should be made slowly. At these intensities, it is also possible to monitor the beam profile with a piece of burn paper. The output mirror should be adjusted so that the roundest possible spot (i.e. TEM<sub>00</sub>) is produced by the oscillator. Also, near mode-locking threshold when optimally adjusted, the cavity length becomes the most sensitive adjustment for improving stability. The output mirror mount is itself mounted on a precision translation stage. The micrometer on this stage is used to fine adjust the cavity length. (One might be tempted to adjust the frequency of the AOM. However, the AOM has a natural frequency to which the synthesizer frequency has been matched. This is described at the beginning of this section. Changing the synthesizer frequency at this point would lead to a loss of mode-locking power, since a larger fraction of the rf driving energy would be reflected from the AOM crystal. Of course, for very small cavity length adjustments, the matching can be done by changing the synthesizer frequency, since there is a finite AOM bandwidth. However, speaking strictly from a technical standpoint, and from the standpoint of experience, it is much easier to find the correct cavity length by adjusting the micrometer mount.) Typically, it must be within 50 micron of the correct length.<sup>1</sup> When optimally adjusted, the power supply voltage range between mode-locking threshold and 100% mode-locking probability is not more than 10 volts as compared to 50 to 100 volts for the purely passive case.

There is one final note in the system adjustment. It may be tempting to run the oscillator far above threshold to compensate for bad alignment. If one wishes to have the best stability characteristics, it is better to spend a little more time aligning the system and run the oscillator near threshold.

#### 4. System Performance

One should expect a 3-5 mJ train of 12-13 pulses with a 10 ns separation, TEM<sub>00</sub> mode

with shot to shot envelope fluctuations of not more than 5%. The oscillator runs at 10Hz and individual pulses are nominally 30ps. The long term stability seems to vary with the amount of daily use, but it is not unreasonable to expect to be able to run the system for several days with no adjustment or several weeks with minimal adjustment. (This assumes a dye change every 5 to 7 days).

### C. Single Pulse Selector

#### 1. Principles of Operation

The output from the oscillator is a train of pulses. To make the most efficient use of the amplifier, one pulse, preferably near the center of the train, should be selected, while all others are discarded. The single pulse selector (SPS) does this job.<sup>16</sup>

The basic idea is very simple. Two crossed polarizers have very low (in principle zero) transmission. If a half-wave plate is introduced between the polarizers, then the linearly polarized light from the first polarizer can be rotated by the  $\lambda/2$  plate to pass through the second polarizer. If the  $\lambda/2$  plate were present only during one of the pulses in the train, then only that single pulse would be transmitted through the second polarizer. In this way, the polarizer- $\lambda/2$  plate-polarizer combination has acted as a single pulse selector.

In this case, the "half-wave plate" is a Pockel's cell which is placed between the two polarizers. The Pockel's cell used is a longitudinal KDP model. Here the electric field is applied along the laser propagation direction, assumed to be the z-direction. It can be shown that, for KDP, there will be an induced difference in the indices of refraction for x and y polarized light given by<sup>17</sup>

$$\Delta n = n_o^3 r_{63} E_z, \quad (6)$$

where  $n_o$  is the ordinary index of refraction,  $E_z$  is the applied electric field, and  $r_{63}$  is the only independent contributing coefficient of the electrooptic tensor  $r_{ij}$ . The tensor is defined

by

$$\Delta(1/n_i^2) = \sum_j r_{ij} E_{ij} \text{ for } i=1 \text{ to } 6 \text{ and } j=1 \text{ to } 3 \quad (7)$$

which relates the changes in the index of refraction  $\Delta n$  to the applied electric field. (The standard convention for the equation of the index ellipsoid in the presence of an electric field is

$$\begin{aligned} & (1/n_1^2)x^2 + (1/n_2^2)y^2 + (1/n_3^2)z^2 + \\ & + 2(1/n_4^2)yz + 2(1/n_5^2)xz + 2(1/n_6^2)xy = 1. \end{aligned} \quad (8)$$

For a crystal of length  $l$ , there will be a path difference  $\Delta n l$  for the two polarizations. This causes a phase difference,  $\delta$ , given by

$$\delta = (2\pi/\lambda)(\Delta n l). \quad (9)$$

The voltage across the PC,  $V$ , is related to the electric field by  $V=El$ . Consequently,

$$\delta = (2\pi/\lambda)(n_o^3 r_{63}) V. \quad (10)$$

A simple derivation shows that for a Pockel's cell placed between two crossed polarizers, the transmission is given by

$$T = \sin^2(\delta/2). \quad (11)$$

The transmission equals unity when  $\delta = \pi$ , which implies a  $\lambda/2$  rotation, meaning that the input polarization is rotated by  $90^\circ$ . The voltage required for this, called the half-wave

voltage, is

$$V_{1/2} = \lambda / (2 n_o^3 r_{63}) \quad (12)$$

and the transmission can then be written

$$T = \sin^2[(\pi/2)(V/V_{1/2})]. \quad (13)$$

A simple plug-in gives  $V_{1/2} = 6.6\text{KV}$  for a 1cm KDP crystal. (For KDP  $r_{63} = 10.5 \times 10^{-6} \mu\text{m/volt}$ .) If an electronic pulse with amplitude equal to the half-wave voltage and duration less than or equal to the pulse separation is put across the PC, then only one pulse will pass through the second polarizer. This is how a single pulse is selected.

## 2. Elements composing the system

The pulse selector is composed of two polarizers, a Pockel's cell, a triggering photodiode and the power supply to form the voltage pulse.

The two polarizers are calcite Glan air-spaced polarizers. Calcite is a birefringent crystal having different indices of refraction for polarizations parallel or perpendicular to the optic axis.<sup>18</sup> In the middle of the polarizer there is an air gap. The crystal is cut at such an angle that s-polarized light is totally internally reflected at this air gap and is lost out the side of the prism, while p-polarized light is transmitted across the air gap, due to the differing refractive indices. There are low power versions of this type of prism which are glue-spaced, but these are not suitable for use with the high-intensity pulses produced by a mode-locked system.

The Pockel's cell (PC) is a dual-KDP crystal, impedance-matched design, manufactured by Interactive Radiation. This PC is meant to be used as an element "in-line" with a 50 ohm coaxial cable. That is, the design assumes that an electrical pulse is produced

in a power supply and sent through the PC and down a long coaxial cable to a 50 ohm terminating resistor. The presence of two crystals drops the half-wave voltage at 1.064  $\mu\text{m}$  from 6.6KV, typical for a single crystal PC, to 3.3KV. In the generation of nanosecond duration, high voltage pulses, this greatly simplifies the design of the PC power supply.

The triggering photodiode is an FND-100 manufactured by EG&G. The crucial parameter in choosing this photodiode is the fact that the pulses in the train are easily resolved by this photodiode. The connection from the photodiode to the power supply is a 50 ohm coaxial cable which is hard wired directly to the photodiode to prevent any possible impedance mismatch.

The commercial pulse forming power supply is manufactured by Lasermetrics. In order to understand the principle of the pulse formation, one must understand some simple transmission line theory. In particular, one must examine the behavior of a voltage wave when it encounters an impedance discontinuity.<sup>19</sup> Consider the situation in figure (2). A voltage wave  $V$  travels from the left on a transmission line of impedance  $Z_0$ . It encounters a junction to another line of impedance  $Z_1$ , not equal to  $Z_0$ . (In this power supply design,  $Z_0$  will be set equal to  $Z_1$ . However, the reflection and transmission coefficients at an impedance mismatch will still be needed. Consequently, they are derived here.) There will be a reflected wave  $V_r$  and a transmitted voltage wave  $V_t$ . Since the voltage must be continuous across the junction,

$$V_0 + V_r = V_t \quad (14)$$

Conservation of current requires

$$V_0/Z_0 = V_r/Z_0 + V_t/Z_1 \quad (15)$$

The reflected and transmitted voltages can be re-expressed in terms of reflection and

transmission coefficients,  $V_r = RV_o$  and  $V_t = TV_o$ . These reflection and transmission coefficients can be found using equations (14) and (15). One finds

$$R = (Z_1 - Z_o)/(Z_1 + Z_o) \quad (16a)$$

$$T = 2 Z_1/(Z_1 + Z_o). \quad (16b)$$

The operation of the power supply is as follows. (See figure 2. The basic schematic of the discharge cables and Krytron are shown at the top of the figure.) Initially, the power supply charges a coaxial cable to a voltage  $V$  (see figure 2a). (Figures 2 (a)-(e) show the voltage on the charged cable and output cables at various times in the evolution of the output pulse. The charged cable voltage is to the right of the arrow. The output cable voltage is to the left of the arrow.) This cable, which will be called the charged cable, has an impedance  $Z_c$ . The Krytron suddenly shorts the charged cable to another cable which will be called the output cable. The output cable has an impedance  $Z_o$ . After the charged cable is connected suddenly to the output cable, a voltage wave  $V_c$  will be launched down the charged cable and an output wave  $V_o$  will be launched down the output cable. Since the voltage must be continuous across the connection,  $V - V_c = V_o$ . Conservation of current requires  $V_c/Z_c = V_o/Z_o$ . Solving these equations leads to  $V_o = V(Z_o)/(Z_o + Z_c)$ . Of course, in this circuit,  $Z_c = Z_o$ . So the output voltage wave will be  $V_o = V/2$  and the wave traveling down the charged cable will be  $V_c = V/2$ . The situation can be visualized by examining figure (2b). At this point, the output voltage wave has been started and it has an amplitude  $V/2$ . There is a voltage wave traveling down the charged cable. This voltage wave causes the voltage in the cable to drop from  $V$  to  $V/2$ . When this charged cable voltage wave reaches the end of the charged cable it encounters an open end (see figure 2c). At this point, the reflection coefficient can be calculated using equation (16). Essentially,  $Z_1$  is infinite. Consequently,  $R = 1$ , and the voltage wave is reflected maintaining its amplitude. On the return trip (see figure 2d) the voltage falls from  $V/2$  to 0. When the charged cable

voltage wave reaches the Krytron again, it encounters a transmission line junction where  $Z_0 = Z_1$  since the cables are of equal impedance. Using equation (16) gives  $R = 0$  and  $T = 1$ . This causes the termination of the output pulse (see figure 2e). Since the cable is completely discharged and since there is no reflected pulse, the process is finished.

One should note that in this process, the output pulse generated will have an amplitude  $V/2$ , where  $V$  is the voltage initially put on the charged cable, and will have a duration equal to the round trip travel time of the voltage wave in the charged cable. Consequently, the charged cable is the one which controls the temporal length of the pulse sent to the Pockel's cell.

The basic design can be built by anyone. However, since this is being used for a single pulse selector, there are several strict constraints that are placed on the power supply. The selector should select the same amplitude pulse each from each train. This means that the power supply must be able to trigger from the rising edge of the pulse train, since the pulses here provide the best amplitude discrimination. Since the pulse train is approximately ten pulses in duration, it must have a turn-on (trigger delay) time of not more than 20 nanoseconds (the pulse separation is 10 nanoseconds). It must provide the same relative delay time between trigger and output pulse. (In the terminology of the power supply, it must have a jitter of less than 1 nanosecond.) Ordinary specifications provided by EG&G on their Krytrons list delay times of 100 nanoseconds and jitter times of 5 to 10 nanoseconds. These figures are utterly unacceptable for any kind of reliable pulse selection.

The main purpose of the supply is to provide a low voltage (300 volts) pre-trigger pulse to the Krytron. This increases the density of the plasma inside the Krytron. Since the higher density plasma provides a better defined electrical discharge path for the Krytron, the higher density plasma leads to a lower delay time and smaller jitter time.<sup>20</sup> (The high density plasma state cannot be maintained in a DC fashion. The Krytron would be damaged permanently if this were attempted.) Consequently, the actual trigger provided by the photodiode signal leads to a very low turn-on time (20ns) with very low jitter (<1ns).<sup>19</sup>

Because of the short turn-on time, the rising portion part of the pulse train can be used to select a pulse from the maximum of the train. Consequently, the stability is no worse than, and optimally better than, the stability of the train envelope.

### 3. Technical Operation of the System

The performance of each of the elements in the single pulse selector depends critically on alignment. Misalignment of one can lead to poor discrimination in the selection process, interference fringes in the transmitted mode, or even damage to the optics themselves. Following a standard alignment procedure can avoid these problems (see figure 3).

Because of the nature of the Glan prisms, the correct use is very dependent on the tilt of the polarizers. A tilt too far in one or the other direction can result in both polarizations being reflected or transmitted. In fact, if the user is new to these prisms, it is a good idea to get a little practice with a He-Ne beam first to get a "feel" for the alignment.

The two prisms should be aligned initially without the PC, allowing enough room to insert the PC later. The first prism should be aligned for maximum transmission, the second for maximum rejection. The most difficult aspect of the alignment is the assurance that a half-wave rotation will change the beam in the second prism from reflected out the side to transmitted through. Thus it is important to use a half-wave plate to check to see that this happens. The most likely problem is that the transmitted mode will have fringes due to poor alignment. (These fringes are caused by multiple reflections in the air gap of the improperly aligned Glan prism. If one has practiced the alignment with the He-Ne laser, these fringes will be familiar, since they can be seen with that laser as well.) Burn paper should be used to make sure that the input mode quality is conserved after passing through both prisms. The rejection ratio of the prisms should be checked via a photodiode. They should have a rejection ratio of at least  $10^3$ .

When the level of transmission and rejection are both correct and the transmission is



still a good quality mode, the Pockel's cell should be put in place. Initially, the cell should be aligned so that the entrance and exit windows are perpendicular to the laser path. The two rotation axes should be adjusted to minimize the transmission (it is best to use a photodiode for this alignment). One should make adjustments slowly. Too large an adjustment may lead to a small (and seemingly correct) transmission which will actually be caused by a complete misalignment of the PC. There should be an alignment position which produces a clear minimum transmission in both rotation adjustments.

To check that it is rotating the polarization properly, a DC 3.3 KV signal should be applied to the PC. (The DC voltage should be applied through a large(>10M ohm) resistor so that no current can go through the crystal. A DC voltage should never be left on the crystal for long periods of time.) The transmitted beam should be as good a mode quality as when rotated by the half-wave plate. If it is not, the PC alignment may be slightly adjusted to improve the mode. However, one should bare in mind that large adjustments will ruin the rejection ratio.

After removal of the DC supply, the coaxial cables should be connected to the PC. The output cable from the power supply to the PC should be kept as short as possible to minimize pulse delay. (See figure 3.) The exit cable should be made fairly long (10meters) so that any reflected electrical pulse will arrive at the PC long after the laser train has passed. Note that only the charging cable on the Lasermetrics power supply determines the temporal length of the HV electrical pulse which causes the 90° polarization rotation. That pulse length is defined by the coaxial charged cable located on the commercial power supply as described at the end of section 2. The triggering photodiode should be placed at the rejection window of the second polarizer, since this rejected train provides the trigger to the power supply.

The actual power supply technical adjustment (setting the trigger level, setting the pre-trigger window, etc.) is explained very clearly in its manual will not be described here.

#### 4. Performance of the system

With the introduction of the Lasermetrics commercial HV pulser, the SPS, which used to be the least reliable subsystem of the laser setup, is now operable with almost no maintenance. An overall rejection ratio of  $10^3$  with good mode quality is easily maintained. Only the KN-22B Krytron (EG&G) must be replaced periodically. (Lasermetrics specifications list the Krytron lifetime at  $10^6$  flashes, but ours has operated up to  $8 \times 10^6$  flashes, although with increased jitter above  $3 \times 10^6$ .)

#### D. Double Pass Amplifier

##### 1. Principles of Operation

After single pulse selection, the  $1.064 \mu\text{m}$  pulse has approximately .5mJ when selected from the center of the pulse. The single pump pulse must contain approximately 25mJ in order to operate the second harmonic generator and the optical parametric amplifier. This can be accomplished by a high gain, double passed amplifier system.

Sufficiently high pumping energy, should be able to create sufficient inversion in the amplifier rod to obtain a single pass gain of 7.<sup>21</sup> In an amplifier the small signal gain coefficient  $g_0$  is related to the stored energy by<sup>2</sup>

$$g_0 = \beta E_{st} \quad (17)$$

For YAG,  $\beta = 4.73 \text{ cm}^2/\text{J}$ , a value much higher than either Nd:glass or ruby.<sup>2</sup> In the design of an amplifier, a decision must be made as to whether to run the amplifier in the exponential (small signal) or linear (large signal) gain regime. The advantage to the former is that it gives the largest gain. The advantage to the latter is that it transfers the largest amount of stored energy to the amplified pulse. To operate in the linear regime, the input fluence must exceed the saturation energy,  $E_s = 1/\beta = 200 \text{ mJ}/\text{cm}^2$ .<sup>2</sup> Given that the input pulse is .25mJ, the exponential gain regime must be used in this case. The single pass gain is given by  $G =$

$\exp(g_0 L)$ , where  $L$  is the crystal length. For the present case,  $L = 7.62$  cm. If one needs  $G = 7$ , then  $g_0 = .255\text{cm}^{-1}$ . Consequently,  $E_{st}$  must equal  $.054\text{J/cm}^3$ .

## 2. Elements composing system

The design of the amplifier head is simply a larger version of the oscillator head. The double ellipse is larger diameter and longer. The lamps are longer (3 inches) and of larger bore (7 millimeter). The rod is longer (2.9 inches) and wider (.335 or .375 inch). The rod is anti-reflection coated with a slight wedge (one degree) to avoid any stray reflections.

## 3. Technical Operation of the System

The initial amplifier alignment should be done at low pumping power. The pumping power should be increased only when one is sure that the rod is properly aligned.

Before starting the alignment, the cylinders which cover the ends of the rod must be put into place to insure that there will be no thermal distortion of the beam. Without these tubes, the beam will be diffuse, will fluctuate in shape, and will suffer drastic wandering as it propagates through the rest of the optics. (Beam wanders will be larger than 1 milliradian without the tubes.)

It is best to align a single pass through the rod first (see figure 4). The IR telescope is useful when starting. (The infrared "telescope" manufactured by FJW industries is actually an IR imaging tube and image intensifier which allows one to "see" the IR laser beam wherever it scatters off an object's surface.) The electrical flashlamp pumping energy should be increased until there is a clean round burn spot at the exit. The pumping energy needs to be reduced before reflecting the laser for the second pass. (At full power, the double-passed pulse will contain enough energy to do considerable damage to the amplifier rod and/or other optics on the table if it is not properly aligned. Consequently, it is imperative to reduce the amplifier electrical pumping power before reflecting the pulse for its

second pass. That way, the pulse will be at powers which will not damage the optics while the alignment is being completed. Once it is aligned, the amplifier can be set to full power.)

On the second pass, the amplified output must be separated from the path it took on the input to the amplifier. There are two ways to do this. (See figure 4). The system which had been used merely misaligned the second pass through the amplifier, so that the reflected pulse hit a mirror which was placed just to the side of the input path. This way, the amplified spot could be picked off and sent to the rest of the system. Presently, another scheme is being used. Here, the input path passes through a thin film polarizer which transmits a p-polarized input. On the far end of the amplifier, there is a  $\lambda/4$  -plate. Double-passing this plate has the effect of a  $\lambda/2$ -plate. Consequently, the pulse has its polarization rotated  $90^\circ$ , so that the thin film polarizer will now reflect the amplified pulse. In this case, one does not have to spatially resolve the reflected pulse from the input path. The angular separation in the amplifier can be much smaller, so that the path through the amplifier crystal can be much closer to the rod center. This simplifies the alignment. In principle, the reflected path can be exactly coincident with the input path. Since there will be a small transmission through the polarizer, even for optimum alignment, a small misalignment is advisable to prevent any potential feedback problems.

#### 4. Performance of the system

With pumping energies of 140 Joules, there is sufficient inversion created in the rod to generate a single pass gain of 7. Using the dimensions of the .375 inch diameter rod, the estimated stored energy is .3J. This leads to an electrical energy to stored optical energy conversion efficiency of .2%. This number is not unreasonable, since the best commercial pumping heads only achieve efficiencies of 1%. Consequently, an input of .5 mJ will result in an output of 25 mJ. This is enough to begin the subsequent nonlinear generation processes in the optical setup.

## E. Optical Parametric Amplifier

### 1. Principles of Operation

The basic physical process used by this optical system is difference frequency generation.<sup>21</sup> Via a second order non-linear process, an intense input at a pump frequency  $\omega_p$  generates two waves at frequencies  $\omega_s$  and  $\omega_i$ , called the signal and idler, such that  $\omega_p = \omega_s + \omega_i$ . On a quantum mechanical level, each input photon at  $\omega_p$  splits into two photons and the resulting frequency constraint is a result of conservation of energy.

From the coupled wave approach, one finds<sup>21</sup>

$$P(\omega_s, z) = (8\pi^3 \omega_s^2 / c^3 n_i n_s n_p) |e_s \cdot \chi^{(2)}(\omega_s = \omega_p - \omega_i) : e_p e_i|^2 z^2 \{\sin^2(\Delta kz/2) / (\Delta kz/2)^2\} \{P(\omega_i) P(\omega_p) / A\}. \quad (18)$$

For large pump intensities, assuming negligible depletion of the pump beam, the signal and idler intensities grow exponentially according to<sup>22</sup>

$$I_s(z) = 2 I_{SO} \sinh^2(\gamma_s z) + I_{SO}, \quad (19a)$$

$$I_i(z) = I_{SO} (2\omega_i/\omega_s) \sinh^2(\gamma z) + I_{SO} (\omega_i/\omega_s), \quad (19b)$$

where  $I_{SO}$  is the spontaneous noise, and where

$$\gamma_s = \{ [32\pi^3 \omega_s \omega_i (\chi_{\text{eff}}^{(2)})^2 / c^3 n_s n_i n_p ] \}^{1/2} \quad (20)$$

and in LiNbO<sub>3</sub>,

$$\chi_{\text{eff}}^{(2)} = 2(d_{15} \sin\theta - d_{22} \sin\theta \sin 3\phi). \quad (21)$$

A simple calculation shows that with a peak intensity of 2 GW/cm<sup>2</sup>, an intensity

which can be generated easily with picosecond pulses, the gain factor  $2\sinh^2(\gamma_S z) = 3.57 \times 10^3$  with a three centimeter interaction length, assuming  $\omega_S = 6400 \text{cm}^{-1}$  and  $\omega_i = 3000 \text{cm}^{-1}$ . For the first pass of the  $\text{LiNbO}_3$  crystal, the approximate value of  $I_{SO}$  is  $3 \times 10^{-4} \text{W/cm}^2$ ,<sup>21</sup> so that the signal will be  $I_S = 1.1 \text{W/cm}^2$  for  $z = 3$  centimeters.

For a type-I phase-matched interaction in a negative uniaxial crystal, the walkoff angle  $\rho$  is given by<sup>23</sup>

$$\tan \rho = \cos(\theta_{PM}) \sin(\theta_{PM}) \Omega, \quad (22)$$

where  $\theta_{PM}$  is the phase matching for the frequencies in question and  $\Omega$  is given by

$$\Omega = \{[n_e^2(\omega_p) - n_o^2(\omega_p)] / [n_e^2(\omega_p) \cos^2(\theta_{PM}) + n_o^2(\omega_p) \sin^2(\theta_{PM})]\}, \quad (23)$$

where  $n_o$  and  $n_e$  are the ordinary and extraordinary indices of refraction at the pump wavelength  $\omega_p$ . For the parametric generation in question,  $\rho = 2^\circ$ . For a pump beam 2 millimeters in diameter, this will limit the effective crystal length to 28 millimeters, assuming that parametric gain ceases to be effective when the pump and signal beams are separated by one beam radius (1 millimeter).

There are several factors to consider in the determination of the frequency bandwidth of the output.<sup>24</sup> Suppose that one modifies equations (12) and (13) to include the effect of a nonzero  $\Delta k$ . In the exponential amplification regime, the gain is proportional to  $\exp(2\gamma_S z)$ , where  $\gamma_S = [(32\pi^3 \omega_S \omega_i / c^3 n_S n_i n_p) (\chi_{\text{eff}}^{(2)})^2 I_p - \Delta k^2 / 4]^{1/2}$ . The amplification will be down by a factor of two when  $\Delta k = 2[\ln(2\gamma_S / z)]^{1/2}$ .<sup>22</sup> For a crystal of 5 centimeters, one estimates a value of  $\Delta k = 1.1 \text{cm}^{-1}$  for half intensity. The phase mismatch corresponds to a frequency variation  $\Delta \nu$  according to the relation  $d\nu/dk = [2\pi(n_{\text{eff},i} - n_{\text{eff},s})]^{-1}$ , where  $n_{\text{eff}} = n + n(d\nu/dn)$ . This depends on the optical dispersion of  $\text{LiNbO}_3$  at the particular wavelength of

operation. For  $\Delta k = 1.1\text{cm}^{-1}$ , one finds  $\Delta\nu = 11\text{cm}^{-1}$  for  $\nu_i = 3000\text{cm}^{-1}$ . The divergence of the beam will lead to a small bandwidth contribution. Suppose the beam has a finite divergence of  $\phi$ .  $\phi$  is equivalent to a variation of the phase matching angle  $(\phi/n_p)$  inside the crystal. This leads to a bandwidth  $\Delta\nu = (d\nu/d\theta) (\phi/n_p)$ , where  $\theta$  is the phase matching angle. At  $\nu_i = 3000\text{cm}^{-1}$ ,  $d\nu/d\theta = 24\text{cm}^{-1}$ . If the beam has a divergence of .3 milliradian, this leads to a bandwidth of  $3\text{cm}^{-1}$ . There is also a small contribution from the pump source. However, the single largest contributing factor is caused by the off-axis k-matching due to the finite beam diameter (see figure 5). It was this fact which led to the large bandwidths ( $100\text{cm}^{-1}$ ) in the earliest parametric amplification experiments.<sup>22</sup>

However, this process which causes the large bandwidths allows one to narrow the bandwidth as well. The infrared which is produced by off-axis k-matching will not propagate colinearly with the pump beam. Since this infrared is produced off-axis it will propagate off-axis. If the output of the first pass is reflected from a mirror and sent back through the  $\text{LiNbO}_3$  again (after approximately 40 cm of propagation), the pump beam, with its smaller divergence, will act as an aperture which allows only a narrow spectral range of the bandwidth to be amplified on the second pass. This allows one to narrow the bandwidth to  $<10\text{cm}^{-1}$ , good enough to do IR spectroscopy.

There exists a finite amount of group velocity dispersion in the  $\text{LiNbO}_3$  crystal. In order to generate the narrowest pulses, the signal and pump pulse should overlap at the entrance of the  $\text{LiNbO}_3$  on the second pass.<sup>25</sup> This can be done with a small (3 millimeter) piece of  $\text{CaCO}_3$ .  $\text{CaCO}_3$ , like  $\text{LiNbO}_3$ , is a negative uniaxial ( $n_o > n_e$ ) birefringent crystal. Because it encounters a higher index of refraction, the e-ray will travel more slowly than the o-ray through either of these crystals. (This is known as group velocity dispersion.) However, the  $\text{CaCO}_3$  crystal can be oriented so that the light polarized as an e-ray in the  $\text{LiNbO}_3$  will be polarized as an o-ray in the  $\text{CaCO}_3$  and vice-versa. This will allow the  $\text{LiNbO}_3$  e-ray to "catch-up" with the  $\text{LiNbO}_3$  o-ray before entering the  $\text{LiNbO}_3$  for the second pass. If the  $\text{CaCO}_3$  crystal's optic axis is oriented normal to the plane defined by the

pump propagation direction and the LiNbO<sub>3</sub> optic axis, its group velocity dispersion will compensate that caused by the LiNbO<sub>3</sub> crystal. (The group velocity dispersion of CaCO<sub>3</sub> will compensate .56 picoseconds per millimeter of crystal. The 6 millimeters of CaCO<sub>3</sub> encountered upon double passing the 3 millimeter crystal will compensate the 3.4 picosecond delay produced in the first pass of the LiNbO<sub>3</sub> crystal.)

After double passing the first crystal, a narrow band pulse of nominally 15ps has been generated, but of small energy (.1nJ). (The 1W/cm<sup>2</sup> pulse will lose a factor of 10 since only ~10cm<sup>-1</sup> of the 100cm<sup>-1</sup> bandwidth produced on the first pass will be amplified on the second pass. This leads to  $I_s = 3.6 \times 10^2 \text{W/cm}^2$  after the second pass, that being approximately .1nJ in a 30 picosecond, 1 millimeter<sup>2</sup> pulse. This is used as a "seed pulse" in the second "amplifier" crystal. The parametric generation process is the same in the second crystal, except instead of starting from IR noise, the process starts with an input at the signal wavelength. The presence of this seed allows a very efficient energy conversion, since  $I_{SO} = 3.6 \times 10^2 \text{W/cm}^2$  in equation(19). With a stronger pump beam (10GW/cm<sup>2</sup>) in the second crystal there is a larger gain factor ( $2\sinh^2(\gamma_s z) = 6 \times 10^6$ ) so that energies on the order of .25mJ at the idler wavelength are possible.

The highest gain is possible only for the  $\Delta k=0$  case. This phase matching is dependent on the indices of refraction which are in turn controlled by the angle of propagation with respect to the LiNbO<sub>3</sub> optic-axis (z-axis). The Sellmeier equations for the LiNbO<sub>3</sub> indices of refraction are<sup>26</sup>

$$n_o^2 = 4.9130 + (1.173 \times 10^5 + 1.65 \times 10^{-2} T^2) / [\lambda^2 - (2.12 \times 10^2 + 2.7 \times 10^{-5} T^2)^2] + \quad (24a)$$

$$-2.78 \times 10^{-8} \lambda^2$$

for the o-ray and

$$n_e^2 = 4.5567 + 2.605 \times 10^{-7} T^2 + \quad (24b)$$



$$+(0.970 \times 10^5 + 2.70 \times 10^{-2} T^2) / [\lambda^2 - (2.01 \times 10^2 + 5.4 \times 10^{-5} T^2)^2] - 2.24 \times 10^{-8} \lambda^2$$

for the e-ray. In these equations, T is the temperature in degrees Kelvin and  $\lambda$  is in nm. The crystal are cut for type-I phase-matching, so that

$$n_p w_p = n_s w_s + n_i w_i, \quad (25)$$

where  $n_s$  and  $n_i$  are ordinary indices of refraction and  $n_p$  is a extraordinary index of refraction. Consequently, the tuning of the IR is controlled by simultaneously twisting the two crystals to change the phase-matched wavelengths and in so doing, change the IR output wavelength.

## 2. Elements composing the system

The system is composed of two 5cm LiNbO<sub>3</sub> crystals cut at 47° with respect to the optic axis, a copper mirror, a 70-30 beamsplitter, a sapphire substrate 1.064μm mirror, a 3 millimeter CaCO<sub>3</sub> crystal, and five 45° mirrors for directing the beam.

Each LiNbO<sub>3</sub> crystal is ~5cm in length and ~2cm in diameter. (The group velocity delay between the idler and laser pulse is 1.5 picoseconds per centimeter for 1.064μm pumping and 3.3μm idler wavelength. If one were to pump the OPA with the shorter pulses produced by a Nd:glass laser, 3 centimeters would already be close to the limitations imposed by group velocity dispersion. For Nd:YAG pulses, the crystals may be longer. However, even in a 5 centimeter crystal the interaction length is limited to 3 centimeters by the walkoff effect (see equation 22).) Each is cut at 47° with respect to the optic axis so that pump propagation parallel to the crystal axis will result in operation at the middle of the IR tuning frequency range (see figure 7).

The copper mirror ( manufactured by SPAWR) is a solid copper piece with a one

inch diameter which has been polished to a sufficiently high optical grade that it can be used as a mirror. It replaced an aluminum coated glass substrate for two reasons. First, the bulk copper led to a much higher damage threshold. Second, the copper has slightly better reflectivity in the infra-red than aluminum does.<sup>27</sup>

The 45° mirrors are used for a delay line for the amplifier crystal pump (4) and for feeding the 1.064μm into the LiNbO<sub>3</sub> oscillator crystal (1) and subsequently seeding the amplifier crystal.

The 70-30 beamsplitter splits the 15mJ input into two pulses. The 30% feeds the "oscillator" half of the OPA and the 70% travels down the delay line to the "amplifier" crystal.

### 3. Technical Operation

There should be an initial He-Ne beam alignment with the two LiNbO<sub>3</sub> crystals, the two 45° mirrors which sit between them, and the sapphire mirror. (See figure 6) (One can do this without the copper mirror in place.) There are two characteristics of alignment to be determined with the red beam. First, the laser must be able to pass all four pieces of optics. Although this might seem trivial, the walkoffs produced in the LiNbO<sub>3</sub> and the displacements produced by the 45° mirrors cause horizontal beam displacements in the plane of the table on the order of several millimeters. Second, the optic (z) axes of the LiNbO<sub>3</sub> crystals should be aligned to lie in the plane of the table in opposing directions (see figure 6) This must be done so that the stepping motor motion maintains the two crystals phase-matched at the same frequency.

Due to the birefringence of LiNbO<sub>3</sub>, passing the unpolarized red beam through the crystal will produce two spots, one e-ray and one o-ray, linearly polarized 90° with respect to one another. The plane which contains these two beams also contains the z-axis.<sup>18</sup> Twisting the crystal about its cylindrical axis can orient these two beams, and consequently the z-axis, to be parallel to the table. After traversing the two mirrors and the other LiNbO<sub>3</sub>

crystal, the two beams should be recombined (the proper orientation for the z-axis will exactly compensate the walkoff of the first crystal). If they are not recombined then there are two possible problems. Either the z-axis of the second crystal is not parallel to the table, in which case there will be 4 spots of varying intensities, or the z-axis is in the same plane but is in the same direction as the first crystal, which will cause the two spots to be farther apart. It is fairly easy to correct either of these problems. The sapphire mirror is also birefringent. It should be oriented so that a polarized red-beam will not have its polarization rotated by passing through the mirror.

The "oscillator" half of the parametric generator can now be aligned. The 1.064  $\mu\text{m}$  which is transmitted through the 70-30 beamsplitter (5mJ) is reflected off the 45 $^\circ$  mirror and through the LiNbO<sub>3</sub> crystal and the CaCO<sub>3</sub> to the copper mirror. (It is easiest to start with the pump propagating parallel to the crystal growth axis.) The position of the beam immediately after reflecting from the 45 $^\circ$  mirror should be set with an iris. The spot reflected from the copper mirror should be aligned to retrace its path back to the iris. The small amount of second harmonic which is produced in the LiNbO<sub>3</sub> crystal overlaps the pump fairly closely and can be used as a rough means to align this reflection. The IR telescope can be used for more accurate determination.

To monitor the IR production, a Ge photodiode must be used since a silicon photodiode response cuts off at 1.15 $\mu\text{m}$ .<sup>28</sup> This photodiode should be placed on the amplifier side of the two 45 $^\circ$  mirrors (note position in figure 5) and should have at least one additional 1.064  $\mu\text{m}$  mirror in front of it to serve as a filter. (The Ge photodiode is sensitive to the 1.064  $\mu\text{m}$ . Since each 1.064  $\mu\text{m}$  mirror does have a finite transmission ( $10^{-3}$ ), care must be taken to eliminate the 1.064  $\mu\text{m}$  hitting the photodiode.) A small tube should be placed around the photodiode to eliminate any stray light reflected from the various optical pieces on the table.

If the reflection is overlapped fairly closely, there should already be some IR signal being produced. The Ge photodiode (which should be mounted on an X-Y translation stage)

should have its position adjusted until the signal is maximized. At this point the fine adjustment of the copper mirror should be done. One must be aware that each time the tilt of the copper mirror is adjusted, the Ge photodiode must be repositioned. For this reason, it is a good idea to note the micrometer readings on the mirror tilt and the corresponding IR signal produced. The optimum tilt should not be too far away from the exact reflection direction. If it seems as though large tilt changes are needed, it is best to go back to the beginning and realign the reflection on the iris.

Lastly, the horizontal tilt ( about the axis perpendicular to the cylindrical axis in the plane of the table ) of the crystal should be checked. Large changes should not be necessary. If it is found that a change in horizontal tilt is necessary, the copper mirror should be fine tuned one more time.

After the oscillator half is aligned, the amplifier side has to be set. The most important aspect of this alignment is to know the path that the IR beam is following. Using the Ge photodiode, two irises should be set to mark the position of the beam. One iris should be next to the 45° mirror and the other should be immediately in front of the amplifier crystal. Since the positioning of these irises sets the overlap of the pump and IR seed pulses in the amplifier crystal, these irises should be positioned with great care.

The amplifier pump beam (1.064  $\mu\text{m}$  reflected from the 70-30 beamsplitter) can now be aligned through the delay line to the two irises. This alignment is fairly easy, but it must be kept in mind that the optical path lengths (for the oscillator and amplifier) must be matched to within a few millimeters [ $15\text{ps} \times (3 \times 10^{10} \text{cm/sec}) = 4.5 \text{ millimeter}$ ]. The oscillator path length should be measured to the nearest millimeter, in particular noting the beam position as it is reflected from the mirrors in question. Allowances should then be made for the different optical path lengths in the various materials (glass,  $\text{LiNbO}_3$ ,  $\text{CaCO}_3$ ) due to different indices of refraction. For example, the double passing of a 5 cm  $\text{LiNbO}_3$  crystal, with an index of refraction of approximately 2.1, adds 11 cm to the optical path length of the oscillator arm when compared to the propagation through air. The amplifier delay line has two mirrors

positioned on a translation stage to help make this adjustment.

With the overlap adjustment complete, the IR seed and pump beams can be passed through the amplifier crystal. There is a sapphire mirror at the crystal output which reflects most of the 1.064 $\mu\text{m}$ . The signal level in the IR should be monitored with an energy meter, since optimally the IR output will be near 1mJ. The energy meter should be placed at least 40 cm away from the amplifier crystal to assure that the IR measured is coming from amplification of the seeded pulse produced in the "oscillator " half of the OPA rather than being an amplified noise signal produced solely in the second crystal.

The phase-matching angle of the second crystal should be adjusted slowly until the IR output is maximized. The horizontal tilt can also be adjusted to maximize the output, but will have a much smaller effect. If the IR signal output (working at  $\omega_i = 3300\text{cm}^{-1}$ , for example) does not approach 1mJ levels, it is possible that the overlap is slightly off. Small adjustments of the 45 $^\circ$  mirror before the amplifier crystal can be made, but it should be kept in mind that mirror angle adjustments will change the propagation direction in the crystal and that the phase matching angle will have to be readjusted with each movement of the 45 $^\circ$  mirror.

Careful optimization should lead to the proper level of IR generation. A definitive check for proper operation should be to block the oscillator arm. This should completely eliminate the output, assuring that the signal is being seeded by the oscillator half rather than being produced solely in the amplifier crystal.

#### 4. Performance of the System

When correctly aligned, the system will produce 1mJ in the IR, that being the combined energy of the signal and idler. Since one photon at the pump converts to one photon at the signal and one at the idler, the ratio of signal energy to idler energy will be proportional to the ratio of the signal and idler frequencies. (Note the  $\omega_i/\omega_s$  factor in equation (19b) for the idler intensity.)

The tuning curve is given in figure 7. The curve was derived using equation (25) with the Sellmeier equations (24a) and (24b). The output continuously covers the IR spectrum from 1.4 to 4  $\mu\text{m}$  except at the water absorption line ( $3435\text{cm}^{-1}$  -  $3550\text{cm}^{-1}$ ) in the  $\text{LiNbO}_3$ . (The low transmission of the  $\text{LiNbO}_3$  in this frequency regime will prevent operation of the OPA in the  $3470\text{cm}^{-1}$  -  $3500\text{cm}^{-1}$  range and reduce it in the  $3435\text{cm}^{-1}$  -  $3470\text{cm}^{-1}$  and  $3500\text{cm}^{-1}$  -  $3550\text{cm}^{-1}$  ranges.) Notice that due to the 53 cm length of the arm that controls the crystal angle, the stepping motor must be moved approximately 13 cm to cover the entire tuning range of the device. (Figure 7 shows that the tuning range of the OPA is covered by a  $7^\circ$  change of angle between the optic axis and the pump propagation direction. The  $7^\circ$  change of angle between the optic axis and the pump propagation direction inside the crystal corresponds to a  $14^\circ$  twist of the crystal due to the large index of refraction ( $n=2.1$ ) of  $\text{LiNbO}_3$ .) The tuning of the device results in a  $16\text{cm}^{-1}$  change for a 1 millimeter motion of the stepping motor. The limit of the device occurs when the idler frequency becomes strongly attenuated by absorption in the  $\text{LiNbO}_3$ . Pulse to pulse fluctuations are in the range of 20% to 30%, due primarily to the beam wander in the crystals. (The beam wander can be seen most vividly by setting an iris in front of the  $\text{LiNbO}_3$  amplifier crystal. Under normal operating conditions, the burn spot on the iris will move on the order of 1 millimeter from shot to shot. The beam wander is caused primarily by index of refraction fluctuations, caused by thermal fluctuations near the hot ends of the oscillator and amplifier Nd:YAG rods. This can be seen most readily by removing the tubes which surround the ends of either of these rods. If one does this, the beam wander becomes considerably worse. It will be on the order of 5 - 10 millimeters shot-to-shot on an iris placed in front of the amplifier crystal. Replacing the tubes greatly diminishes, but does not completely eliminate the wander.)

## F. Second Harmonic Generation

### 1. Principles of Operation

The second harmonic generator is perhaps the easiest subsystem to understand, since it is simply a high-conversion efficiency nonlinear optical device. The expression for high conversion efficiency phase-matched second harmonic generation is<sup>21</sup>

$$P_{2\omega}(z) = P_{\omega}(0) \tanh^2[\mathbb{C} (P_{\omega}(0)/A)^{1/2} z], \quad (26)$$

where  $\mathbb{C} = \mathbf{K} (2\omega/n)(2\pi c/n)^{1/2}$  and  $\mathbf{K} = (2\pi/c^2) \mathbf{e}_{2\omega} \cdot \chi^{(2)}(2\omega = \omega + \omega) : \mathbf{e}_{\omega} \mathbf{e}_{\omega}$ .

For the crystal in question, type-II phase matching is used. In this case, some of the fundamental travels as an o-ray and some travels as an e-ray with the second harmonic traveling as an e-ray also. The phase matching condition then leads to

$$n_e(2\omega) = (1/2) [n_o(\omega) + n_e(\omega)], \quad (27)$$

from which it can be found that the phase-matching angle occurs at  $\theta = 53.5^\circ$ . The KDP crystal geometry puts it in the 4 2-m point group. The nonvanishing elements are<sup>21</sup>

$$\chi^{(2)}_{XYZ} = \chi^{(2)}_{YXZ} = \chi^{(2)}_{XZY} = \chi^{(2)}_{YZX} \quad (28a)$$

and

$$\chi^{(2)}_{ZXY} = \chi^{(2)}_{ZYX}. \quad (28b)$$

The effective nonlinear susceptibility for type-II phase-matching is

$$\begin{aligned} \chi^{(2)}_{\text{eff}} &= \mathbf{e}_3 \cdot \chi^{(2)} : \mathbf{e}_1 \mathbf{e}_2 = \\ &+ \chi^{(2)}_{ZXY} \sin(2\theta) \cos(2\phi), \end{aligned} \quad (29)$$

where  $\theta$  and  $\phi$  are the angles which define the propagation direction of the pump beam

through the crystal, relative to the crystal coordinate system. Here  $\theta$  is the angle between the propagation direction and the z-axis and  $\phi$  is the angle between the projection of the propagation direction in the x - y plane and the x-axis. (In a uniaxial birefringent crystal, the optic-axis is taken to be the z-axis.)  $e_3$ ,  $e_1$ , and  $e_2$  are the polarization unit vectors for the second harmonic ( $e_3$ ) and fundamental beams ( $e_1$  and  $e_2$ ) respectively. (Recall that in type-II phase matching  $e_3$  is an e-ray,  $e_1$  is an o-ray, and  $e_2$  is an e-ray.) Note that using type-II phase matching leads to a slightly enhanced  $\chi^{(2)}_{\text{eff}}$  as compared to the type-I case. Specifically,

$$\begin{aligned} \chi^{(2)}_{\text{eff type-II}} / \chi^{(2)}_{\text{eff type-I}} &= \quad (30) \\ &= \sin(2\theta_{\text{II}} = 2 \times 53.5^\circ) \cos(2\phi) / \sin(\theta_{\text{I}} = 40.5^\circ) \sin(2\phi) = 1.47, \end{aligned}$$

if it assumed that  $\phi = 45^\circ$  in both cases.

Equation (26) can be used to predict the power conversion efficiency. For this case,  $2\omega = 18797\text{cm}^{-1}$ ,  $n = 1.5$ ,  $\chi^{(2)}_{\text{eff}} = 2.7 \times 10^{-9}$ ,  $z = 1.5\text{centimeter}$ ,  $P_\omega(0) = 1.3 \times 10^{15}\text{esu}$ , and  $A = .06\text{cm}^2$  (spot diameter = 3millimeter). Substitution into equation (26) gives  $P_{2\omega}(z = 1.5\text{cm}) = (.25)P_\omega(0)$ .

## 2. Elements Composing the System

The second harmonic generator is composed of a 1.3cm x1.3cm x1.5cm KD\*P crystal angle cut for phase-matched 1.064  $\mu\text{m}$  to .532  $\mu\text{m}$  generation. It is mounted in a teflon cylinder with Brewster angle input and output windows. The device is o-ring sealed to prevent exposure to moisture (KD\*P is a hydroscopic crystal). The teflon is machined to fit into a Lansing rotational mount, whose precision is need to properly align the crystal tilt.

## 3. Technical Operation



The second harmonic generator is assembled in a dry-nitrogen glove box. It is desirable to refill the container with nitrogen once a year.

The basic alignment should be done with low input power powers ( $<1\text{mJ}$ ) (see figure 8). A high power pulse which grazes a corner of the face or hits an inside crystal surface can cause damage. It is also easier to tell when the crystal is phase-matched at lower powers since one's eyes have a more linear response at lower power.

The  $1.064\ \mu\text{m}$  input propagation should be near normal to the input face. The crystal should be oriented so that the optic axis is at  $45^\circ$  with respect to the  $1.064\ \mu\text{m}$  polarization. (The polarization should coincide with an input face diagonal.)

There are two tilts to be adjusted. One axis is parallel to the  $1.064\ \mu\text{m}$  polarization, the other is perpendicular to it. The tilt about the axis perpendicular to the  $1.064\ \mu\text{m}$  polarization is more sensitive. The phase-matching angle is fairly sharply peaked, so that near the optimum, the adjustment should be done very carefully.

The full power alignment can now be done by turning up the amplifier flashlamp pumping power to increase the  $1.064\ \mu\text{m}$  input laser power. This adjustment should be done with an energy meter, with some filter to cut off the fundamental. The tilt of both axes should produce clear maxima. As predicted, an input of  $8\text{mJ}$  at the fundamental will produce an output of  $2\text{mJ}$  in the second harmonic.

#### 4. System Performance

The SHG has a short warm-up time, but this equilibrium will be reached within one minute. (There is a temperature effect on the indices of refraction.) The second harmonic generator should function for long periods of time without any degradation in performance.

If the second harmonic generator is used in conjunction with the IR (e.g. for SFG experiments), then the relative delay for the SHG line must be matched to that of the IR line. To do this, the two optical path lengths should be measured and physically matched with appropriate allowances made for the indices of refraction of the various optical elements in

the laser path. The final temporal overlap is checked by optical cross-correlation, specifically a sum-frequency generation measurement from either the bulk or surface of an appropriate non-linear crystal. (In the surface sum-frequency generation experiments described in the subsequent chapters of this thesis, it was found that a cross-correlation from a crystalline quartz surface was very convenient for checking the temporal overlap of IR and visible pulses.)

### G. Integrated System

The integrated system is shown in figure 9. The entire system, when aligned properly, simultaneously provides pulses of 2mJ, 15ps at .532  $\mu\text{m}$  and 200 $\mu\text{J}$ , 15ps, tunable in the IR from 1.4  $\mu\text{m}$  to 4  $\mu\text{m}$ . The modes are near  $\text{TEM}_{00}$  mode, the IR being slightly degraded by imperfections in the  $\text{LiNbO}_3$  crystals. The system operates at 10Hz.

To compensate for day to day drifts in the alignment, there are several irises which should be installed once the system is aligned. These are the most important irises (shown in figure 8): 1) before the single pulse selector, 2) before the second harmonic generator, 3) before the 70-30 beamsplitter, 4) before the copper mirror, and 5) before the  $\text{LiNbO}_3$  amplifier crystal.

The oscillator, once optimized should be aligned on iris#1 first via the beam steerer at its output. The mirror (#1) after the beam steerer should align the 1.064  $\mu\text{m}$  to iris #1. Before turning on the single pulse selector power supply, mirror#2 should be adjusted until there is at least a small amount of green light leaking through (the leak through the single pulse selector after amplification will still be strong enough to produce a small amount of green.) This should simultaneously align the system to iris#2 and iris#5. The 60-40 beamsplitter should align the 1.064  $\mu\text{m}$  to iris #3. The 45 $^\circ$  mirror#2 should align the 1.064  $\mu\text{m}$  to iris #4.

The laser system seems to work better the more it is used. This is probably because it receives daily alignment. Normally, start-up adjustments should not exceed 15 minutes.

One final note on the system. It is difficult to deal with a homemade laser of this size. Each subsystem has its own quirks and secrets for quick alignment. (This author has listed all that he is aware of in the previous sections.) Each operator must develop a certain amount of familiarity with the laser before its operating behavior becomes completely transparent. In other words, if at first you don't succeed, keep adjusting the mirrors.

## References

1. H.P. Korts, IEEE J. Quant. Electr. QE-19, 578, (1983).
2. W. Koechner, Solid State Laser Engineering (Springer-Verlag, New York, 1976).
3. D.A. Pinnow, IEEE J. Quant. Electr. QE-6, 223 (1970).
4. D.J. Kuizenga and A.E. Siegmann, IEEE J. Quant. Electr. QE-6, 694 (1970).
5. V.S. Letokov, SOC. Phys. JETP 28, 562 (1969).
6. W.H. Glenn, IEEE J. Quant. Electr. QE-8, 766, (1972).
7. W. Zinth, A. Laubereau, and W. Kaiser, Optics Comm. 22, 161 (1971).
8. G.H.C. New, IEEE J. Quant. Electr. QE-14, 642 (1978).
9. G.H.C. New, T. B. O'Hare, Phys. Lett. 68A, 27 (1978).
10. G.H.C. New, Proc. IEEE 67, 380 (1979).
11. C. Kolmeder and W. Zinth, Appl. Phys. 24, 341 (1981).
12. A. Leitner, M.E. Lippitsch, E. Roschger, and F.R. Aussenegg, IEEE J. Quant. Electr. QE-19, 562 (1983).
13. R. Wilbrandt and H. Weber, IEEE J. Quant. Electr. QE-11, 186 (1975).
14. This is in agreement with the work of other investigators. see, for example, J.P. Heritage, Ph.D. thesis, University of California, Berkeley, 1975 (unpublished).
15. D.C. Brown, The Physics of High Peak Power Nd:Glass Laser Systems, (Springer-Verlag, New York, 1980).
16. R.C. Hyer, H.D. Surphin, and K.R. Winn, Rev. Sci. Instr. 46, 1333 (1975).
17. R. O'B, Carpenter, J. Opt. Soc. Am. 40, 225 (1950).
18. see, for example, M. Born and E. Wolf, Principles of Optics, (Macmillan Co., New York, 1964).
19. J. Wilkinson, J. IEE, 93, 1098 (1946).
20. J.A. Oicles, Lawrence Livermore National Laboratory, Livermore, CA, private communication.
21. Y.R. Shen, The Principles of Non-linear Optics, (John Wiley, New York, 1984).

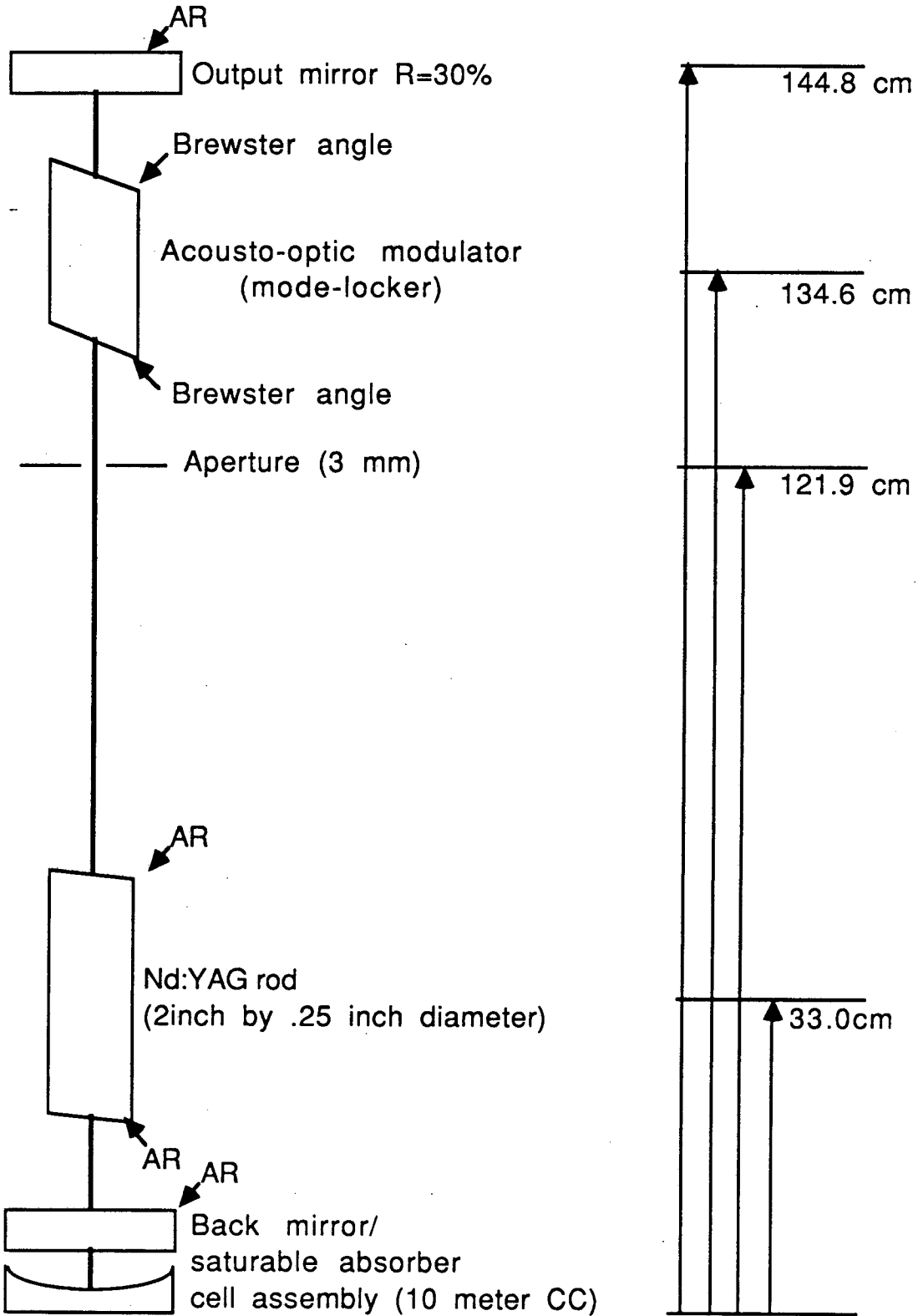
22. A. Laubereau, L. Greiter, and W. Kaiser, Appl. Phys. Lett. 25, 87 (1974).
23. R.A. Baumgartner and R.L. Byer, IEEE J. Quant. Electr. QE-15, 432 (1979).
24. A. Seilmeier and W. Kaiser Appl. Phys. 23, 113 (1980).
25. W. Kranitzky, K. Ding, A. Seilmeier, and W. Kaiser, Opt. Comm. 34, 483 (1980).
26. M.W. Hobden and J. Warner, Phys. Lett. 22, 243 (1966).
27. Hass, J. Opt. Soc. Am. 45, 945 (1955).
28. see, for example, Lasers and Applications 1987 Designer's Handbook, (High Tech Publications Inc., Torrance, CA 1986).

## Figure captions

- Fig. 1 Oscillator schematic: The distances on the right are the distances between the back mirror reflective surface and the center of the optical element in question.
- Fig. 2 Basic transmission line schematic for high voltage, short temporal pulse formation in Lasermetrics power supply. (Top of Figure.) Figures (a) through (e) show the voltage on the cable as a function of position in the cable, at various times in the formation of the output pulse: (a)  $t = 0$ , immediately before the Krytron electrically connects the two cables, (b)  $t = (1/2) t_p$ , where  $t_p$  is the round trip time of the voltage wave in the charged cable, (c)  $t = (1/2) t_p$ , (d)  $t = (3/4) t_p$ , (e)  $t = t_p$ .
- Fig. 3 Single Pulse Selector: The diagram shows the optical elements and the electrical connections between the Pockel's cell and the Lasermetrics power supply. Note that there are three cables: the charged cable which determines the high voltage pulse duration, the power supply output cable which delivers this pulse to the Pockel's cell and the exit cable. The exit cable is long enough to prevent any reflections from its 50 ohm termination from reaching the Pockel's cell until after the train has completely passed the single pulse selector. The position of the photodiode which triggers the Lasermetrics power supply is also shown.
- Fig. 4 Double Pass Amplifier: The old method on the left spatially separates the second pass. The new method on the right uses polarization rotation to separate the amplified pulse.
- Fig. 5 Comparison of on-axis and off-axis k-matching: These figures show the possible phase-matching geometries that lead to large bandwidths on a single pass of the crystal.
- Fig. 6 Optical Parametric Amplifier: This is the basic positioning of the optics.
- Fig. 7 OPA output curve: Shows the signal and idler output frequencies as a function of pump propagation angle with respect to the  $\text{LiNbO}_3$  optic-axis.
- Fig. 8 Second Harmonic Generation:  $\text{KD}^*\text{P}$  crystal and relative input and output

polarization orientations.

Fig. 9 Integrated System: Shows the basic optics positions needed for using the system as a whole.



AR indicates anti-reflection coating

Oscillator Schematic  
Figure 1

XBL-881-128



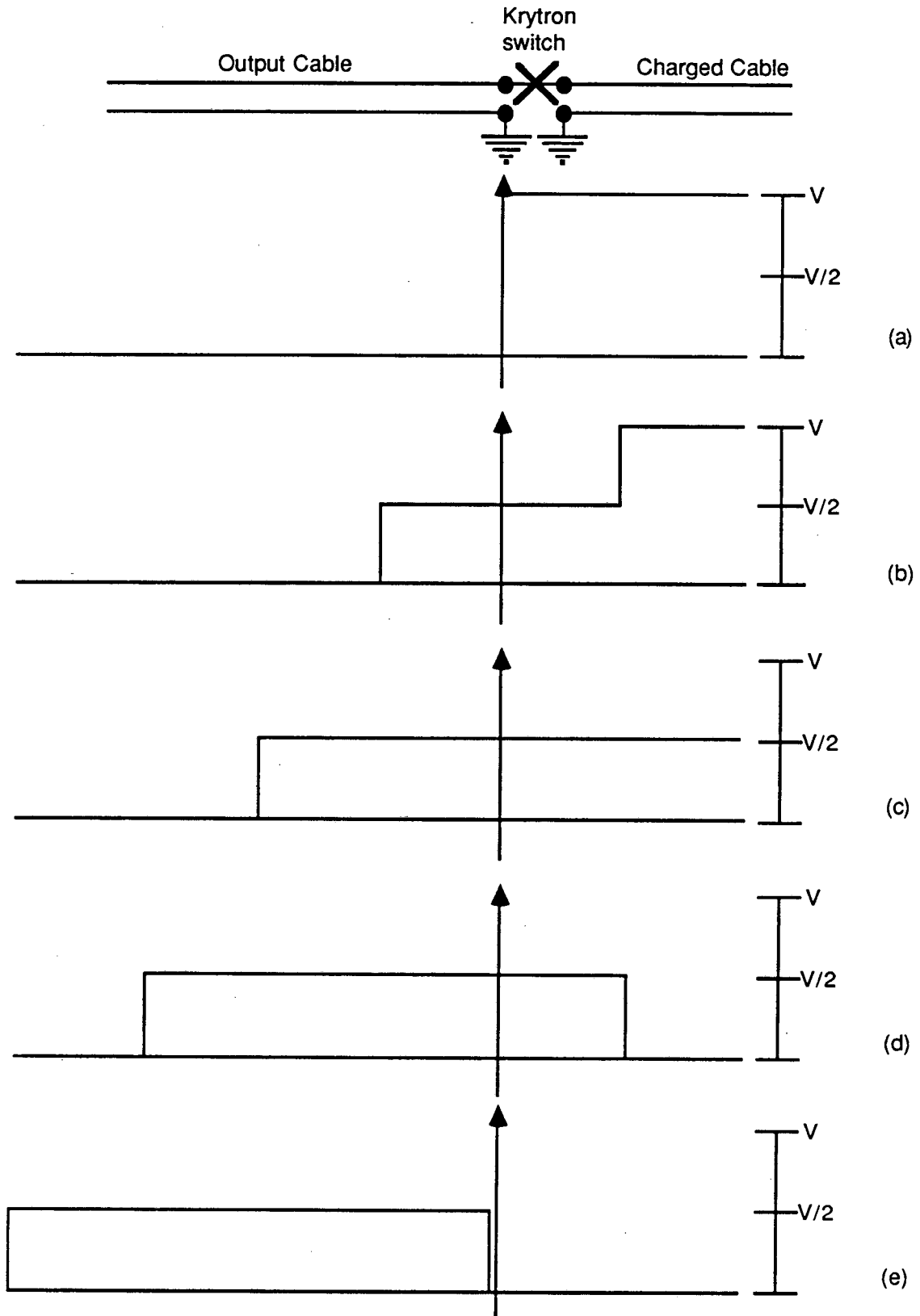
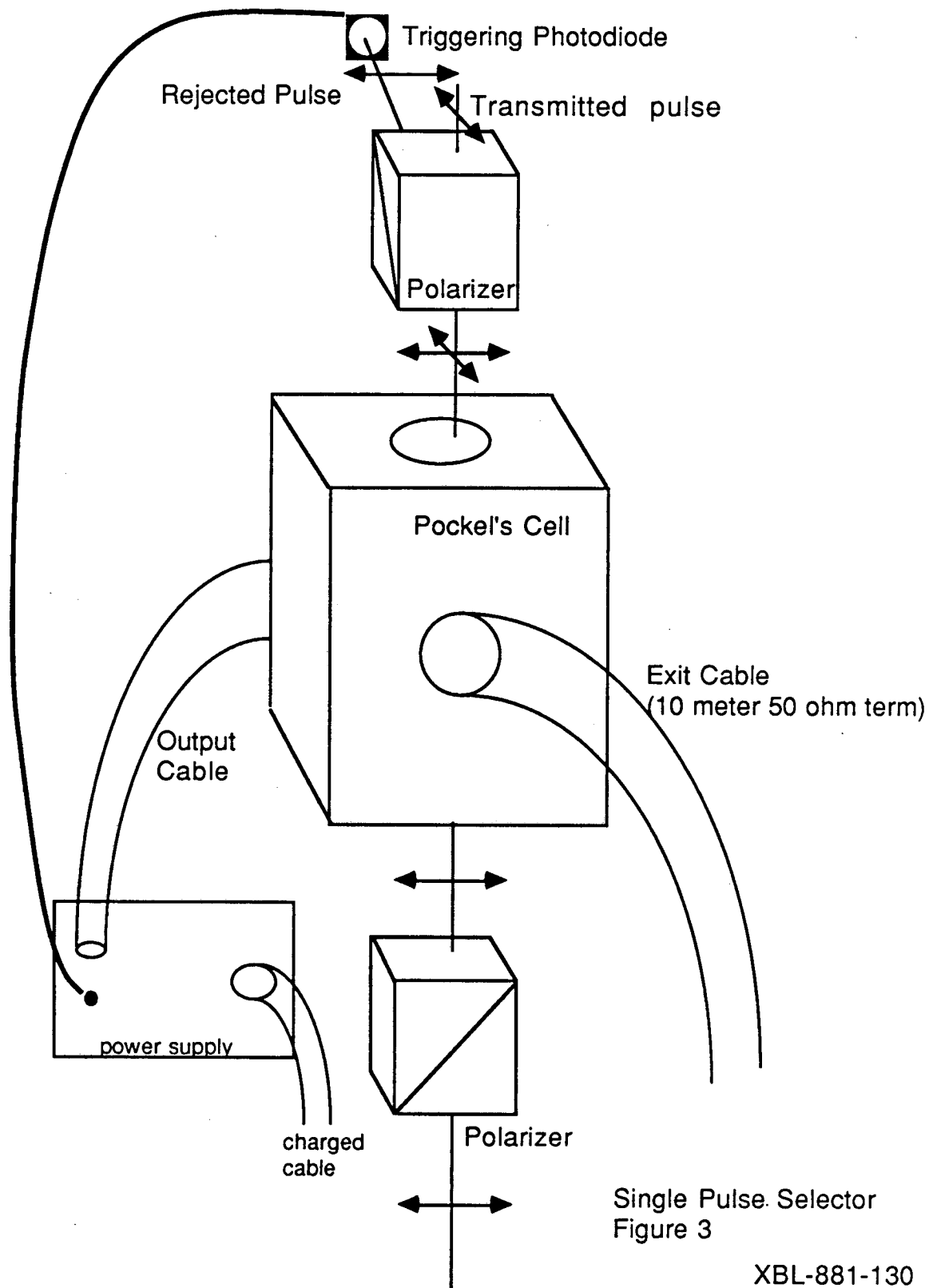
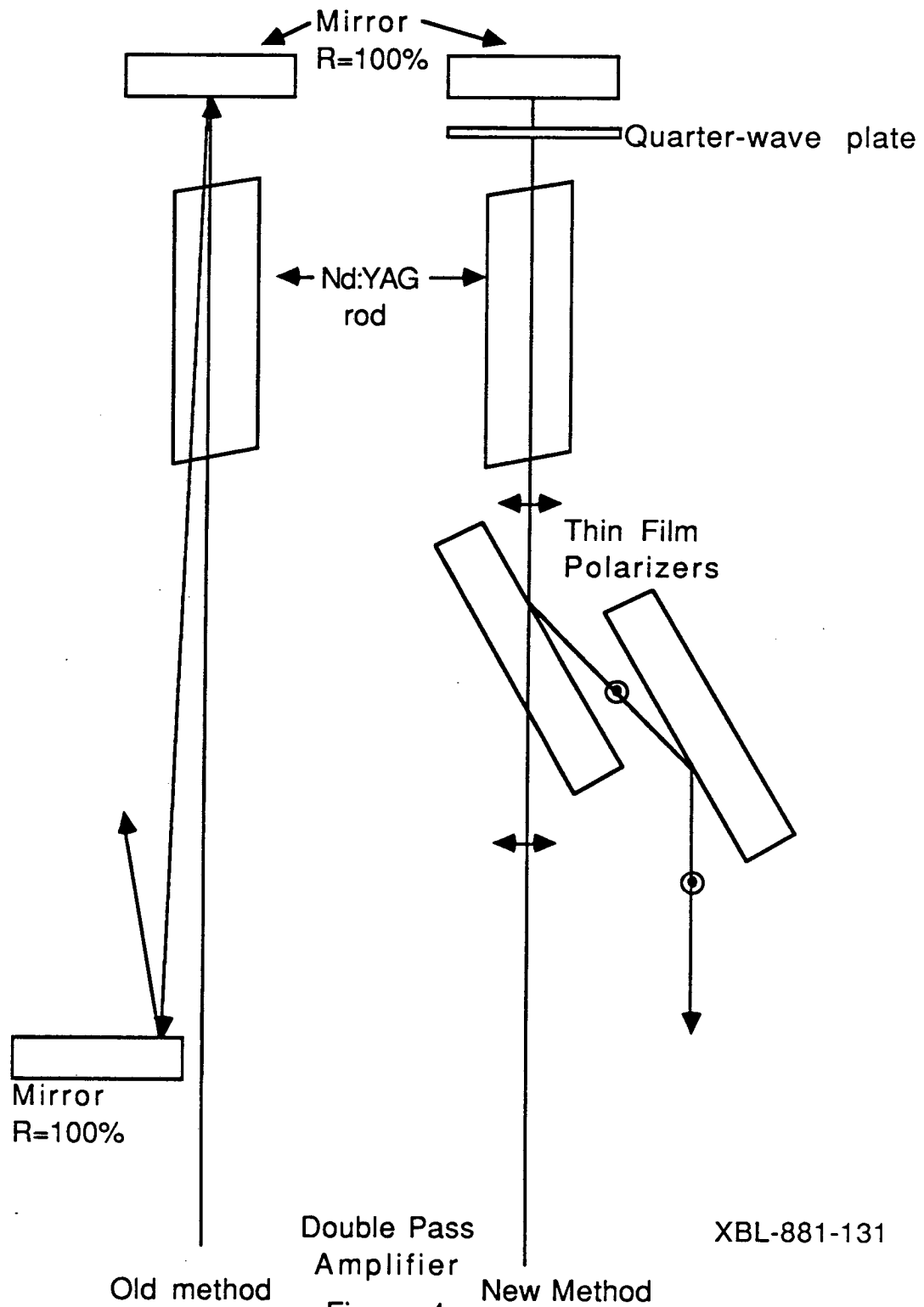


Figure 2

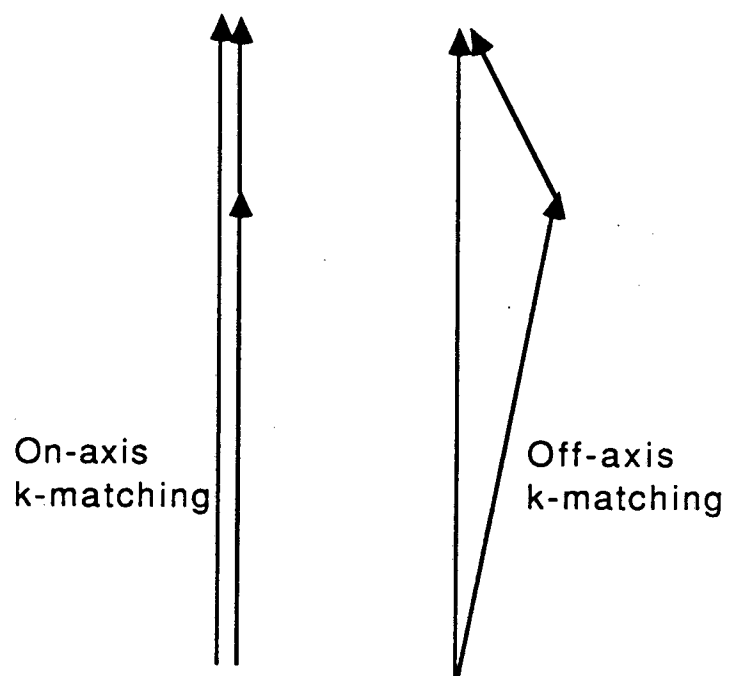
Discharge Cable Schematic  
with Voltage as function of Time

XBL- 881- 129





XBL-881-131



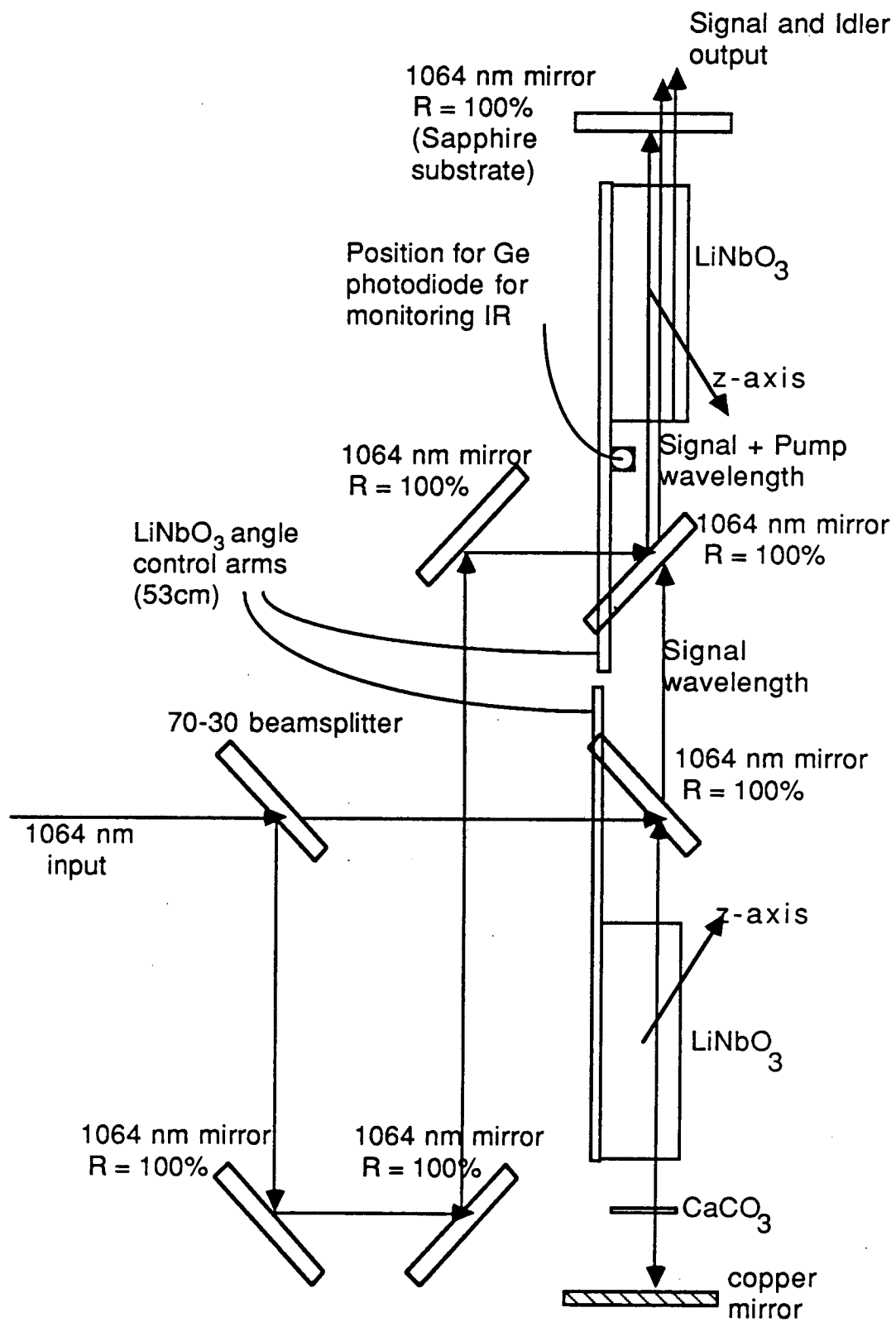
On-axis  
k-matching

Off-axis  
k-matching

Comparison of On-axis  
and Off-axis k-matching

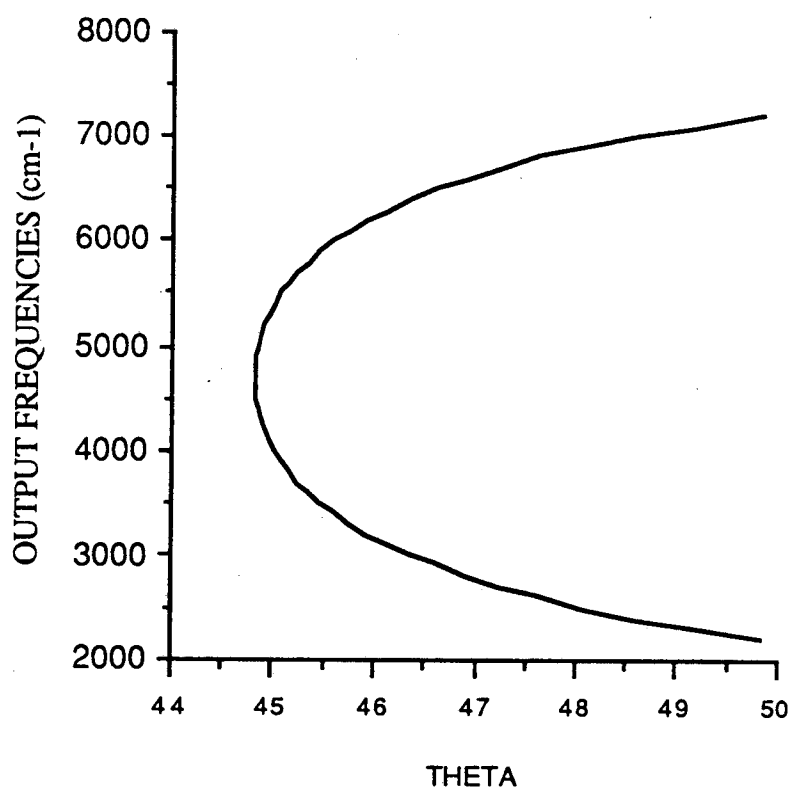
Figure 5

XBL-881-132



Optical parametric Amplifier  
Figure 6

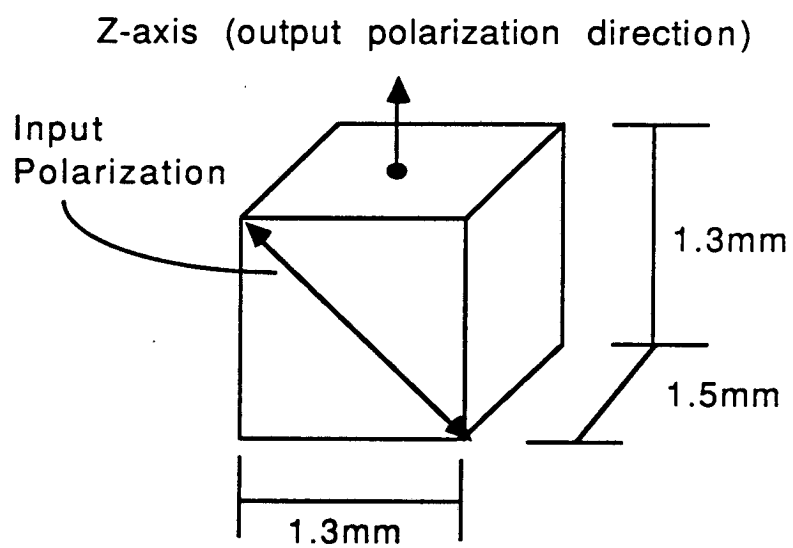
XBL-881-133



LiNbO3 OPA phase-matching curve

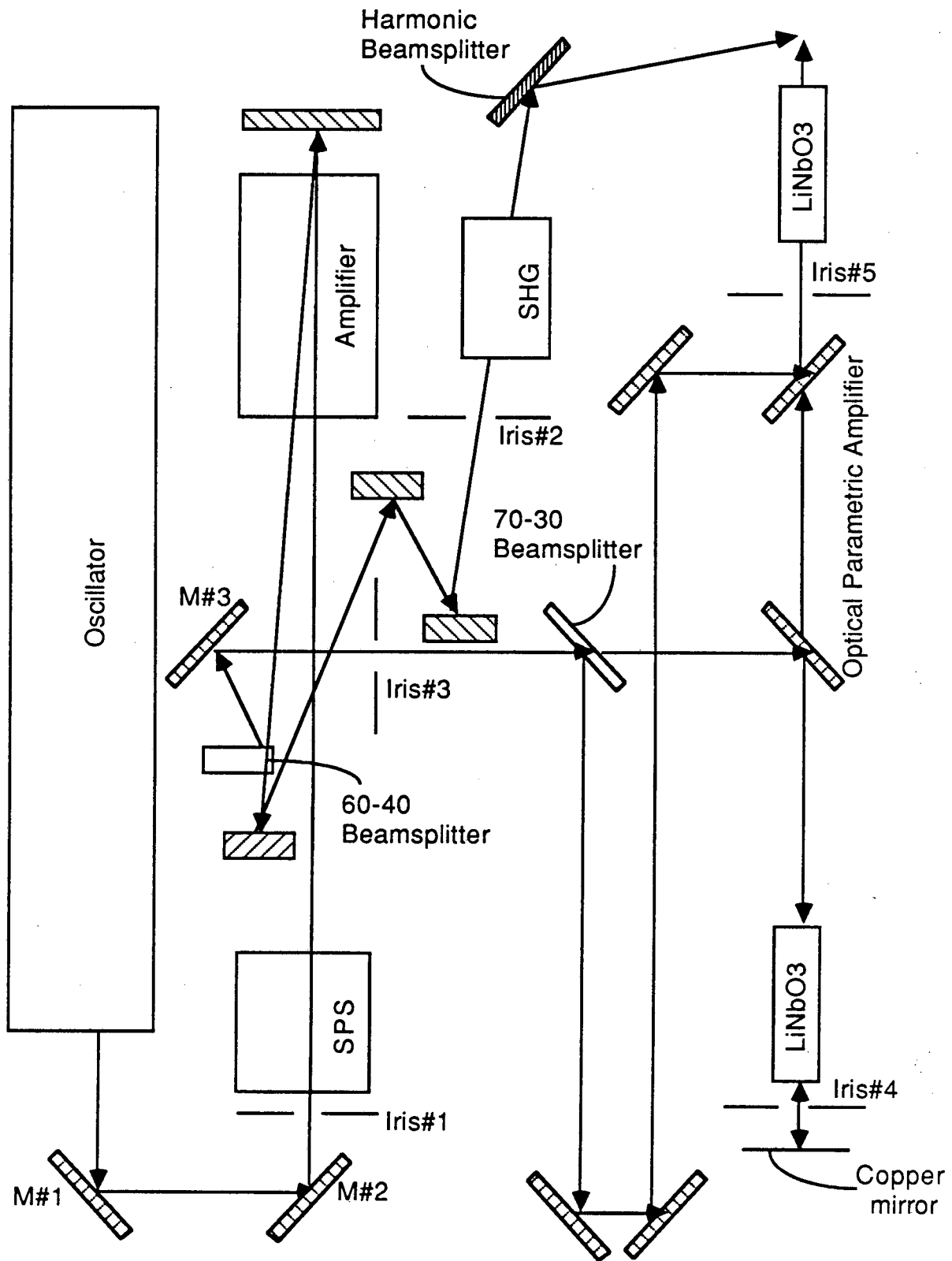
Figure 7



XBL-881-134



Second Harmonic Generator  
KD\*P crystal  
Figure 8

XBL-881-135



Integrated System  
 Figure 9  = 1064nm mirror  
 = Iris

XBL-881-136



### III. Introduction to Sum Frequency Generation: Spectroscopy of Alcohols at Air-Solid Interfaces

The use of second harmonic generation (SHG) to study the interface between two centrosymmetric media has been well established at this point.<sup>1</sup> One serious drawback of the technique is the lack of species specificity. This lack is due to the fact that the low signal levels produced by surface SHG require photomultiplier sensitivities for detection. Photomultiplier sensitivities are large only in the visible regime and very-near infra-red ( $\lambda=1\mu\text{m}$ ). In this frequency regime, only electronic excitations can be made in molecules. These excitations usually have broad features which are not highly useful for identification or study of the particular molecule in question.

For species specific molecular spectroscopy, especially at interfaces, vibrational spectroscopy is much more useful.<sup>2</sup> The plethora of vibrational spectroscopic techniques is testimony to this. However, each has its limitations. Electron energy loss<sup>3</sup> and surface photoacoustic spectroscopy<sup>4</sup> require a UHV environment. Electron tunneling spectroscopy<sup>2</sup> requires the molecules to be sandwiched into a semiconductor barrier. Surface infrared-spectroscopy<sup>2</sup> requires long integration times during data taking because of the poor signal-to-background ratios. All of these techniques have severe restrictions on the interfaces that they can examine because they can only be used in certain environments. One would like a technique with the versatility of SHG, but able to probe vibrational spectra in the infra-red (IR).

IR-visible sum-frequency generation (SFG) has all the advantages of SHG but can obtain vibrational spectra as well.<sup>5</sup> The first measurements made with this technique were done by Tom and Page<sup>6</sup>, but their inability to clean their sample substrate left them unable to clearly identify the species on their substrate. Zhu et.al. clearly identified Coumarin 504 on a fused silica substrate by mixing a  $.532\mu\text{m}$  input with the  $10\mu\text{m}$  input from a  $\text{CO}_2$  laser.<sup>7</sup>

Unfortunately, the limited tuning range and slow repetition rate of the CO<sub>2</sub> laser made the experiment very tedious.

The SFG experiments discussed in this thesis were the first ones done with this technique using an IR source of sufficiently high repetition rate (10Hz) and range of tunability (1.4μm to 4μm) that the technique could be used to quickly ascertain the vibrational spectrum in question. This chapter begins with a general theoretical discussion of the technique in section A. Section B outlines the basic experimental set-up. The first data taken with this set-up is shown in section C and results are discussed in section D.

#### A. General Considerations

The fundamental principle which makes SFG a useful surface and interface technique is the fact that even-ordered nonlinear processes identically vanish in centrosymmetric media. Consider the relation that governs the general three-wave sum-frequency process

$$\mathbf{P}^{(2)}(\omega_3=\omega_1+\omega_2) = \chi^{(2)}(\omega_3=\omega_1+\omega_2):\mathbf{E}(\omega_1)\mathbf{E}(\omega_2) \quad (1)$$

In the electric dipole approximation the existence of a center of inversion in a material means that

$$\chi^{(2)}(\mathbf{r}) = \chi^{(2)}(-\mathbf{r}) \quad (2)$$

Consequently, in the above relation( or in any relation having an even number of E terms), the reversing of the directions of the displacement vectors ( $\mathbf{r}$ ) leads to

$$\chi^{(2)}=0. \quad (3)$$

Suppose one examines the situation at an interface between two centrosymmetric media. The only place that the centrosymmetry is broken is at the interface. Consequently, any SFG signal will have to be generated at that interface, so that the process is highly surface-specific.

Consider the frequency response of the nonlinear polarizability  $\alpha^{(2)}(\omega_3=\omega_1+\omega_2)$  in the case where  $\omega_1$  is near some resonance in the medium.  $\alpha^{(2)}$  can be separated into two components,  $\alpha^{(2)} = \alpha^{(2)}_R + \alpha^{(2)}_{NR}$ , where  $\alpha^{(2)}_R$  is the frequency dependent part of the nonlinear susceptibility and  $\alpha^{(2)}_{NR}$  is the frequency independent part of the nonlinear susceptibility. It can be shown from the microscopic expressions

$$[\alpha^{(2)}_R(\omega_3)]^2_{ijk} = [\alpha^{(1)}_R(\omega_1)]_{kk} [\alpha^{(3)}_R(\omega_3=\omega_2+\omega_3-\omega_2)]_{ijij} \quad (4)$$

where  $\alpha^{(1)}_R$  and  $\alpha^{(3)}_R$  are the resonant IR and Raman polarizabilities, respectively. Specializing now to the surface case, the microscopic polarizability is related to the macroscopic susceptibility as<sup>8</sup>

$$s\chi^{(2)} = N_s \langle \alpha^{(2)} \rangle \quad (5)$$

assuming the local-field correction is negligible. Here,  $\chi^{(2)} = \chi^{(2)}_R + \chi^{(2)}_{NR}$ , where  $\chi^{(2)}_R$  is the frequency dependent part of the nonlinear susceptibility and  $\chi^{(2)}_{NR}$  is the frequency independent part of the nonlinear susceptibility. Here  $N_s$  is the density of surface adsorbates, the  $s$  superscript denotes surface, and the  $\langle \rangle$  denotes an average over the molecular orientational distribution.

There are two important points to be gleaned from this expression. First, if  $\omega_1$  coincides with a resonance of the material, there will be an enhancement in  $\alpha^{(2)}$  and

consequently in  $S\chi^{(2)}$  leading to a larger SFG signal. Specifically, for a surface layer of molecules,<sup>9</sup>

$$({}^S\alpha^{(2)})_{lmn} = (A_n M_{lm} \Delta\rho) / [(h/2\pi)(\omega_{IR} - \omega_v + i\Gamma_v)], \quad (6)$$

where

$$A_n = \langle g | e r_n | v \rangle,$$

$$M_{lm} = \sum_s \{ [\langle v | e r_n | s \rangle \langle s | e r_l | g \rangle / (h/2\pi)(\omega_{SF} - \omega_{SG})] \\ - [\langle v | e r_l | s \rangle \langle s | e r_m | g \rangle / (h/2\pi)(\omega + \omega_{SG})] \},$$

v, s, and g refer to the vibrational excited state, the intermediate state, and the ground state, respectively,  $\Delta\rho$  is the population difference between  $\langle g |$  and  $\langle v |$ , and  $\omega_v$  and  $\Gamma_v$  are the vibrational resonance frequency and the associated damping constant, respectively. Second, in order for  $\alpha^{(2)}$  to exhibit this resonant enhancement, the transition in question must be both IR (one-photon) and Raman (two-photon) active.<sup>5,7</sup>

Although there are many cases where this does occur, it is not generally true. In an unsymmetrical molecule,<sup>10</sup> every normal vibration is infra-red active and every normal vibration is Raman active. In a symmetrical molecule, that is, one with a center of inversion, transitions which are allowed in the IR are forbidden in the Raman spectrum and those which are allowed in the Raman are forbidden in the IR. The condition which leads to the existence of a non-zero  $\alpha^{(2)}$ , namely, the lack of a center of inversion in the molecular vibration, is also necessary for the vibration to be both IR and Raman active.

If the molecule in question is adsorbed to a surface, the symmetry of the molecular vibration may change, depending on the particular mechanism of adsorption. This could cause a symmetrical molecule to lose its center of symmetry. In this case, it could become both IR and Raman active when adsorbed to a surface, even though it is not both IR and

Raman active in bulk. The presence of the surface may modify the symmetry of the molecule, but once this new symmetry is obtained, the basic rule for IR and Raman activity or inactivity is the same as in the bulk case.

Sum-Frequency Generation from the surface is a coherent process and as such is subject to a surface phase-matching condition,

$$s_{k_{sf}} = s_{k_{vis}} + s_{k_{ir}} \quad (7)$$

where the  $s$  superscript indicates the projection of the input and output  $k$ -vectors onto the surface. From this, it can be determined that

$$n_{sf}\omega_{sf}\sin(\theta_{sf}) = n_{vis}\omega_{vis}\sin(\theta_{vis}) + n_{ir}\omega_{ir}\sin(\theta_{ir}) \quad (8)$$

where  $n_{sf}$ ,  $n_{vis}$ , and  $n_{ir}$  are the indices of refraction for the SFG beam and two inputs respectively in the bulk media in which they are propagating and where  $\theta_{vis}$  and  $\theta_{ir}$  are the incident angles of the visible and IR beams respectively and  $\theta_{sf}$  is the output angle of the SFG beam.

A straightforward analysis analogous to SFG in bulk shows that the SFG surface signal is given by<sup>1</sup>

$$S = 256\pi^4 (\omega_{sf}/hc^3) |L_{SF}^m L_V^n L_{IR}|^2 |\chi_{lmn}^{(2)}|^2 (U U_{IR}/AT) \quad (9)$$

Here, the  $L$  are geometric Fresnel factors relating the surface fields to the radiating fields in air,  $U$  and  $U_{IR}$  are the visible and IR pulse energies,  $A$  is the pulse overlapping cross-sectional area,  $T$  is the pulse duration, and  $S$  is in photons per pulse. The geometric Fresnel factors for the input fields are given by

$$L_x = [-2 n_1 \sin\theta_2 \cos\theta_1] / [n_2 \cos\theta_1 + n_1 \cos\theta_2]$$

$$L_y = [2 n_1 (n_2)^2 \cos\theta_2 \cos\theta_1] / [n_2 \cos\theta_1 + n_1 \cos\theta_2]$$

$$L_z = [2 n_1 \cos\theta_1] / [n_1 \cos\theta_1 + n_2 \cos\theta_2]$$

and the geometric Fresnel factors for the output field are given by

$${}^{SF}L_x = (\cos\theta_2) / [n_2 \cos\theta_1 + n_1 \cos\theta_2]$$

$${}^{SF}L_y = [1 / (n_1 \cos\theta_1 + n_2 \cos\theta_2)]$$

$${}^{SF}L_z = (n_2 / n_1) [\sin\theta_1 / (n_2 \cos\theta_1 + n_1 \cos\theta_2)],$$

where  $z$  is the surface normal, the  $x$ - $z$  plane is the plane of incidence,  $n_1$  and  $n_2$  refer to the bulk indices of refraction for the two centrosymmetric media,  $\theta_1$  is the angle of incidence for the input fields and is the output angle for the sum-frequency fields, and  $\theta_2$  is defined by  $n_1 \sin\theta_1 = n_2 \sin\theta_2$ . One uses these factors in the following way. The input fields can be expressed as  $s$ - and  $p$ -polarized components  $E_s$  and  $E_p$ . Then the surface fields can be expressed by

$${}^sE_x = L_x E_p$$

$${}^sE_y = L_y E_p$$

$${}^sE_z = L_z E_s.$$

The surface nonlinear polarizations  ${}^sP_x$ ,  ${}^sP_y$ , and  ${}^sP_z$  are found through the surface nonlinear susceptibility tensor. Finally, the output fields are expressed by

$${}^sE_p = {}^{SF}L_x {}^sP_x + {}^{SF}L_z {}^sP_z$$

$${}^sE_s = {}^{SF}L_y {}^sP_y$$

Because of the nature of the optical source, the experiment will usually be run in the limit where

$$U_{IR} \ll U \quad (10)$$

In this case, the SFG signal strength (equation (9)) can be re-expressed as an efficiency of conversion of IR to SFG photons

$$N_{SF} = \eta N_{IR} \quad (11)$$

where

$$\eta = 128\pi^3 (\omega_{sf} \omega_{IR}/c^3) |L_{SF}^m L_V^n L_{IR}^l|^2 |\chi_{lmn}^{(2)}|^2 I_{VIS}$$

and  $I_{VIS}$  is the intensity of the visible beam.

$I_{VIS}$  is usually limited by the damage threshold of the substrate. Damage may come in the form of bulk self-focussing or surface melting. This  $I_{MAX}$  can vary dramatically from substrate to substrate. As long as the IR input is within the intense region of the pump beam focus, further focussing of the IR will not result in larger signal.

Equation (11) can be used to obtain a numerical estimate of the signal strength. Equations (4) and (5) can be used to obtain an estimate of  ${}^s\chi_{ijk}^{(2)}$ . One finds  ${}^s\chi_{ijk}^{(2)} = 10^{-15} \text{esu}$ .<sup>7</sup> Using  $\omega_{sf} = 21750 \text{ cm}^{-1}$ ,  $\omega_{IR} = 2950 \text{ cm}^{-1}$ , and  $I_{VIS} = 20 \text{ GW/cm}^2$ , one finds  $\eta = 4.25 \times 10^{-12}$ . For an IR input of  $100 \mu\text{J}$ ,  $N_{IR} = 2 \times 10^{15}$  photons. This gives  $N_{SF} = 8.5 \times 10^3$ .

Vibrational spectroscopy has proven to be one of the best means of probing molecular materials, in particular molecular adsorbates.<sup>2</sup> For this reason, one of the input frequencies for SFG should be tunable in the IR, where molecular vibrations are present. Since the output will typically be in the range of  $10^2$  to  $10^4$  photons per laser shot, photomultiplier sensitivity will be required. Consequently, the second input beam should be at a visible input, so that the sum-frequency signal will also be in the visible where PMT's have optimum quantum efficiencies.

## B. Experimental Set-Up

To this end, the laser system was constructed to produce high intensity pulses at a fixed visible wavelength and a tunable range in the near IR. Specifically, an active/passive mode-locked Nd:YAG oscillator, single pulse selector, amplifier combination was used to generate a visible input at  $.532 \mu\text{m}$  by SHG in KD\*P and a tunable IR input in the vicinity of  $3.4 \mu\text{m}$  by optical parametric amplification in  $\text{LiNbO}_3$ .<sup>11</sup> The details of the system construction are delineated in chapter I.

The experimental set-up is shown in figure 1. At the sample, the  $.532\mu\text{m}$  output is approximately  $1\text{mJ}$  per pulse and the IR is approximately  $100\mu\text{J}$  per pulse. Both pulses are approximately  $15\text{ps}$  in duration and were focussed to a common spot of  $350\mu\text{m}$  diameter. The initial experimental alignment was performed on a quartz surface which was co-planar with the sample surface. The lack of a center of inversion in quartz allows a bulk contribution which will generate a reflection SFG approximately  $10^3$  times larger than the "pure" surface signal. The beam overlap and subsequent alignment of detection optics can be optimized on the quartz. The system response (as the infra-red frequency is tuned) can also be determined, so that it can be normalized out of the data. The quartz and sample mounts were on the same translation stage, so that after the alignment was completed on the quartz, the sample could be translated into place, maintaining the optimized alignment achieved on



the quartz. For any of the interfaces studied, a nearly collinear beam geometry was used in which the visible and IR beams were incident on the sample at  $50^\circ$  and  $55^\circ$  degrees respectively with respect to the interface normal (see figure 1). The IR input was filtered with an AR-coated polished piece of Ge which removed both the  $1.5\mu\text{m}$  output produced by the optical parametric amplifier and any other visible light which was coincident with the optical parametric amplifier path. The  $5^\circ$  angular separation was sufficient to allow the spatial filtering of the reflected input light from the SFG signal. Subsequent spectral filtering was accomplished with an interference filter and monochromator. The signal was detected with a Hamamatsu 955 PMT whose output was electronically gated, digitized and collected on an Apple computer. To provide normalization of the data, a small portion of the inputs were split off to a focus in a thin quartz piece. The bulk sum-frequency signal from the quartz was large enough to provide a means to eliminate both the laser power fluctuations and the experimental response of the system. The computer also controlled the tuning of the IR frequency.

The IR radiation was calibrated by linear adsorption in a  $\text{CH}_4$  cell. The IR bandwidth was approximately  $6\text{cm}^{-1}$ . This was also the limiting bandwidth in the SFG technique, since the input at  $.532\mu\text{m}$  had a bandwidth much less than  $1\text{cm}^{-1}$ .

### C. Resulting Data

To demonstrate the feasibility of the SFG technique, a series of three alcohols at an air-glass interface were studied.<sup>12</sup> The alcohols in question, methanol, isopropyl alcohol, and ethylene glycol, were chosen because of the ease of their simple preparation as well as their distinctive spectral responses in the IR range of the OPA output. Each C-H stretch individually lacks a center of symmetry in its vibration. Infrared and Raman bulk spectra show that the vibrations in question are all both IR and Raman active and consequently accessible by the SFG technique.<sup>13</sup> In the preparation of each sample, the glass substrate

was thoroughly cleaned in oxidizing solution to remove hydrocarbon contaminants. (This oxidizing solution was composed of equal volumes of sulfuric acid (98%) and hydrogen peroxide (30%)). The SFG spectrum of the clean glass substrate was very weak and showed little structure. The samples were evaporated from a closed cell directly below the glass substrate. This ensured that only the alcohol in question adsorbed to the substrate. With these precautions the vibrational spectrum of the adsorbed molecules of each alcohol could be measured.

The output signal was highly directional and well-collimated as anticipated. The peak methanol, isopropyl alcohol, and ethylene glycol signals respectively were approximately  $2 \times 10^4$ ,  $6 \times 10^2$ , and  $1 \times 10^2$  SFG photons per pulse. The monochromator was changed to wavelength settings both above and below the SFG wavelength to assure that the signal was being produced only at wavelength expected.

#### D. Interpretation

Figure 2 displays the SFG spectra of the three adsorbed molecular species together with their Raman spectra from bulk liquid.<sup>13</sup> The close agreement between the Raman and SFG spectra allows us to assign unambiguously the observed peaks in the SFG spectra.

In figure 2a, for methanol  $\text{CH}_3\text{OH}$  on glass, two peaks at  $2840\text{cm}^{-1}$  and at  $2960\text{cm}^{-1}$  correspond to the  $\text{CH}_3$  symmetric and asymmetric stretch vibrations, respectively. In figure 2b, for ethylene glycol,  $\text{C}_2\text{H}_4(\text{OH})_2$ , the symmetric and asymmetric  $\text{CH}_2$  stretches appear at  $2875$  and  $2935\text{cm}^{-1}$ , respectively. In figure 2c, for isopropyl alcohol,  $(\text{CH}_3)_2\text{CHOH}$ , the peak at  $2885\text{cm}^{-1}$  is assigned as the  $\text{CH}_3$  symmetric stretch, the two peaks at  $2950\text{cm}^{-1}$  and  $2980\text{cm}^{-1}$  are assigned as the degeneracy-lifted  $\text{CH}_3$  asymmetric stretches, and the little bump at  $2920\text{cm}^{-1}$  is assigned as the  $\text{CH}$  stretch. All the spectra were taken with the visible light s-polarized and the infrared light unpolarized. It is seen that the spectra for the three alcohols are distinctly different, and various C-H stretches are clearly

distinguishable.

The methanol spectrum appeared to have changed in a few hours after the sample was prepared, as shown in figure 3. This suggests that the methanol might have been transformed into another molecular species, presumably methoxy,  $\text{CH}_3\text{O}$ .<sup>10</sup> (The substance is presumed to be methoxy because the methyl stretch resonances have shifted to higher frequency values.) The result is a manifestation of the capability of SFG to monitor surface molecular reactions. It was also found that after leaving the alcohol-covered samples in air for a while, the isopropyl alcohol spectrum would disappear, but the other two would not. This indicates that only isopropyl alcohol is desorbed completely from the glass surface and explains why it is often used as the solvent for cleaning glass.

Obviously, the limited range of the OPA does not allow one to obtain sufficiently distinct IR spectra to make a positive identification of an unknown molecule placed at the interface. The IR range of the optical parametric amplifier ( $>2500\text{cm}^{-1}$ ) allows one only to excite C-H, N-H, and O-H stretches.<sup>14</sup> The spectral range usually used for molecular identification is that between  $1400\text{cm}^{-1}$  to  $1900\text{cm}^{-1}$ . However, this series of experiments indicates that identification is possible in principle. As new nonlinear crystals extend the range of parametric generation to longer IR wavelengths, more complete vibrational spectroscopic measurements will be made.

## References

1. Y.R. Shen, in: New Laser and Optical Investigation of Chemistry and Structure of Interfaces, eds. R. B. Hall and A. B. Ellis (Verlag Chemie, Weinheim, 1986) p. 151; *Ann. Rev. Mat. Sci.* 16 (1986) 69.
2. R.F. Willis, Springer series in chemical physics, Vol. 15. Vibrational Spectroscopy of Adsorbates (Springer, Berlin, 1980).
3. H.Ibach and D.L. Mills, Electron Energy Loss Spectroscopy and Surface Vibrations (Academic, New York 1982).
4. F. Traeger, H. Coufal, and T.J. Chuang, *Phys. Rev. Lett.* 49, 1720 (1982).
5. J.H. Hunt, P. Guyot-Sionnest, Y.R. Shen, *Chem. Phys. Lett.* 133 189 (1987).
6. H.W.K. Tom, Ph.D. thesis, University of California, Berkeley, 1984 (unpublished).
7. X.D. Zhu, H. Suhr, and Y.R. Shen, *Phys. Rev. B* 35 3047 (1987).
8. T.F. Heinz, H.W.K. Tom, Y.R. Shen, *Phys. Rev. A* 28 1883 (1983).
9. Y.R. Shen, The Principles of Nonlinear Optics (Wiley, New York, 1984) p.171.
10. G. Herzberg, Molecular Spectra and Molecular Structure II (Van Nostrand Reinhold Co., 1945), p.239-243.
11. see, for example, H. Graener and A. Laubereau, *Appl. Phys.* B29 (1982) 213.
12. J.H. Hunt, P. Guyot-Sionnest, Y.R. Shen, in Laser Spectroscopy VIII, Proceedings of the Eighth International Conference on Laser Spectroscopy, Are, Sweden.
13. Selected Raman Spectral Data, ed. L.B. Beach (Thermodynamic Research Center Hydrocarbon Project Publications, College Station, Texas, 1983), Ser. No. 807, 653, 55.
14. see, for example, Randall et. al. "Infra-Red Determination of Organic Structures," (Van Nostrand, New York, 1949).

### Figure Captions

Fig. 1 Experimental set-up for SFG, including both the sample and reference arms.

Fig. 2 Sum-Frequency Generation spectra as a function of infra-red input frequency. The bold lines are the bulk liquid Raman spectra.

Fig. 3 Sum-Frequency Generation spectrum of methanol on glass of a fresh sample and an old sample. The latter was taken several hours after deposition.

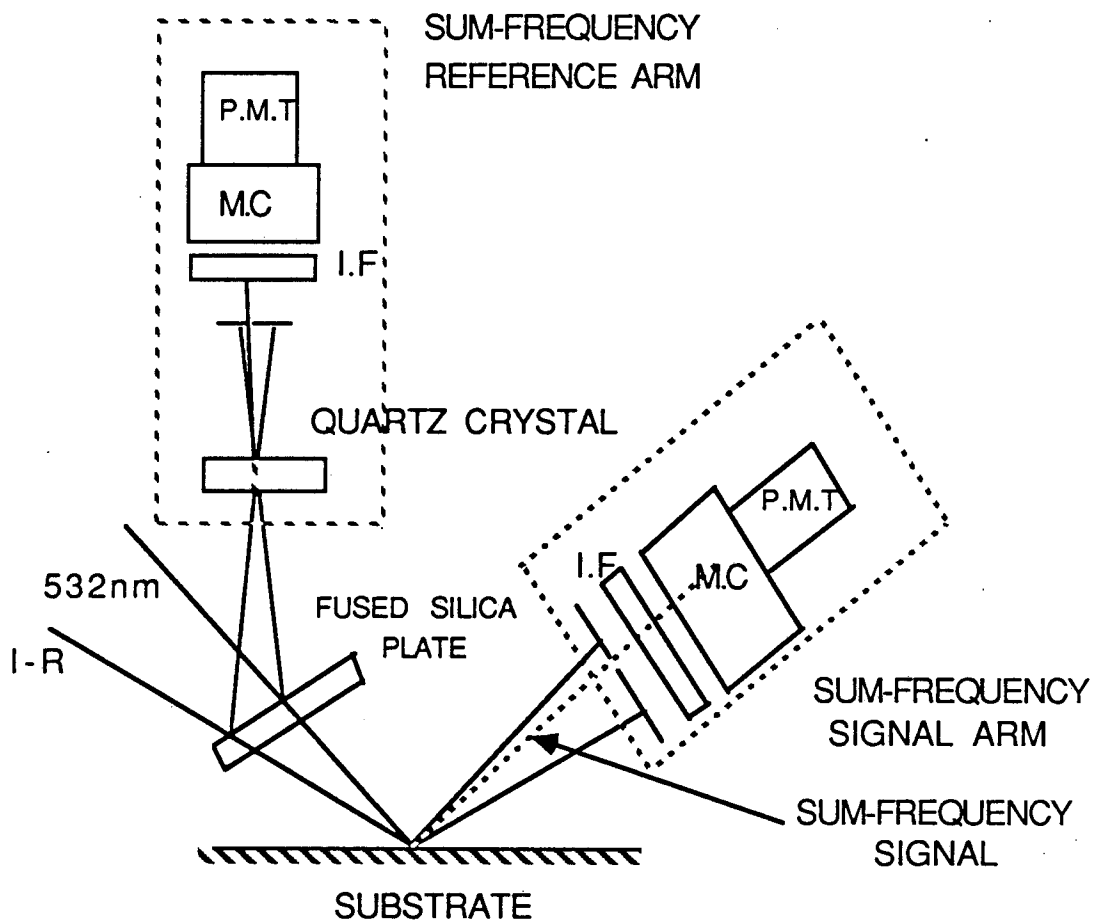


Figure 1

XBL-881-116

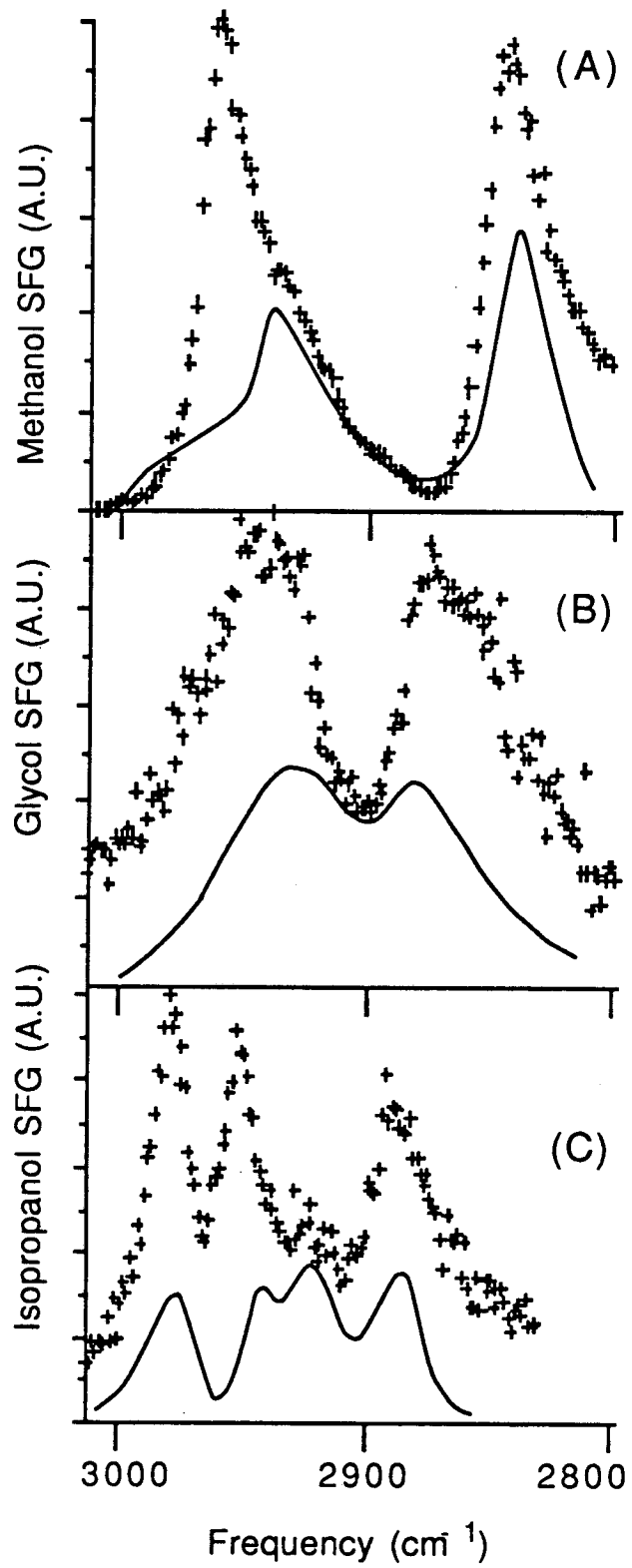


Figure 2

XBL-881-117

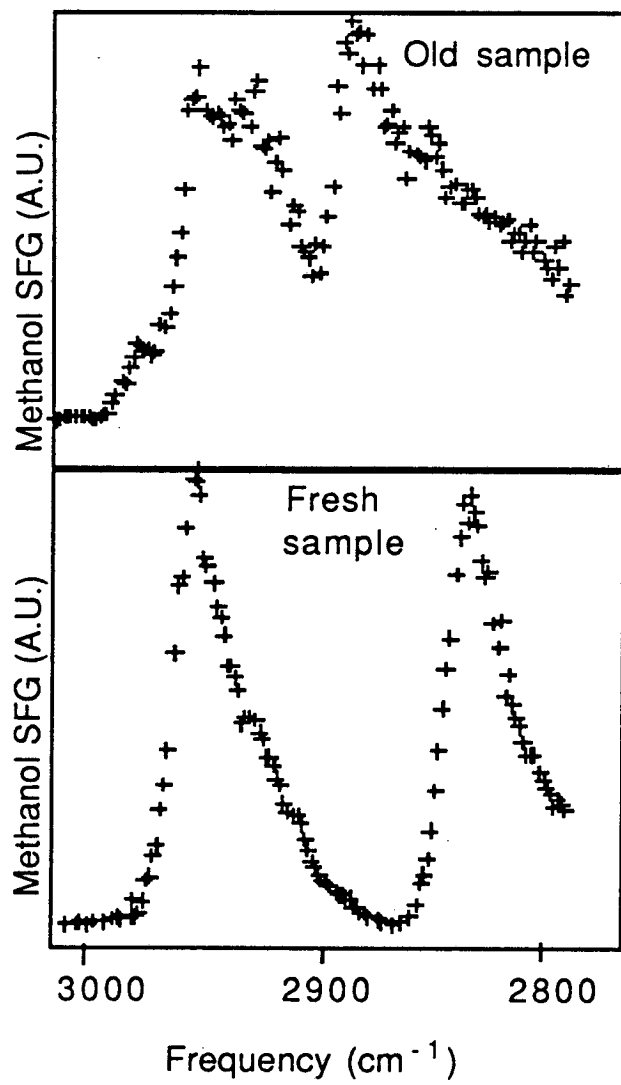


Figure 3

XBL-881-118



## IV. Sum Frequency Generation Spectroscopy of Pentadecanoic Acid at an Air/Water Interface

### A. Introduction

In this chapter, it will be shown that by using surface SFG, information about the microscopic properties of Langmuir films can be deduced.<sup>1</sup> The so-called Langmuir film formed by long-chain molecules spread on water is of great interest to many researchers because of their relevance to cell membranes and molecular electronics.<sup>2</sup> Such systems often exhibit a gas phase at low density, a liquid expanded phase (LE) phase at intermediate density, and a liquid condensed (LC) phase at high density.<sup>3</sup> The nature of the first-order transition between the LE and LC phases is the subject of many recent investigations.<sup>4-8</sup> There had been some dispute as to whether the phase transition was associated with the "melting" of the tail or a reorientation of the head group. (An excellent review of the state of theoretical understanding prior to 1981 can be found in a review article by Bell, Combs, and Dunne.)<sup>8</sup> Traditionally, this phase transition was studied by surface tension and potential measurements giving little microscopic information. However, new techniques probing the microscopic features of the transition have recently been developed.<sup>4-6</sup> Optical second harmonic generation (SHG) has found that the molecular polar head groups reorient themselves upon surface compression.<sup>5</sup> However, the degree of extension, orientation, and alignment of the molecular chains in the two phases has not yet been well investigated for lack of experimental tools. This is the first application of surface SFG to the study of a molecular monolayer at an air/liquid interface.

### B. Theoretical Considerations

If one rewrites chapter II equation (5) to specifically include the molecular orientational projections, then the surface susceptibility  $S\chi^{(2)}$  is given by

$$s\chi^{(2)}_{ijk} = N_s \sum_{i'j'k'} \alpha^{(2)}_{i'j'k'} \langle (i'i) (j'j) (k'k') \rangle \quad (1)$$

where  $N_s$  is the surface molecular density. The primed coordinates are those of the molecule; the unprimed coordinates are those of the laboratory frame. When the resonant contribution of a particular mode dominates at a certain frequency, measuring the components of the surface nonlinearity allows one to determine the orientational order parameters of that mode. Note that the relationship between different elements of  $\chi^{(2)}$  can be obtained by projecting the  $\alpha^{(2)}$  elements onto the laboratory coordinates.

To determine the allowed surface susceptibility terms one must examine the symmetry of the surface. If  $Z$  is the surface normal and if it is assumed that the surface is isotropic, then there is inversion symmetry in the plane. This immediately implies that any  $\chi^{(2)}$  term having an odd number of  $X$ 's or  $Y$ 's must vanish. Consequently, the nonvanishing components of  $\chi^{(2)}$  are

$$\begin{aligned} \chi^{(2)}_{ZZZ}; \quad \chi^{(2)}_{XXZ} = \chi^{(2)}_{YYZ}; \\ \chi^{(2)}_{XZX} = \chi^{(2)}_{YZY}; \quad \chi^{(2)}_{ZXX} = \chi^{(2)}_{ZYY}. \end{aligned} \quad (2)$$

In the limit when  $\omega_{SF}$  and  $\omega_{VIS}$  are both far from resonance, there is the additional relation  $\chi^{(2)}_{XZX} = \chi^{(2)}_{ZXX}$ .

One should note that certain input polarization combinations will interact with certain  $\chi^{(2)}$  elements. For both inputs s-polarized, only  $\chi^{(2)}_{ZXX}$  will contribute (with  $Z$  normal to the surface,  $k$ -vectors in the  $Z$ - $Y$  plane), so that the output polarization must be p-polarized. For both inputs p-polarized,  $\chi^{(2)}_{ZZZ}$  and  $\chi^{(2)}_{ZYY}$  can contribute, so that the output polarization must be p-polarized. An s-polarized visible input and p-polarized infra-red input will interact only through  $\chi^{(2)}_{XXZ}$ , so that the output polarization will be s-polarized. A p-polarized visible input and s-polarized infra-red input will interact only through  $\chi^{(2)}_{XZX}$ , so that the output polarization will be s-polarized. Any deviations from these polarization

rules would indicate the presence of an anisotropic surface.

### C. Experimental Considerations

In our experiment, a system of a monolayer of PDA spread on water was prepared by depositing a measured amount of PDA dissolved in petroleum ether onto a thoroughly cleaned water surface (pH=2), and waiting until the ether had evaporated. PDA is a weak acid. Estimates of its dissociation constant indicate that the acid group will be 96% dissociated when it is spread on a neutral substrate.<sup>9</sup> When spread on a distilled water surface the dissociation will depend on the amount of CO<sub>2</sub> dissolved in the water, since its presence changes the acidity of the water substrate. If the molecule is dissociated, it can react with metallic ions present in the water. These reactions will modify the interaction between the individual PDA molecules and between the molecules and the substrate. This could greatly affect the appearance of the phase transition diagram. In order to prevent such effects, pure HCl was included in the water to reduce its pH to 2. Under these conditions the film is only .03% dissociated.<sup>9</sup>

The water substrate was prepared in a Langmuir trough. In this case, the trough was a glass "tub" which had its edges coated with a teflon tape. The teflon edge allows the water to be filled several millimeters above the edge of the trough. Cleaning of the water surface is accomplished by "vacuuming" the surface through a hypodermic needle. Eventually, enough material is removed from the water surface so that a spectrum taken with the SFG technique gives a very small signal with little structure.

The solvent for the PDA must also be cleaned since several hundred microliters of it is deposited on the surface over the course of the film build-up. Petroleum ether contains impurities which have spectral features in the range of the PDA features. Although the petroleum ether eventually evaporates, the impurities do not. It was found that if untreated petroleum ether were deposited on the surface in amounts normally used in the build-up of a full film, the impurities left on the surface resulted in the presence of a considerable

background. This would interfere with the PDA resonances.

The impurities could be eliminated by singly distilling the petroleum ether. The distillation apparatus consisted of two flasks, connected by a long (2 meter) tube with a 90° bend in it. One end was placed on a hot plate and the other was placed in an ice bath. The distillation took only a few minutes to purify 500 ml of the solvent. There was considerable residue left in the starting flask after the evaporation was complete. After applying the distilled ether to the water substrate, there was no detectable background signal produced. The surface pressure ( $\pi$ ) of the system was monitored by using the Wilhelmy plate method.<sup>3</sup> The plate, a thin piece of platinum, is hung from a balance, suspended so that it is partially submerged in the water. (The plate is first cleaned by placing it in a flame until it glows red.) As the coverage changes, there will be a change in the pull on the plate,  $\Delta w$ . The surface pressure is then given by

$$\pi = \Delta w p, \quad (3)$$

where  $p$  is the perimeter of the slide.

The surface pressure as a function of area per molecule at 28.5°C is shown in figure 1. The visible beam was focussed on the surface at an angle of 52° and the IR at 58° to a common area of .1mm<sup>2</sup>. At full monolayer coverage of PDA, the peak signal was ~500 photons/pulse with a signal-to-noise ratio of 10<sup>3</sup>. The IR frequency was calibrated to 1.5cm<sup>-1</sup> using the methane absorption spectrum and the IR laser linewidth was 6cm<sup>-1</sup>. The SFG polarization rules that were discussed in the last paragraph of section B were strictly obeyed. This indicated azimuthal symmetry of the molecular orientation as expected.

The basic optical experimental alignment set-up is the same as in figure 1 in chapter III. The only difference is that here the "substrate" is the pH=2 water surface.

#### D. Interpretation I: High Density Case

The first focus of attention will be the spectra (fig 2) taken with various input polarization combinations at the highly compressed end of the LC phase (point c in fig 1). This allows the identification of the C-H stretches in the SFG spectra. Only the terminal CH<sub>3</sub> group is expected to contribute strongly; the CH<sub>2</sub> groups distributed along a straight alkane chain have their contribution nearly cancelled by one another because of inversion symmetry.

The IR and Raman spectra of the methyl group have been extensively studied in bulk alkanes.<sup>10</sup> They consist of a symmetric s-stretch at 2875cm<sup>-1</sup> corresponding to a change of the dipole moment along the symmetric z axis of the CH<sub>3</sub> group (along the C-C bond; see figure 2) and two nearly degenerate modes, the d<sub>x</sub>-stretch at 2962cm<sup>-1</sup> and the d<sub>y</sub>-stretch at 2954cm<sup>-1</sup>, corresponding to changes of the dipole moment in and out of the plane of the alkane chain, respectively. An additional peak at 2935cm<sup>-1</sup> is usually attributed to a Fermi resonance of the s-stretch with the overtones of the methyl-bending modes.<sup>11</sup>

(Combinations or harmonics of lower lying vibrational excitations can be excited if the sum- or harmonic- frequency coincides with the infra-red input frequency. Normally these excitations are very small in amplitude. However, if these combinations or harmonics are accidentally degenerate with higher frequency fundamental excitations, the amplitude of these combination or harmonic excitations can be enhanced, resulting in a Fermi resonance.<sup>12</sup> The only restriction is that the lower lying levels must be of the same symmetry group as the higher one.) Our spectra in figure 2 exhibit the CH<sub>3</sub> stretch peaks in the expected regions except that the one attributed to Fermi resonance appears to be shifted to 2940cm<sup>-1</sup>. This relatively large shift (5cm<sup>-1</sup>) is presumably the result of the high sensitivity of the Fermi resonance to the change of the environment (i.e. from bulk to surface). Thus it is concluded that the methyl group dominates the spectra. As expected, different input polarizations give very different intensities for the various modes and this feature can be used to determine the orientation of the methyl group. The methyl group has an approximate C<sub>3v</sub> symmetry. Then, for both s- and d-stretches, there are only two independent components for the

nonlinear susceptibility  $\alpha^{(2)}_{\nu}$  (see Table I).

Having identified the features in the spectrum, an analysis will now be made to determine the effect of the input polarizations on the s-stretch intensity. This dependence will be used to determine the orientation of the hydrocarbon tail with respect to the water surface. Using the known angle of  $109^{\circ}$  between between the C-C and C-H bonds, the two independent components  $\alpha^{(2)}_{s,zzz}$  and  $\alpha^{(2)}_{s,xxz}$  of  $\alpha^{(2)}_s$  for the s-stretch mode can be related. Suppose  $\alpha^{(2)}_{\xi\xi\xi}$  is the second order polarizability associated with the symmetric stretching C-H along the bond direction. A simple projection of  $\alpha^{(2)}_s$  onto the methyl group coordinates (lower case subscripts) gives

$$\alpha^{(2)}_{s,zzz} = \cos^3(\pi-\Omega) \alpha^{(2)}_{\xi\xi\xi} \quad (4a)$$

and

$$\alpha^{(2)}_{s,xxz} = \sin^2(\pi-\Omega) \cos(\pi-\Omega) \sin^2(\Phi) \alpha^{(2)}_{\xi\xi\xi}, \quad (4b)$$

where  $\Omega=109^{\circ}$  is the angle between the C-H bond and the C-C bond and  $\Phi$  is the azimuthal angle in that coordinate system. (It should be noted that because of the definition of the methyl group coordinates, the angle between the C-H bond and the z-axis is  $\pi-\Omega$ .)

Consequently,

$$\alpha^{(2)}_{s,zzz} = 2[\cot^2(109^{\circ})] \alpha^{(2)}_{s,xxz}, \quad (5)$$

where  $\Phi$  has been averaged over orientation. A similar method has been used to calculate the Raman depolarization ratio with reasonable success.<sup>12</sup>

Recall that it is possible to relate the  $\alpha^{(2)}_s$  components to the surface susceptibility by projecting the  $\alpha^{(2)}_s$  components onto the laboratory coordinates via the Euler angles.

Since the s-polarized visible p-polarized infra-red and p-polarized visible s-polarized infra-red combinations involve only one  $\chi^{(2)}$  term each, only those will be shown here.

Writing  $\chi$  in terms of the Euler projections and the  $\alpha$  components, one finds

$$\begin{aligned}\chi_{YZY} = & \langle (\mathbf{Y} \cdot \mathbf{z}) (\mathbf{Z} \cdot \mathbf{z}) (\mathbf{Y} \cdot \mathbf{z}) \rangle \alpha_{zzz} + \\ & + \langle (\mathbf{Y} \cdot \mathbf{x}) (\mathbf{Z} \cdot \mathbf{x}) (\mathbf{Y} \cdot \mathbf{z}) \rangle \alpha_{xxz} + \\ & + \langle (\mathbf{Y} \cdot \mathbf{y}) (\mathbf{Z} \cdot \mathbf{y}) (\mathbf{Y} \cdot \mathbf{z}) \rangle \alpha_{yyz}\end{aligned}\quad (6a)$$

and

$$\begin{aligned}\chi_{YYZ} = & \langle (\mathbf{Y} \cdot \mathbf{z}) (\mathbf{Y} \cdot \mathbf{z}) (\mathbf{Z} \cdot \mathbf{z}) \rangle \alpha_{zzz} + \\ & + \langle (\mathbf{Y} \cdot \mathbf{x}) (\mathbf{Y} \cdot \mathbf{x}) (\mathbf{Z} \cdot \mathbf{z}) \rangle \alpha_{xxz} + \\ & + \langle (\mathbf{Y} \cdot \mathbf{y}) (\mathbf{Y} \cdot \mathbf{y}) (\mathbf{Z} \cdot \mathbf{z}) \rangle \alpha_{yyz},\end{aligned}\quad (6b)$$

where  $\langle \rangle$  indicates an orientational average. Using the Euler angle projections that are given in Table II, one finds

$$\begin{aligned}\chi_{YZY} = & \langle \cos^2 \psi \sin^2 \theta \cos \theta \rangle \alpha_{zzz} + \\ & + \langle (-\sin \psi \cos \phi - \cos \theta \sin \phi \cos \psi)(\sin^2 \theta \sin \phi \cos \psi) \rangle \alpha_{xxz} + \\ & + \langle (\sin \psi \sin \phi - \cos \theta \cos \phi \cos \psi)(\sin^2 \theta \cos \phi \cos \psi) \rangle \alpha_{yyz}\end{aligned}\quad (7a)$$

and

$$\begin{aligned}\chi_{YYZ} = & \langle \cos^2 \psi \sin^2 \theta \cos \theta \rangle \alpha_{zzz} + \\ & + \langle (-\sin \psi \cos \phi - \cos \theta \sin \phi \cos \psi)(-\sin \psi \cos \phi - \cos \theta \sin \phi \cos \psi)(\cos \theta) \rangle \alpha_{xxz} + \\ & + \langle (-\sin \psi \sin \phi + \cos \theta \cos \phi \cos \psi)(-\sin \psi \sin \phi + \cos \theta \cos \phi \cos \psi)(\cos \theta) \rangle \alpha_{yyz}.\end{aligned}\quad (7b)$$

Upon simplifying the expressions, one finds

$$\begin{aligned} \chi_{YZY} = & \langle \cos^2\psi \sin^2\theta \cos\theta \rangle \alpha_{ZZZ} + \\ & + \langle -\sin\psi \cos\psi \sin^2\theta \cos\phi \sin\phi - \cos^2\psi \cos\theta \sin^2\theta \sin^2\phi \rangle \alpha_{XXZ} + \\ & + \langle \sin\psi \cos\psi \sin\phi \sin^2\theta \cos\phi - \cos^2\psi \sin^2\theta \cos\theta \cos^2\phi \rangle \alpha_{YYZ} \end{aligned} \quad (8a)$$

and

$$\begin{aligned} \chi_{YYZ} = & \langle \cos^2\psi \sin^2\theta \cos\theta \rangle \alpha_{ZZZ} + \\ & + \langle \sin^2\psi \cos\theta \cos^2\phi + \cos^2\psi \cos^3\theta \sin^2\phi + 2\sin\psi \cos\psi \cos^2\theta \cos\phi \sin\phi \rangle \alpha_{XXZ} + \\ & + \langle \sin^2\psi \cos\theta \sin^2\phi + \cos^2\psi \cos^3\theta \cos^2\phi - 2\sin\psi \cos\psi \cos^2\theta \cos\phi \sin\phi \rangle \alpha_{YYZ}. \end{aligned} \quad (8b)$$

By using the fact that  $\alpha_{XXZ} = \alpha_{YYZ}$  (see Table I), one finds that

$$\begin{aligned} \chi_{YZY} = & \langle \cos^2\psi \sin^2\theta \cos\theta \rangle \alpha_{ZZZ} + \\ & + \langle -\cos^2\psi \cos\theta \sin^2\theta \rangle \alpha_{XXZ} \end{aligned} \quad (9a)$$

and

$$\begin{aligned} \chi_{YYZ} = & \langle \cos^2\psi \sin^2\theta \cos\theta \rangle \alpha_{ZZZ} + \\ & + \langle \sin^2\psi \cos\theta + \cos^2\psi \cos^3\theta \rangle \alpha_{XXZ}. \end{aligned} \quad (9b)$$

As is seen in Table I,  $\alpha_{ZZZ}$  and  $\alpha_{XXZ} = \alpha_{YYZ}$  are the two independent components of the s-stretch mode of the methyl group. Because of the relation in equation (5) between  $\alpha_{ZZZ}$  and  $\alpha_{XXZ}$  there is now only one independent component. With only one independent component in  $\alpha^{(2)}_s$ , it is easy to find the orientation of the methyl group from the ratio of the two components of  $\chi^{(2)}$ . In the above expressions,  $\theta$  is the angle between the C-CH<sub>3</sub> axis and the surface normal. Using the above relations for  $\chi_{YZY}$  and  $\chi_{YYZ}$  and the relation between  $\alpha_{ZZZ}$  and  $\alpha_{XXZ}$  (equation (5)) one finds that



$$\begin{aligned}
\chi_{YZY} &= 2[\cot^2(109^\circ)] \langle \cos^2\psi \sin^2\theta \cos\theta \rangle \alpha_{XXZ} + \\
&+ \langle -\cos^2\psi \cos\theta \sin^2\theta \rangle \alpha_{XXZ} = \\
&[2\cot^2(109^\circ) - 1] \langle \cos^2\psi \sin^2\theta \cos\theta \rangle \alpha_{XXZ}
\end{aligned} \tag{10a}$$

and

$$\begin{aligned}
\chi_{YYZ} &= 2[\cot^2(109^\circ)] \langle \cos^2\psi \sin^2\theta \cos\theta \rangle \alpha_{XXZ} + \\
&+ \langle \sin^2\psi \cos\theta + \cos^2\psi \cos^3\theta \rangle \alpha_{XXZ} = \\
&\langle \{2[\cot^2(109^\circ)]\cos^2\psi + \sin^2\psi\} (\sin^2\theta \cos\theta) + \cos^3\theta \rangle \alpha_{XXZ},
\end{aligned} \tag{10b}$$

where the expression  $\cos\theta = \cos^3\theta + \sin^2\theta \cos\theta$  was used. Taking  $\psi$  to be isotropically distributed, one has the angular averages  $\langle \cos^2\psi \rangle = \langle \sin^2\psi \rangle = .5$ . Using these averages and the fact that  $\cot(109^\circ) = -.344$ , one finds, upon taking the ratio between  $\chi_{YYZ}$  and  $\chi_{YZY}$ , that

$$\chi_{YYZ}/\chi_{YZY} = [\langle \cos^3\theta \rangle + .62\langle \sin^2\theta \cos\theta \rangle] / [.38\langle \sin^2\theta \cos\theta \rangle]. \tag{11}$$

To analyze the results in figure 2 it is noted that  $\chi_{YYZ}/\chi_{YZY} = (I_{sp}/I_{ps})^{1/2}$ , where  $I_{ps}$  is the intensity taken with p-polarized visible and s-polarized IR and  $I_{sp}$  is the intensity taken with s-polarized visible and p-polarized IR. The intensity of the  $I_{ps}$  peak is fairly small, so it is difficult to trust the peak signal height. Working from the figure, two extremes values are taken; using the height of the small peak as an upper limit on  $I_{ps}$ , one finds  $I_{sp}/I_{ps} = 18$ ; using the surrounding nonresonant background as a lower limit, one finds  $I_{sp}/I_{ps} = 70$ . These two limits were used to make sure that the actual  $\theta$  value would lie in this range. Using these two extremes in equation (11), one finds that

$$1.0 < \{ \langle \cos^3\theta \rangle / \langle \cos\theta \sin^2\theta \rangle \} < 2.6 \tag{12}$$

corresponding to  $45^\circ > \theta > 32^\circ$  if a  $\delta$ -function is assumed for the orientational distribution.

The above result suggests that for a full monolayer of PDA, on water, the alkane chain of the molecules stands nearly vertically on the surface, as this leads to  $\theta = 35^\circ$  for methyl group s-stretch. The data are consistent with a chain orientation that has a distribution of tilt between  $10^\circ$  and  $0^\circ$  about the surface normal. Infrared studies have shown that fatty acid on solid substrates have the chain tilted at  $(25 \pm 4)^\circ$  or  $(60 \pm 4)^\circ$  for the methyl group.<sup>13</sup> Fatty acid salts, however, were found to be oriented nearly normal to the substrate.<sup>14</sup> In the latter case, LEED studies indicate that the chains are oriented with a dominant tilt angle of  $8^\circ$  from the surface normal.<sup>15</sup> A similar analysis of our spectra could be made for the d-stretch. Unfortunately, we could not resolve the  $d_x$  and  $d_y$  modes. The presence of two independent components of  $\alpha^{(2)}_d$  makes an unambiguous interpretation difficult.

#### E. Interpretation II: Low Density Case

At this point, attention should be focussed on the spectra with different surface coverages, shown in figure 3. In the LC-LE coexistence region ( $23\text{-}31\text{A}^2/\text{molecule}$ ), there are strong fluctuations of the SFG signal. Because it is a coexistence regime, there are small "islands" of closely packed molecules within a lake of farther separated liquid molecules.<sup>5</sup> These "islands" can drift into or out of the laser input over the course of the data acquisition time. Since the spectral responses of the two phases are quite different, there will be data-point-to-data-point fluctuations if the SFG spectrum is attempted in this region. Therefore the LE phase was studied, taking complete spectra close to the two ends of this phase, namely points a and b in figure 1.

The most striking result is the appearance of a strong  $\text{CH}_2$  s-stretch signal at  $2850\text{cm}^{-1}$  as well as a broad background also attributable to the  $\text{CH}_2$  stretches in the  $2930\text{-}2880\text{cm}^{-1}$  range in the spectra. These must arise from a weakening of the selection

rules on the CH<sub>2</sub> modes along the alkane chain. For a straight chain, near inversion symmetry leads to a near cancellation of the different CH<sub>2</sub> contributions. When this symmetry is broken, the CH<sub>2</sub> modes become observable.

The most likely reason for such a symmetry breaking is a trans-gauche conformation which effectively would lead to a kink in the hydrocarbon chain. In the lowest energy state of a saturated hydrocarbon chain, each successive carbon-carbon bond is at the "trans" angle with respect to the previous bond.<sup>16</sup> This is the lowest energy configuration because it positions the CH<sub>2</sub> groups as far away from each other as possible (see figure 4). This implies that the carbon atoms in the chain are all co-planar. This configuration gives the minimum volume and allows the closest packing of the molecules. However, the carbon-carbon bond can rotate to two other gauche (out-of-plane) bond angles which are separated in energy by .022eV per molecule (see figure 4). These conformations are of slightly higher energy because they result in the CH<sub>2</sub> groups being positioned closer together. The rotation about the C-C bond leads to a van der Waals repulsion (or steric repulsion) between the CH<sub>2</sub> groups. Other intermediate angles are possible. But due to torsional strain in the molecule these require higher energies (.13 to .26 eV per molecule) than are available at room temperature (.025eV per molecule). After this trans-gauche conformation the carbon atoms are no longer co-planar and the chain is bent.

In the full layer, the molecules are constrained to occupy a minimum volume due to the steric interaction with neighboring molecules. As the area per molecule is increased, this gauche deformation becomes much more likely. These transformations have been proposed in many theoretical models attempting to explain the LE-LC transition.<sup>20</sup> The decrease of the background and the mode at  $2850\text{cm}^{-1}$  from a to b indicates that as the monolayer is compressed, the number of trans-gauche transformations is reduced (the chain is straightened up). The intensities of the CH<sub>2</sub> structure are related to the trans-gauche deformation as follows; for each deformation, there is an unpaired CH<sub>2</sub> group created. It is the combined contribution of the number of trans-gauche and the average orientation of those groups along

the chain that determines the  $\text{CH}_2$  mode intensity in the spectrum. One could also argue for an increased water-alkane chain interaction. However, in view of the strong hydrophobicity of the alkane such an interaction is unlikely to significantly reduce the chain symmetry.

The deformation and the orientational disordering of the chain in the LE-phase are expected to lead also to a poorer orientational order of the terminal methyl group. This should appear as a decrease in the intensities of the  $\text{CH}_3$  peaks as is indeed seen in figure 3(1b) and 3(2b). Chain disordering has been observed at high temperatures ( $100^\circ\text{C}$ ) in Langmuir Blodgett films of fatty acid salts on solid substrates.<sup>17</sup> In contrast to the result presented here, the higher disordering temperature of those films is probably due to their closer packing ( $23\text{Å}^2/\text{mol}$ ) which would lead to a stronger steric interaction.

#### F. Conclusion

Infrared-visible sum-frequency generation has been used with various polarization combinations to obtain the vibrational spectra of the CH stretches for PDA Langmuir monolayers on water in their LE and LC phases. From the results it has been deduced that in the LC phase the long alkane chains of the PDA molecules are straight and oriented nearly normal to the water surface. In the LE phase, the chains are deformed and orientationally disordered.

Table I. Hyperpolarizability components for the various modes of the methyl group.

CH mode	$\nu(\text{cm}^{-1})$	IR dipole moment	$\alpha_{\nu,ijk}^{(2)}(\omega_{\text{SF}} = \omega_{\text{vis}} + \omega_{\text{IR}})$
s-stretch	2875	z	$\alpha_{zzz}; \alpha_{xxz} = \alpha_{yyz}$
d-stretch	2962	x	$\alpha_{xxx} = -\alpha_{yyz}; \alpha_{zxx} = \alpha_{xzx}$
d-stretch	2954	y	$\alpha_{xyy} = \alpha_{yxy}; \alpha_{zyy} = \alpha_{yzy}$

Table II. Euler angle projection matrix components

$$(\mathbf{X} \cdot \mathbf{x}) = \cos\psi \cos\theta - \cos\theta \sin\phi \sin\psi$$

$$(\mathbf{Y} \cdot \mathbf{x}) = -\sin\psi \cos\theta - \cos\theta \sin\phi \cos\psi$$

$$(\mathbf{Z} \cdot \mathbf{x}) = \sin\theta \sin\phi$$

$$(\mathbf{X} \cdot \mathbf{y}) = \cos\psi \sin\phi + \cos\theta \cos\phi \sin\psi$$

$$(\mathbf{Y} \cdot \mathbf{y}) = -\sin\psi \sin\phi + \cos\theta \cos\phi \cos\psi$$

$$(\mathbf{Z} \cdot \mathbf{y}) = -\sin\theta \cos\phi$$

$$(\mathbf{X} \cdot \mathbf{z}) = \sin\psi \sin\theta$$

$$(\mathbf{Y} \cdot \mathbf{z}) = \cos\psi \sin\theta$$

$$(\mathbf{Z} \cdot \mathbf{z}) = \cos\theta$$

## References

1. P. Guyot-Sionnest, J.H. Hunt, and Y.R. Shen, *Phys. Rev. Lett.* **59** 1597 (1987).
2. Proceedings of the Second International Conference on Langmuir-Blodgett Films, *Thin Solid Films* **132** (1986).
3. A. W. Adamson, *Physical Chemistry of Surfaces* (John Wiley, New York, 1982.)
4. K. Kjaer, J. Als-Nielsen, C.A. Helm, L.A. Laxhuber, H. Mohwald, *Phys. Rev. Lett.* **58**, 2224 (1987).
5. Th. Rasing, Y.R. Shen, M.W. Kim, and S. Grubb, *Phys. Rev. Lett.* **55**, 2903 (1985).
6. R. A. Dluhy, *Biophys. J.* **51**, 19a (1987).
7. N. R. Pallas and B.A. Pethica, *Langmuir* **1**, 509 (1985).
8. G.M. Bell, L.L. Coombs, and L.J. Dunne, *Chem. Rev.* **81**, 15 (1981).
9. M.W. Kim and D.S. Cannell, *Phys. Rev. A* **13** 411 (1976).
10. L.J. Bellamy, *The Infrared Spectra of Complex Molecules* (John Wiley, New York, 1975).
11. R.C. Spiker and I.W. Levin, *Biochim. Biophys. Acta* **338**, 361 (1975).
12. G. Herzberg, *Molecular Spectra and Molecular Structure II* (Van Nostrand Reinhold Co., 1945), p.247.
13. P. Chollet, J. Messier, and C. Rosilio, *J. Chem. Phys.* **64**, 1042 (1976).
14. D.L. Allara and J.D. Swalen, *J. Phys. Chem.* **86**, 2700 (1982).
15. S. Garoff, H.W. Deckman, J.H. Dunsmuir, M.S. Alvaerz, and J.M. Bloch, *J. Physique (Paris)* **47**, 701 (1986).
16. see, for example, R. T. Morrison and R. N. Boyd *Organic Chemistry* (Allyn and Bacon, Boston 1983).
17. C. Naselli, J. F. Rabolt, and J. D. Swalen, *J. Chem. Phys.* **82**, 2136 (1985).

## Figure Captions

- Fig. 1 Surface pressure of a monolayer of PDA on water as a function of area per molecule at  $T = 28.5^{\circ}\text{C}$ .
- Fig. 2 SFG spectra of PDA at full monolayer coverage using various (vis; IR) polarization combinations. 1) s-visible, p-IR, 2) p-visible, s-IR, 3) p-visible, p-IR. The lines simply connect the experimental data points (squares). The insert shows the coordinate axes chosen for the methyl group.
- Fig. 3 SFG spectra of PDA at different surface coverages normalized per molecule. 1(a) - (c) were taken with the (s-visible, p-IR) polarization combination. 2(a) - (c) were taken with the (p-visible, s-IR) polarization combination.
- Fig. 4 Schematic representation which demonstrates the difference between Trans and Gauche orientations of the carbon atoms in the hydrocarbon tail.



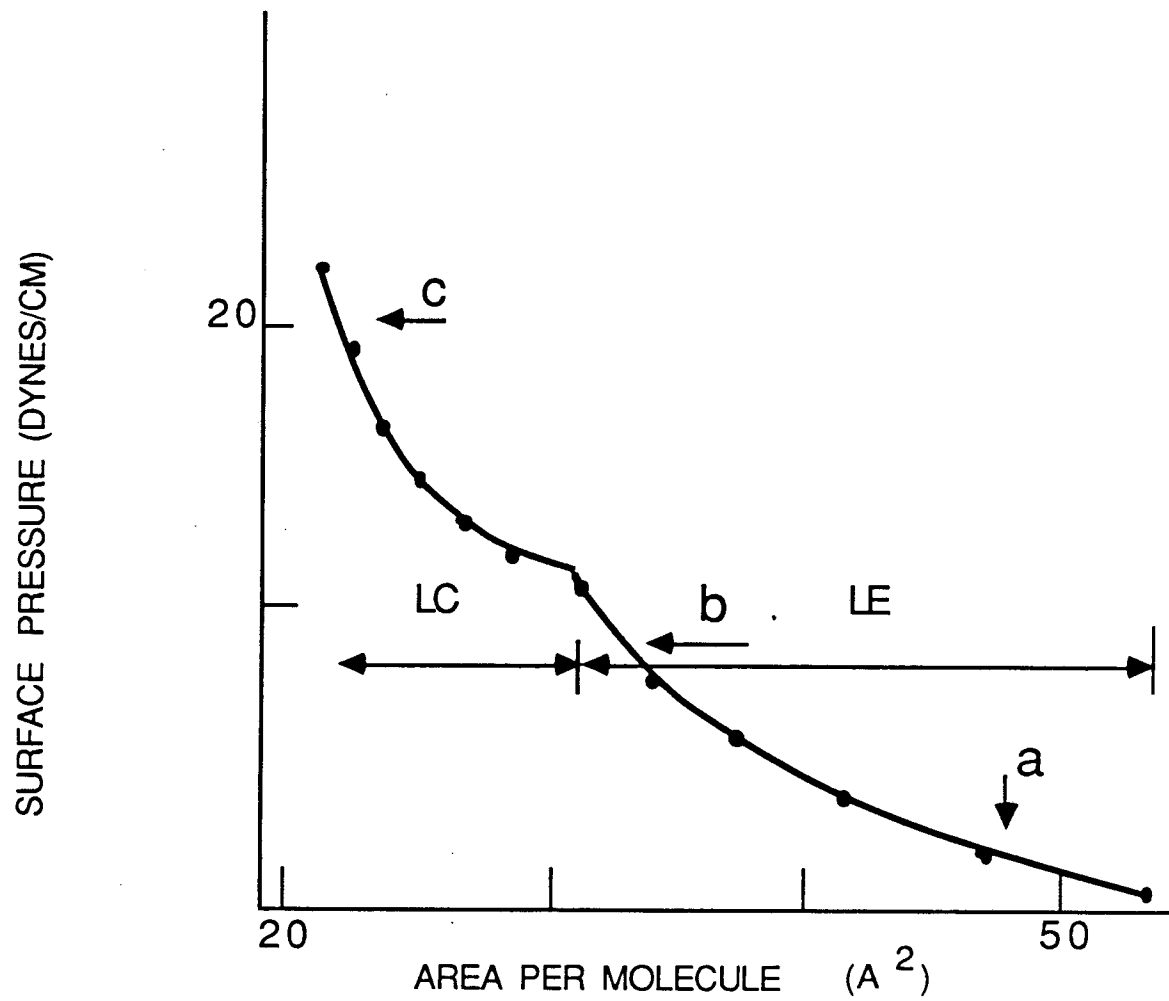


Figure 1

XBL-877-3179

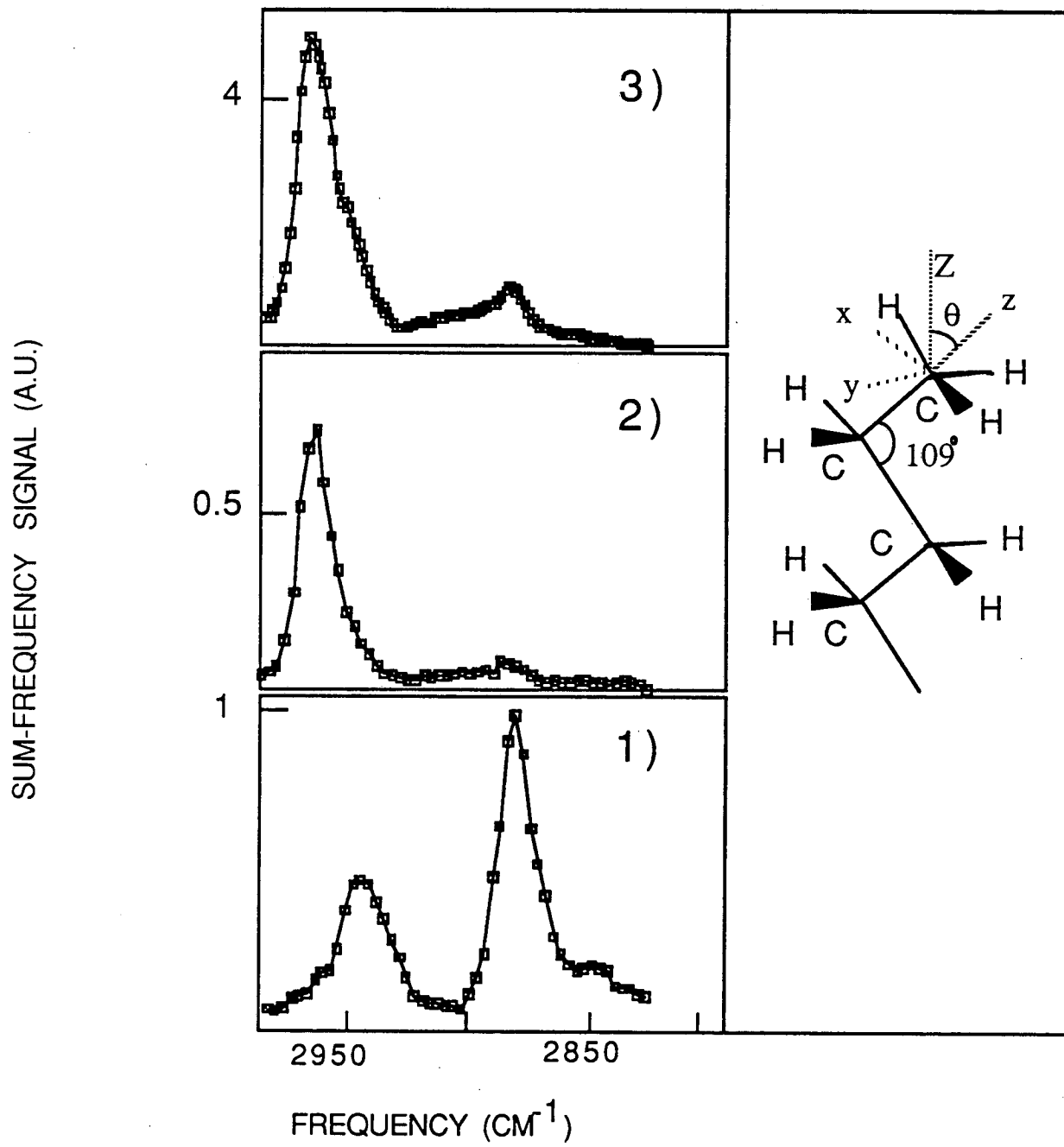


Figure 2

XBL-877-3071

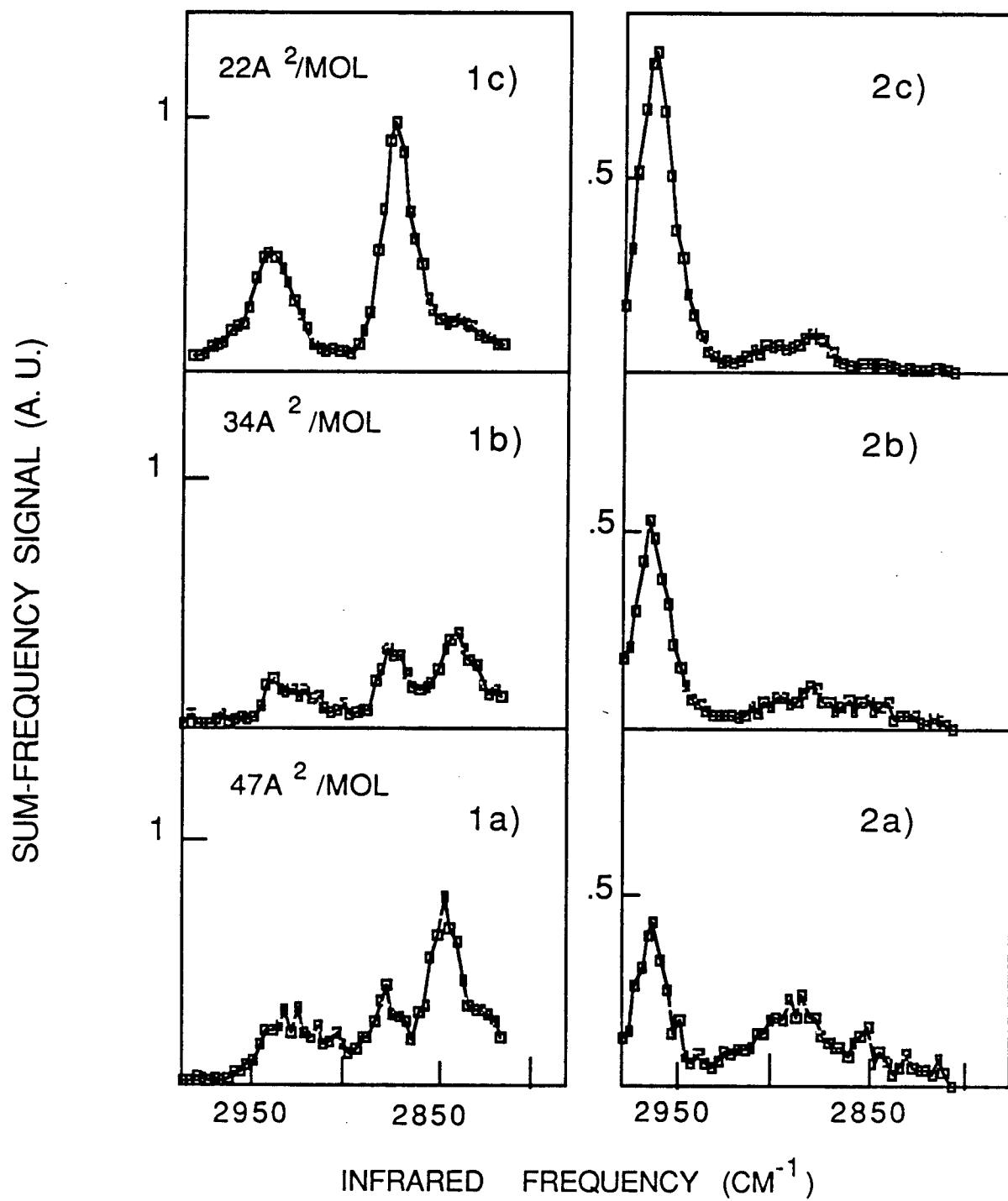
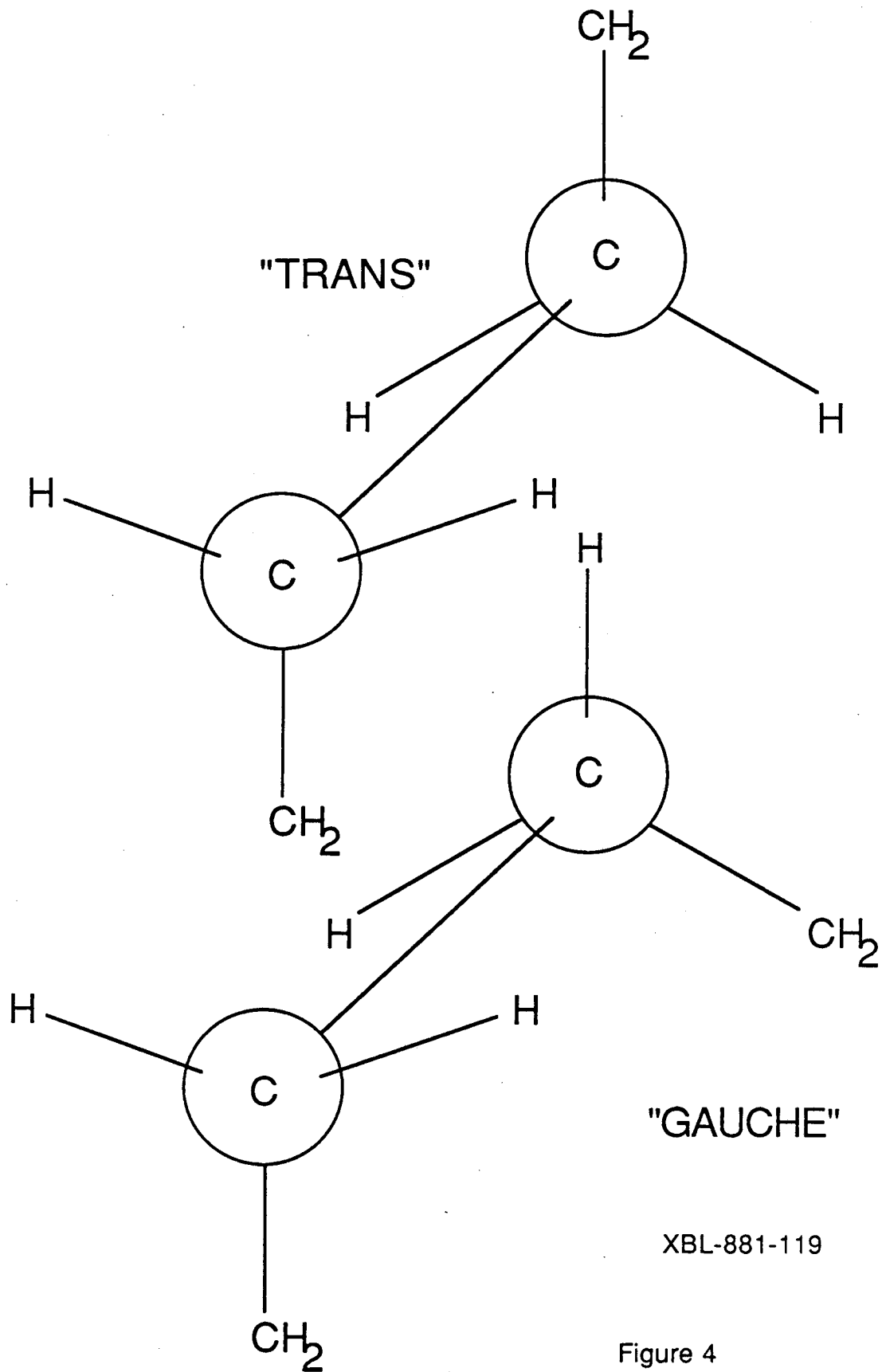


Figure 3

XBL-877-3072



XBL-881-119

Figure 4

## V. Difference Frequency Generation and Up - Conversion

### A. Introduction

The previous chapters have demonstrated sum-frequency generation to be a useful technique for performing IR surface sensitive spectroscopy. However, the technique requires tunable IR pulses of high peak intensity. Production of IR via optical parametric amplification works well in the near infra-red, but is limited by the LiNbO<sub>3</sub> transparency region to wavelengths of approximately 4.5  $\mu\text{m}$ .<sup>1</sup> In this region there are very few accessible vibrational excitations. In fact, the only types of vibrations whose resonant frequencies are above 2200 $\text{cm}^{-1}$  are X-H stretches, where X can be carbon, oxygen, sulfur, etc.<sup>2</sup>

Obviously, one would like to extend this technique to longer wavelengths. Recent advancements in the growth of new high quality nonlinear optical crystals show excellent promise for extending parametric generation in the IR. In particular, AgGaSe<sub>2</sub> and AgGaS<sub>2</sub> have been used to parametrically generate IR radiation to wavelengths of 12 $\mu\text{m}$  and 18 $\mu\text{m}$  respectively.<sup>3,4</sup> However, these crystals are only recently becoming available in the large sizes (centimeter dimensions) needed for high conversion efficiency.

This limitation can be remedied by using Difference Frequency Generation (DFG) from the surface. In this case, the two inputs are both at frequencies greater than the vibrational resonances to be studied, but their difference in frequency is tuned to match the IR vibrational resonance in question. When the frequency difference matches a resonance in the molecule being studied, there is a resonant enhancement in the second order susceptibility, in a manner completely analogous to the SFG case. Consequently, the level of DFG radiation, now at IR wavelengths, will be increased when the frequency difference is tuned through the various IR resonances of the material. Since high-power tunable dye lasers can be continuously tuned throughout the visible, this technique can study any vibrational resonance, the only experimental limitation being imposed by the laser

bandwidth.

Unfortunately, the DFG signal levels will be comparable to those produced by SFG. By comparing surface SFG to DFG, it is shown here that the latter should have outputs of  $10^2$  to  $10^4$  IR photons per laser shot. The expression for the signal strength of DFG is<sup>5</sup>

$$S(\text{DFG}) = 128\pi^3 (\omega_{\text{DF}}/hc^3)^2 |L_{\text{DF}}^m L_1^n L_2|^2 |\chi^{(2)}_{\text{Imn}}|^2 (U_1 U_2 / AT), \quad (1)$$

Here, the L are geometric Fresnel factors relating the surface fields to the radiating fields in air,  $U_1$  and  $U_2$  are the energies of the two inputs, A is the pulse overlapping area on the surface, T is the pulse duration, and S is in photons per pulse. The geometric Fresnel factors are the same as those listed in chapter III equation (9).

Suppose one wishes to scale the SFG signal as given in chapter III equation (9) to the DFG signal as given above in equation (1). The ratio of the signals will be

$$S(\text{DFG})/S(\text{SFG}) = (\omega_{\text{DF}}/\omega_{\text{SF}}) (U_1 U_2 / U_{\text{IR}}). \quad (2)$$

Suppose the laser system that is described in chapter II is modified, so that instead of generating inputs at  $.532\mu\text{m}$  and  $3.3\mu\text{m}$ , it is used to generate inputs at  $1.064\mu\text{m}$  and  $1.6\mu\text{m}$ . This can be done simply in the following manner. First, removal of the SHG KD\*P crystal will leave the fundamental  $1.064\mu\text{m}$  unchanged. Second, instead of filtering out the  $1.6\mu\text{m}$  output from the OPA, one should filter out the  $3.3\mu\text{m}$  and use the  $1.6\mu\text{m}$  on the sample. In equation (2),  $U_1$  is the energy of the  $1.064\mu\text{m}$  input and  $U_2$  is the energy of the  $.532\mu\text{m}$ . Chapter II equation(19) shows that

$$U(1.064\mu\text{m})/U(.532\mu\text{m}) = 4. \quad (3)$$

Furthermore, chapter II equation(12) shows that the ratio of the energies of the signal

(1.6 $\mu\text{m}$ ) and idler (3.3 $\mu\text{m}$ ) OPA outputs is given by

$$U_s/U_i = \omega_s/\omega_i = 2, \quad (4)$$

where  $\omega_s$  and  $\omega_i$  are the frequencies of the signal and idler respectively. In equation (2)  $U_2 = U_s$  and  $U_{\text{IR}} = U_i$ , so  $U_2/U_{\text{IR}} = 2$ . Using the fact that  $\omega_{\text{DF}}/\omega_{\text{SF}} = 3000\text{cm}^{-1}/21979\text{cm}^{-1} = 1/7.3$ , it is found that  $S(\text{DFG})/S(\text{SFG}) = 1.1$ . So, the signal strengths (photons per pulse) that were observed in SFG will be approximately equal to the signal strengths expected for DFG. This means that detection with photomultiplier tube signal to noise characteristics will be necessary. However, PMT sensitivities very quickly fall off at wavelengths longer than one-micron.<sup>6</sup> Since even the shortest wavelength fundamental vibrational resonances occur in the vicinity of two micron, a different detection scheme must be employed.

An obvious choice of detection scheme is the use of up-conversion of the IR to visible wavelengths via some nonlinear crystal. This process was first analyzed in detail by Kleinman and Boyd,<sup>7</sup> with more complete reviews by Voronin and Strizkevskis and Warner.<sup>8,9</sup> Recent work by Hartmann and Laubereau reported an up-conversion efficiency of 5% and noise level corresponding to  $10^4$  IR photons per pulse.<sup>10</sup> Conversion efficiencies up to unity have been reported (although with large background noise) and others have reported low noise equivalent photon levels limited by the photomultiplier dark counts.<sup>8</sup>

For the specific application of detection of DFG, the signal to background discrimination must be sufficient to resolve the one to  $10^3$  DFG photons produced per laser shot. Obviously, one would like to have as high a conversion efficiency in the nonlinear crystal as possible. However, it must be kept in mind that higher conversion efficiency is only desirable if the process does not lead to higher noise.

In the up-conversion technique, an IR source is mixed with a visible beam to produce an output at the sum-frequency. In the up-conversion limit, (no input at  $\omega_{\text{UC}} = \omega_{\text{IR}} + \omega_{\text{P}}$  and  $I_{\text{P}} \gg I_{\text{IR}}$ ) the up-conversion efficiency is given by<sup>9</sup>

$$\eta = \sin^2\{[(32\pi^3\omega_{UC}\omega_{IR}[\chi^{(2)}_{eff}]^2I_P)/(c^3n_Pn_{IR}n_{UC})]^{1/2}\}, \quad (5)$$

where  $\eta$  is defined as the ratio of the number of up-converted photons (photons at  $\omega_{UC} = \omega_P + \omega_{IR}$ ) to the number of input IR photons. This relation assumes that there is no input at the sum-frequency and the pump intensity is much larger than the IR intensity. Note that the efficiency is dependent only on the pump intensity and is independent of the IR intensity. Hartmann and Laubereau demonstrated this fact over 10 orders of magnitude of IR input.<sup>10</sup>

However, the relatively low (5%) conversion efficiency and large noise ( $10^3$  photons per shot) reported in this same article by Hartmann and Laubereau would not be sufficient for the detection of 1 to  $10^3$  photons produced in surface DFG. Specifically, H&L's total detection efficiency

$$\eta_{total} = (\eta_{UC}) (T) (\eta_{PMT}) \quad (6)$$

where  $\eta_{UC}$  is the up-conversion efficiency,  $T$  is the transmission of the optics, and  $\eta_{PMT}$  is the PMT quantum efficiency, was restricted to a value of  $2 \times 10^{-5}$ .<sup>9</sup> This was due to the relatively low up-conversion efficiency of 5% and low photomultiplier conversion efficiency of  $10^{-3}$ .

Since Hartmann and Laubereau were using  $\text{LiNbO}_3$  as the up-conversion crystal, they had to use a pump wavelength of  $1.064 \mu\text{m}$  because  $\text{LiNbO}_3$  forms color centers when exposed to high intensity radiation at  $.532 \mu\text{m}$ . Consequently, the up-converted signal was produced at  $.804 \mu\text{m}$  where the PMT in question had a relatively poor quantum efficiency. It is not stated why a higher intensity pump source was not used to improve the up-conversion efficiency, but their efficiency was already sufficient for the subsequent experiment they were to perform.<sup>11</sup>

In order to get the largest possible total efficiency, it is necessary to get a large



up-conversion efficiency in the nonlinear crystal and a larger PMT quantum efficiency. The latter can be accomplished by using a pump wavelength in the visible (.532  $\mu\text{m}$ ) so that the up-converted signal will be at a wavelength where the PMT will have a detection efficiency closer to .15. Therefore the chosen crystal should be transparent from the near IR to .4  $\mu\text{m}$ .

$\text{LiIO}_3$  has the desired properties.<sup>12</sup> It's transparency range extends from .3 $\mu\text{m}$  to 4 $\mu\text{m}$ . It's nonlinearity is such that, with proper phase-matching and pump intensity, high conversion efficiency is possible. The phase matching angle as a function of input IR frequency is given in figure 1 for two possible input angles ( $0^\circ$  and  $7^\circ$ ) between IR and pump beams. The condition for phase matching is

$$k_{\text{UC}}^2 = k_{\text{P}}^2 + k_{\text{IR}}^2 = 2 k_{\text{P}} k_{\text{IR}} \cos(\alpha), \quad (7)$$

where  $\alpha$  is the cross angle inside the crystal (as shown in figure 1) and  $k_{\text{UC}}$ ,  $k_{\text{P}}$ , and  $k_{\text{IR}}$  are given by  $(1/c)(n_{\text{UC}}\omega_{\text{UC}})$ ,  $(1/c)(n_{\text{P}}\omega_{\text{P}})$ , and  $(1/c)(n_{\text{IR}}\omega_{\text{IR}})$  respectively. For type-I phase matching,  $n_{\text{P}}$  and  $n_{\text{IR}}$  are ordinary indices of refraction and  $n_{\text{UC}}$  is an extraordinary index of refraction. The Sellmeier equations for  $\text{LiIO}_3$  are<sup>13</sup>

$$n_o^2 = 2.03132 + \{1.37623/[1 - (.0350832/\lambda^2)]\} + \{1.06745/[1 - (169/\lambda^2)]\} \quad (8a)$$

and

$$n_e^2 = 1.83086 + \{1.08807/[1 - .0313810/\lambda^2]\} + \{0.554582/[1 - (158.76/\lambda^2)]\}, \quad (8b)$$

where  $\lambda$  is in  $\mu\text{m}$ .

Since  $\text{LiIO}_3$  is a class 6 crystal,  $\chi_{\text{eff}}$  is given by

$$\chi_{\text{eff}} = \chi_{31} \sin\theta_{\text{PM}}, \quad (9)$$

where  $\theta_{PM}$  is the phase-matching angle for the up-conversion process at the IR wavelength in question. Using Miller's relation to scale the reported value of  $\chi_{31} = 3.4 \times 10^{-8}$  esu to the wavelengths in question gives  $\chi_{31} = 2.8 \times 10^{-8}$  esu.<sup>14</sup> A quick calculation using equation (2) shows that pump intensities on the order of  $1.5 \text{ GW/cm}^2$  should give  $\eta = 1$ .

In choosing the particular optical geometry in question, there were two things to bare in mind. First, the detection of a single IR photon requires a very low background count. This necessitates the use of a crossed beam geometry so that the pump beam can be spatially blocked after traversing the up-conversion crystal. Second, since the beams are crossed in the crystal, the pump beam diameter should be made large enough so that the IR beam experiences the same pump beam intensity across the entire length of crystal. Otherwise, the IR input will experience a high intensity pump only during a very short length of the crystal.<sup>9</sup> Specifically, the IR will be focussed to a 300 micron spot, while the green beam is focussed only slightly to a 1.2 millimeter diameter. The beams propagate at approximately  $7^\circ$  degrees with respect to each other inside the crystal. At this angle, the IR spot experiences a pump beam of  $\sim .5 \text{ GW/cm}^2$  across the entire 2 millimeter of crystal length.

## B. Experimental Set-up

The experimental set-up is shown in figure 2. The output of the OPA is passed through a Ge filter to remove the  $1.5 \mu\text{m}$  output of the OPA and any visible light coincident with the OPA output path. The  $3.3 \mu\text{m}$  OPA output (the OPA output was tuned to the methane line at  $3020 \text{ cm}^{-1}$  as a convenient yet representative IR frequency) is then focussed by a 8 centimeter focal length BaFl lens to the  $\text{LiIO}_3$  crystal. The  $.532 \mu\text{m}$  input is adjusted to overlap the IR input in the  $\text{LiIO}_3$  crystal. The cross angle (the angle between the propagation directions of the IR and pump input beams) outside the crystal is  $14^\circ$ . Using the indices of refraction for the  $3.3 \mu\text{m}$  and  $.532 \mu\text{m}$  inputs (which can be found from equation 8a in this chapter) and Snell's law, one finds that the cross angle inside the crystal is  $7^\circ$ . Since

most of the infrared was not up-converted, a photodiode was placed in the path of the transmitted infrared to provide a reference of the infrared signal input level. An energy meter was used to calibrate the signal from the photodiode. No photodiode was used to monitor the green signal since its fluctuations were quite small (<5%) and could be averaged out over a large number of laser pulses.

At full IR input power (100 $\mu$ J), the resulting SFG signal could easily be seen by eye when properly phase-matched. The SFG signal level was measured by attenuating the SF beam with several orders of magnitude worth of Kodak Wrattan gelatin neutral density filters to appropriate levels before passing it through the interference filter (IF), monochromator (MC), and photomultiplier (PMT) combination. Independent accurate determination of the transmission of each optical element was obtained on a Beckman spectrometer. One must be careful to account for all reflection losses in the beam propagation path. The photomultiplier quantum efficiency was determined by attenuating an energy-meter-measurable amount of up-converted light down to the level of tens of photons. It was found that the PMT in question had a 10% quantum efficiency. This allowed one to determine the signal strength at the exit from the LiIO<sub>3</sub> crystal.

The damage threshold was measured to be between 3.3 GW/cm<sup>2</sup> and 5.4 GW/cm<sup>2</sup>. However, the damage at these figures occurred very quickly (within a few tens of laser shots). It was not known if intensity values below, but near, these values would still cause damage over longer exposure times. Consequently, to be completely safe, pumping powers were limited to approximately 1 GW/cm<sup>2</sup>, so that the LiIO<sub>3</sub> crystal would not damage.

### C. Results

The theoretical efficiency and the experimental results are shown in figure 3. There are two theoretical curves. The upper curve is the theoretical efficiency which ignores the effect of saturation at high pump intensities. (Quantitatively, it assumes that in equation (2),  $\sin^2[(X)^{1/2}] = X$ .) The lower curve is the theoretical curve which includes the saturation

effect. Both curves include a reduction in the effective interaction length due to the walkoff effect described in the next paragraph.

The walkoff angle as defined in chapter II equation (15) gives a  $4^\circ$  walkoff angle for the up-converted beam in  $\text{LiIO}_3$ . (Recall that the walkoff angle is the angle between the normal to the phase front ( $\mathbf{k}$  - vector) and the direction of energy flow. Since only the up-converted beam is an e-ray, it is the only beam which experiences a walk-off.) The input beams are crossed in the crystal at an angle of  $7^\circ$ . The up-converted beam propagates at approximately  $0.5^\circ$  with respect to the visible pump beam. So, the up-converted beam  $\mathbf{k}$ -vector is at  $6.5^\circ$  with respect to the IR propagation direction. Since the up-converted energy flow is at a  $4^\circ$  angle with respect to the  $\mathbf{k}$ -vector, the up-converted beam energy flow is at a  $10.5^\circ$  angle with respect to the IR beam. This angle causes the up-converted beam walkoff from the IR beam prematurely and reduces the effective interaction length to 1.6 millimeter. (The IR spot is  $\sim 300$  microns in diameter, so the up-converted beam will be approximately the same diameter. With a  $10.5^\circ$  difference in propagation direction, the IR and up-converted beams will be separated by one diameter after traveling 1.6 millimeters in the crystal.) It is this quantity that must be used in the calculation of the conversion efficiency. This causes a small reduction in the efficiency compared to that predicted if one does not consider the walkoff effect. (The interaction length enters the argument of the efficiency,  $\eta$ , in equation (5) as  $l^2$ . Consequently, there is a reduction in that argument by  $(2/1.6)^2 = 1.6$ .) The largest efficiency measured was 27%. Taking the walkoff effect into account, with  $165\mu\text{J}$  pump energy in a 15 ps 1.2 millimeter diameter pulse ( $.97\text{GW}/\text{cm}^2$ ), the predicted efficiency is 29%, in good agreement with the measured quantity. The phase matching angle was also checked. At the wavelength in question, the predicted (see figure 1) and measured angles were  $26^\circ$  and  $25.6^\circ$  respectively.

In absence of IR input (blocked IR input), the noise level was measured to be .1 up-converted photon per pulse. Using the measured 27% conversion efficiency factor, the up-conversion detector as a whole had a noise equivalent of .4 IR photon per pulse.

At this point, the low IR signal response needed to be checked. It was found that Kodak Wrattan gelatin filters had a very small, though finite transmission in the IR. The transmission was determined by inserting two filters into the IR path and measuring the reduction in the sum-frequency signal caused by each filter. The IR signal before the filters was approximately  $1.2 \times 10^{11}$  photons per pulse. Each Wrattan filter reduced the signal by a factor of approximately  $4 \times 10^4$ . The two filters together reduced the signal by approximately  $1.5 \times 10^9$ , consistent with the single filter measurement. The up-converted signal strength was  $\sim 22$  photons per shot. Using the measured 27% conversion efficiency factor, the attenuated IR signal was approximately 80 IR photons per shot. Since the noise equivalent was found to be .4 IR photon per shot, the signal to noise ratio this IR input level was 200:1.

It should be noted that the phase-matching bandwidth is approximately  $30 \text{ cm}^{-1}$ .<sup>10</sup> This is small compared to the usual desired tuning range ( $200 \text{ cm}^{-1}$ ). Therefore, the crystal angle must be stepped with the IR input wavelength.

Consequently, this detection scheme, with a combination of up-conversion crystal, IF, MC, and PMT has a high enough signal to noise ratio to be able to detect the IR photon levels generated in the surface DFG measurements.

#### D. Other crystals

##### 1. AgGaS<sub>2</sub>

A primary disadvantage to LiIO<sub>3</sub> is its limited transparency range in the IR. LiIO<sub>3</sub> is transparent only to approximately  $5.5 \mu\text{m}$ . Although  $5.5 \mu\text{m}$  is a longer wavelength than is accessible by optical parametric amplification in LiNbO<sub>3</sub>, one would like to use DFG to examine spectroscopic features at longer IR wavelengths. To do this, one requires a nonlinear crystal whose transparency region extends further into the IR.

AgGaS<sub>2</sub> is an excellent choice for this purpose. Its transparency region extends from  $.53 \mu\text{m}$  to  $12 \mu\text{m}$ .<sup>15</sup> It also has good nonlinear coefficients and high surface damage thresholds. To be more quantitative,  $d_{36}$  is reported as  $d_{36} = 4.3 \times 10^{-8}$  esu for type-I

phase-matched SHG of 10.6  $\mu\text{m}$  laser radiation.<sup>15</sup> Elsaesser et. al. reported damage threshold in excess of 25  $\text{GW}/\text{cm}^2$  when pumping with 1.064 $\mu\text{m}$  pulses of 30 ps duration.<sup>4</sup>

In order to use this crystal for up-conversion, one needs both a phase-matching curve and an estimate of the quantum up-conversion efficiency. To generate the phase-matching curve, one follows the same procedure as that used for  $\text{LiIO}_3$ . The Sellmeier equations for  $\text{AgGaS}_2$  are<sup>15</sup>

$$n_o^2 = 3.3970 + \{2.3982/[1 - (0.09311/\lambda^2)]\} + \{2.1640/[1 - (950/\lambda^2)]\} \quad (10a)$$

and

$$n_e^2 = 3.5873 + \{1.9533/[1 - (.11066/\lambda^2)]\} + \{2.3391/[1 - (1030.7/\lambda^2)]\}, \quad (10b)$$

where  $\lambda$  is in  $\mu\text{m}$ .

For type-I phase-matching, the indices of refraction must behave according to

$$n_{UC} = n_P \omega_P + n_{IR} \omega_{IR}, \quad (11)$$

assuming a collinear phase-matching geometry. (Since this section does not contain any experimental results, only the collinear case is calculated, although it is a simple computer computation task to use equation (7) to calculate phase-matching angles for the noncollinear case.)

Due to the fact that  $\text{AgGaS}_2$  is not transparent at wavelengths shorter than .53 $\mu\text{m}$ , this calculation will be done using a pump wavelength of 1.064 $\mu\text{m}$ . (One could, in principle, use a pump wavelength between 1.064 $\mu\text{m}$  and .532 $\mu\text{m}$ . However, since the system described in chapter II starts with a Nd:YAG oscillator, the calculation will assume a pump wavelength equal to the oscillator's output.)

Using type-I phase matching, a theoretical tuning curve has been generated assuming a 1.064 $\mu\text{m}$  pump beam. The tuning curve shown in figure 4 covers the range for

IR inputs from 10 $\mu\text{m}$  to 2.5  $\mu\text{m}$ .

The effective nonlinear susceptibility for this type of phase matching is given by

$$\chi_{\text{eff}}^{(2)} = -2 d_{36} [\sin\theta] [\sin(2\phi)]. \quad (12)$$

Using equations (2) and (12) above, the up-conversion efficiency can be calculated. Here,  $\lambda_{\text{IR}} = 6\mu\text{m}$ , is used as a representative case. Using Miller's relation,  $d_{36}$  can be scaled to the up-conversion case. It is found that  $d_{36} = 5.6 \times 10^{-8} \text{esu}$ . Using figure 4, the value for  $\theta$  for phase-matched conversion is seen to be  $\theta = 29.3^\circ$ . This gives  $\chi_{\text{eff}}^{(2)} = 5.5 \times 10^{-8} \text{esu}$ . Using equation (2), it is found that  $I_{\text{P}} = 58 \text{MW/cm}^2$  gives  $\eta = 10\%$ ,  $I_{\text{P}} = .36 \text{GW/cm}^2$  gives  $\eta = 50\%$  and  $I_{\text{P}} = 1.43 \text{GW/cm}^2$  gives  $\eta = 1.00$ , where it has been assumed that  $l = 2 \text{mm}$ . Assuming a pump pulse of 30ps duration and 1mm diameter,  $I_{\text{P}} = 58 \text{MW/cm}^2$  corresponds to 13.6 $\mu\text{J}$ ,  $I_{\text{P}} = .36 \text{GW/cm}^2$  corresponds to 85 $\mu\text{J}$ , and  $I_{\text{P}} = 1.43 \text{GW/cm}^2$  corresponds to 337 $\mu\text{J}$ . Given the ease with which these energies can be generated, it is seen that  $\text{AgGaS}_2$  has excellent potential for use in the detection of IR radiation via up-conversion. (The low intensities needed here are due to the relatively high  $\chi_{\text{eff}}^{(2)}$  value.) One should note, however, that the photo-multiplier quantum detection efficiency will typically be an order of magnitude lower at  $\lambda_{\text{UC}} = .904\mu\text{m}$  than at  $\lambda_{\text{UC}} = .458\mu\text{m}$ . Consequently, the overall detection efficiency (equation (6)) of the up-conversion detector will not be appreciably different from that described for  $\text{LiIO}_3$ .

## 2. KTP

Another nonlinear crystal which has been getting considerable attention is KTP ( $\text{K-TiO-PO}_4$ ).<sup>17</sup> The crystal, which has nonlinearities comparable to  $\text{LiIO}_3$  has the following additional benefits: 1) it is a non-hydroscopic crystal, which makes it much easier to work with in a laboratory environment and 2) it has a very high damage threshold.

A study was undertaken to assess the up-conversion possibilities for KTP. Index of

refraction data in the infra-red is sketchy at best since most applications of the crystal seem to be for standard 1.064 $\mu\text{m}$  second harmonic generation. Using index of refraction data obtained from a private source,<sup>18</sup> the following Sellmeier equations for KTP were computed.

$$n_x^2 = 2.23052385 + \{0.779446937/[1 - (.0477009547/\lambda^2)]\} + \{1.27293994/[1 - (97.657141/\lambda^2)]\}, \quad (9a)$$

$$n_y^2 = 2.32400693 + \{.709006232/[1 - (.0545497704/\lambda^2)]\} + \{1.40060586/[1 - (105.168158/\lambda^2)]\}, \quad (9b)$$

and

$$n_z^2 = 2.36849513 + \{.952359988/[1 - (.058536793/\lambda^2)]\} + \{3.13085741/[1 - (186.168899/\lambda^2)]\}, \quad (9c)$$

where  $\lambda$  is in  $\mu\text{m}$ . It must be understood that the data to which this equation is fit only extends to 2.5  $\mu\text{m}$ , and is sparse even in that region. The IR wavelength region where it is desirable to do infra-red up-conversion is actually closer to 3.3 $\mu\text{m}$ , requiring an extrapolation of the data. Since KTP begins to absorb near 4 $\mu\text{m}$ ,<sup>17</sup> the index of refraction curve should begin to curve downward near those wavelengths. Thus, one would expect the above Sellmeier equations to produce values for the indices of refraction at slightly elevated values.

Phase matching in KTP is considerably different from the cases which have been dealt with up to this point. KTP is a biaxial crystal. This means that one can no longer speak of e-rays and o-rays. All polarizations experience indices of refraction which are a function of the propagation angle with respect to the principle axes in the crystal. The index surface at a given frequency is given by

$$\begin{aligned} & [(\sin\theta)^2 (\cos\phi)^2] / [n^2 - n_x^{-2}] + (\sin\theta)^2 (\sin\phi)^2 / [n^2 - n_y^{-2}] + \\ & + (\cos\theta^2) / [n^2 - n_z^{-2}] = 0, \end{aligned} \quad (10)$$



where  $x$ ,  $y$ , and  $z$  are the KTP crystal axes.  $\theta$  is the angle between the propagation direction and the crystal  $z$ -axis and  $\phi$  is the angle between the projection of the propagation direction on the  $x$ - $y$  plane and the crystal  $x$ -axis. For each wavelength there will be two solutions  $n^+$  and  $n^-$ , where the superscripts refer to the larger or smaller solution to the equation, and the linear polarizations associated with  $n^+$  and  $n^-$  are at  $90^\circ$  with respect to one another. Then, type-I phase-matching can be either of the following: 1)  $(n^+)$ -ray combines with  $(n^+)$ -ray to become  $(n^-)$ -ray or 2)  $(n^-)$ -ray combines with  $(n^-)$ -ray to become  $(n^+)$ -ray. Type-II phase-matching can be either of the following: 1)  $(n^+)$ -ray combines with  $(n^-)$ -ray to become  $(n^+)$ -ray or 2)  $(n^+)$ -ray combines with  $(n^-)$ -ray to become  $(n^-)$ -ray.

Clearly, with this sort of complicated frequency and angular dependence, any phase-matching predictions must be generated numerically. The numerical solution proceeds as follows. For each of the three wavelengths involved,  $n_x$ ,  $n_y$ , and  $n_z$  are found. Then,  $n$  is found for each  $\phi$  and  $\theta$  combination for each wavelength. From this,  $|k| = (n\omega)/c$  can be determined. Then, all the possible  $k$ -combinations are compared to see if any are equal, so that phase-matching is possible.

It was found that using the index of refraction combinations  $IR(n^-) + P(n^+) = SF(n^-)$ , it was possible to type-II phase-match the up-conversion process. (One therefore expects that for that case of an IR input linearly polarized  $90^\circ$  with respect to the pump input, the output will be linearly polarized parallel to the IR input.) A type-II phase-matching curve was generated for the up-conversion of a  $3020 \text{ cm}^{-1}$  IR input. This is shown in figure 5. Note that  $\theta$  is given as a function of  $\phi$ . Because of the biaxial nature of KTP, every choice of  $\phi$  has an associated  $\theta$  that will lead to phase-matched up-conversion.<sup>19</sup>

Ordinarily, the choice of  $\phi$ - $\theta$  combination is determined by the effective susceptibility. In KTP, for type-II phase-matching, the effective susceptibility is given by<sup>20</sup>

$$\chi_{\text{eff}}^{(2)} = 2\{(d_{24} - d_{15})(\sin 2\phi)(\sin 2\theta) - [(d_{15}(\sin \phi)^2 + d_{24}(\cos \phi)^2)(\sin \theta)]\}, \quad (11)$$

(It should be noted that type-I phase-matching is rarely used in KTP; the  $\chi_{\text{eff}}^{(2)}$  is typically a factor a five lower than that for type-II phase-matching, due to the near cancellation of the terms in the effective susceptibility.)<sup>20</sup>

The effective susceptibility is plotted in figure 6 using the phi-theta combinations from figure 5. It can be seen that the maximum  $\chi_{\text{eff}}^{(2)}$  is encountered at  $\phi = 0^\circ$ ,  $\theta = 45^\circ$ .

Suppose one does a term by term comparison in the expression for up-conversion efficiency (equation (2)) between KTP and  $\text{LiIO}_3$ . It is seen that the only term which can be significantly different is  $I_p$ . If one were to use a 2 millimeter KTP crystal which had been cut for an optimum  $\chi_{\text{eff}}^{(2)}$  value of  $5.4 \times 10^{-9}$  esu, then the high damage threshold of KTP ( $>25 \text{ GW/cm}^2$  for a 15 ps pulse<sup>17</sup>) should, in principle, allow one to obtain  $\eta = 1.00$ .

It was decided for this measurement to have the KTP crystal cut at an intermediate  $\phi$  value ( $\phi = 50^\circ$ ) to maximize the chances of phase-matching. Due to this fact,  $\chi_{\text{eff}}$  was reduced by a factor of approximately 2 compared to the optimum value. leading to a reduction in the expected conversion efficiency. Using coefficients published in the literature<sup>17</sup> and using Miller's relation to scale  $\chi$  to the wavelengths in question, it is found that  $\chi_{\text{eff}} = -2.6 \times 10^{-9}$  esu (see figure 6). Equation (2) can be used to calculate the up-conversion efficiency. The values used are  $\omega_{\text{IR}} = 3020 \text{ cm}^{-1}$ ,  $\omega_{\text{SF}} = 21813 \text{ cm}^{-1}$ ,  $l = .08 \text{ cm}^{-1}$ ,  $I_p = 2 \times 10^{16} \text{ esu}$  ( $2 \text{ GW/cm}^2$ ),  $n_{\text{IR}} = 1.6913$ ,  $n_p = 1.8396$ , and  $n_{\text{SF}} = 1.8027$ . Using these values and the aforementioned  $\chi_{\text{eff}}$ , one finds  $\eta = 7\%$ .

Although this theoretical value may seem somewhat low, one must keep in mind that  $\chi_{\text{eff}}$  is not at its optimum value and  $l$  is fairly short (.8 millimeter). Using the optimum  $\chi_{\text{eff}}$  value combined with a 2 millimeter crystal leads to a conversion efficiency  $\eta = 90\%$ , leaving all other parameters unchanged.

The reliability of the phase-matching curve was somewhat in question due to the uncertainties of the index of refraction data. The general form of the index of refraction curve indicated that for any  $\phi$ , a corresponding  $\theta$  existed that would lead to a phase-matched

output. For this reason, an intermediate value of  $\phi$  was selected and two corresponding  $\theta$ 's were chosen to match. Specifically, two KTP crystals were obtained, cut at  $\phi = 50^\circ$ ,  $\theta = 26^\circ$  and  $\phi = 50^\circ$ ,  $\theta = 46^\circ$ . In principle, when checking the phase-matching, one would hold  $\phi$  constant and adjust  $\theta$  plus or minus 10 degrees from the  $\theta$  value at which the crystal was cut. In this way, for a constant  $\phi = 50^\circ$ ,  $\theta$  could be adjusted from  $\theta = 16^\circ$  to  $\theta = 56^\circ$ .

To proceed with the measurement, the green and IR inputs, with their polarizations at  $90^\circ$  with respect to one another, were overlapped on the KTP crystals. Then, in order to assure that the input polarizations were at the proper orientation with respect to the crystal axes, the KTP crystals were rotated about their face-normal until the position of maximum up-conversion efficiency was located. Although rotation about this axis showed a clear maximum for both crystals, the crystal cut at  $\phi = 50^\circ$ ,  $\theta = 26^\circ$  had a maximum conversion efficiency that fell short of the predicted efficiency by between 5 and 6 orders of magnitude, indicating that the up-conversion process was not being properly phase-matched. The crystal cut at  $\phi = 50^\circ$ ,  $\theta = 46^\circ$  had a good conversion efficiency and consequently was used for subsequent quantitative measurements.

The maximum, and consequently phase-matched, up-conversion output was observed at  $\phi = 51^\circ$ ,  $\theta = 47^\circ$  (labeled as + in figure 5 and figure 8) with a crystal orientation as shown in figure 7. The cut KTP piece is basically triangular in shape. The polished crystal faces are in the X-Z plane. The face normal ( $\phi = 50^\circ$ ,  $\theta = 46^\circ$ ) is parallel to the Y-axis, which is also the IR propagation direction. The visible input polarization is parallel to the Z-axis. The IR input polarization is parallel to the X-axis. The bisector of the angle formed by the two indicated crystal edges (as shown in figure 7) contains the crystal's z-axis. The measured conversion efficiency was 3%, in reasonable agreement with theoretical prediction discussed on the previous page. The output polarization was observed to be the same orientation as the IR input, as predicted in the paragraphs immediately preceding equation (11). Additionally, if crystal was tilted about the laboratory Z-axis so that the alignment was moved away from optimum phase-matching, a tilt about the x-axis

would bring the alignment back to a properly phase-matched condition. This indicates that there is more than one  $\phi - \theta$  combination which leads to phase-matched output, consistent with the general phase-matching behavior predicted in figure 5. (This behavior did not exist for the uniaxial crystal  $\text{LiIO}_3$ .) This experimental verification of the existence of the phase-matching  $\theta - \phi$  combinations was intended only to check for the existence of such pairs. Since the changes in angle were not more than 1 degree inside the crystal, including them on figure 5 would not have added additional information on the experimental shape of the  $\theta - \phi$  phase-matching curve. For that reason, no attempt was made to determine the absolute values of these angles from the relative angle changes measured. Numerical calculations indicate that at a constant value of  $\phi$ , a change of 1 degree in the value of  $\theta$  can result in a phase-mismatch of  $30\text{cm}^{-1}$ . For the  $l = .08\text{cm}$  KTP crystal, this gives  $\Delta kl = 2.4$ . For this case of nonzero phase-mismatch there would be a resulting reduction of conversion efficiency by  $\{\sin(\Delta kl/2)/(\Delta kl/2)\}^2 = .6$ . While checking for the existence of these  $\theta - \phi$  combinations, it was noted that changes on the order of 1-2 degrees in the crystal tilt could easily reduce the conversion efficiency by a factor of 2.

The error in the predicted phase-matching angle is most likely due to the index of refraction data. For example, if one lowers the  $n_x$ ,  $n_y$ , and  $n_z$  values at the IR input by 5%, the  $\phi - \theta$  curve in figure 8 is generated, giving a much closer match. (Of course, this is not the only possible way to adjust the index of refraction values to match the theoretical curve to the experimental point. Rather, this figure is included to demonstrate the sensitivity of the phase-matching angle to the indices of refraction.) The index of refraction data was taken on prisms cut from a different boule than the crystal used here. (It has been observed that KTP indices of refraction may vary from boule to boule when grown with the hydrothermal technique.)<sup>21</sup> Also, the crystals used in these experiments are from an "end cap" of a boule. This may have an effect on the optical characteristics of the crystal.

Using the corrected phase-matching curve, one would predict that an ideal crystal should be cut at  $\phi = 0^\circ$ ,  $\theta = 53^\circ$  and be 2 millimeters in length. This would give an

optimum  $\chi^{(2)}_{\text{eff}}$ , since  $\phi = 0^\circ$  for any  $\theta$  in the phase-matching region will give the largest  $\chi^{(2)}_{\text{eff}}$ . With the additional length, conversion efficiencies approaching unity should be possible.

#### E. Conclusion

It has been shown in this section that DFG is a viable alternative to SFG in cases where parametric amplification cannot produce the desired IR radiation. The only difference is that an up-conversion detector is needed to detect the small numbers of IR photons produced in this process. A  $\text{LiIO}_3$  up-conversion device was designed which had a noise-equivalent-level of one photon per laser shot, consequently having a good enough signal-to-noise ratio to resolve the DFG signals. The up-conversion process was also demonstrated in KTP. This crystal can withstand higher pumping powers which can lead to higher conversion efficiencies. Also, being a non-hygroscopic crystal, it is much easier to use in a laboratory environment.

## References

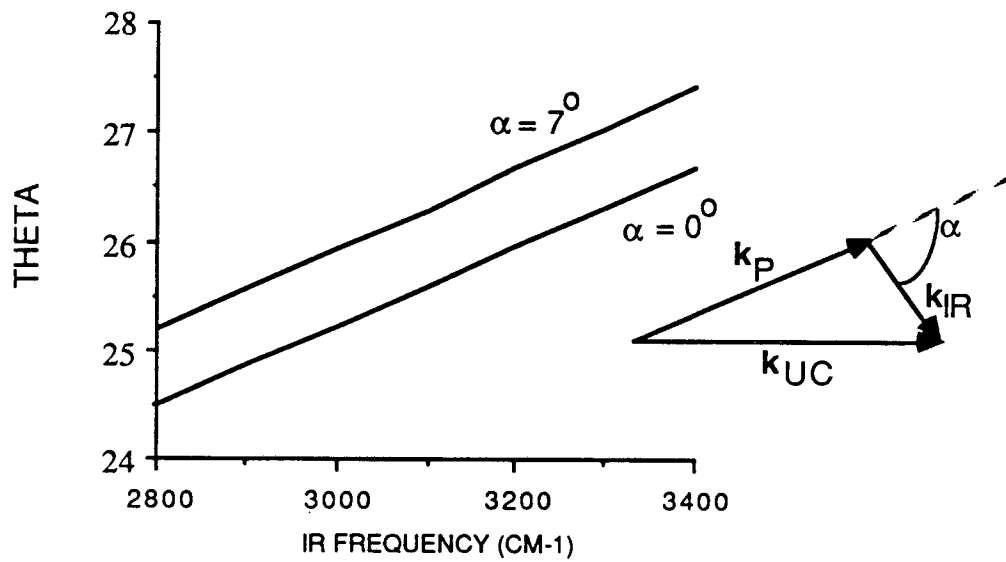
1. A. Seilmeier and W. Kaiser, Appl. Phys. 23, 113 (1980).
2. see, for example, Randall et. al. "Infra-Red Determination of Organic Structures," (Van Nostrand, New York, 1949).
3. R.C. Eckardt, Y.X. Fan, R.L. Byer, C.L. Marquardt, M.E. Storm, and L. Esterowitz, Appl. Phys. Lett. 49, 608 (1986)
4. T. Elsaesser, A. Seilmeier, W. Kaiser, P. Koidl, and G. Brandt, Appl. Phys. Lett. 44, 383 (1984).
5. Y.R. Shen, The Principles of Nonlinear Optics, (John Wiley, New York, 1984).
6. see, for example, Photocathode Spectral Responses in the Photomultiplier Tube catalog published by Hamamatsu.
7. D.A. Kleinman and G.D. Boyd, J. Appl. Phys. 40, 546 (1969).
8. E.S. Voronin and V.L. Strizhevskii, Sov. Phys. Usp. 22, 26 (1979).
9. J. Warner in Quantum Electronics: A Treatise, eds. H. Rabin and C.L. Tang (Academic Press, New York, 1975).
10. H.-J. Hartmann and A. Laubereau, Appl. Optics 20, 4259 (1981).
11. H.-J. Hartmann and A. Laubereau, J. Chem. Phys. 80, (1984).
12. L.S. Goldberg, Appl. Optics 14, 653 (1975).
13. "LiIO<sub>3</sub> Information Sheet" from Cleveland Crystals, Inc., Cleveland, Ohio.
14. M.M. Choy and R.L. Byer, Phys. Rev. B 14, 1693 (1976).
15. Y.X. Fan, R.C. Eckardt, R.L. Byer, R.K. Route, and R.S. Feigelson, Appl. Phys. Lett. 45, (1984).
16. W. Jantz and P. Koidl, Appl. Phys. Lett. 29, 705 (1976).
17. R.F. Belt, G. Gashurov, and Y.S. Liu, Laser Focus 21 (10), 110 (1985).
18. J.D. Bierlein, E.I. du Pont de Nemours and Company, Wilmington, DE, private communication.
19. H. Ito, H. Naito, and H. Inaba, J. Appl. Phys. 46, 3992 (1975).

20. T.Y. Fan, C.E. Huang, B.Q. Hu, R.C. Eckardt, Y.X. Fan, R.L. Byer, and R.S. Feigelson, to be published.
21. J.P. Bly, Litton Airtron, Inc., Morris Plains, NJ, private communication.

## Figure Captions

- Fig. 1  $\text{LiIO}_3$  phase matching curve: These curves show the theoretically predicted phase-matching angle,  $\theta$ , as a function of the infrared input frequency for the up-conversion process.  $\theta$  is the angle between the up-converted signal propagation direction and the optic-axis.  $\alpha$  is the angle between  $k_{\text{IR}}$  and  $k_{\text{P}}$  inside the crystal, as is shown in the figure inset.
- Fig. 2 Experimental set-up
- Fig. 3 Up-conversion efficiency as a function of pump energy. The upper curve is the theoretical efficiency ignoring the effect of saturation at high intensities. The lower curve is the theoretical curve which includes the saturation effect. The crosses are the experimentally measured points.
- Fig. 4  $\text{AgGaS}_2$  phase-matching curve: This curve shows the phase-matching angle  $\theta$  as a function of IR input frequency for the up-conversion process. The predicted angle assumes a collinear pump geometry.
- Fig. 5 KTP phase-matching curve: This curve shows the theoretical combinations of  $\theta$  and  $\phi$  that produce a phase-matched up-conversion of a  $3020\text{cm}^{-1}$  IR input. The experimental point is given by the cross.
- Fig. 6 KTP  $\chi_{\text{eff}}^{(2)}$ : This curve shows  $\chi_{\text{eff}}^{(2)}$  as a function of  $\phi$  for the up-conversion process.
- Fig. 7 Crystal orientation: This figure shows the relationship between the KTP crystal coordinates and the laboratory coordinates.
- Fig. 8 KTP phase-matching curve: This curve recalculates the predicted  $\theta$  and  $\phi$  phase-matching combinations using infra-red  $n_x$ ,  $n_y$ , and  $n_z$  values which are 5% lower than those used in figure 5. The experimental point is given by the cross.

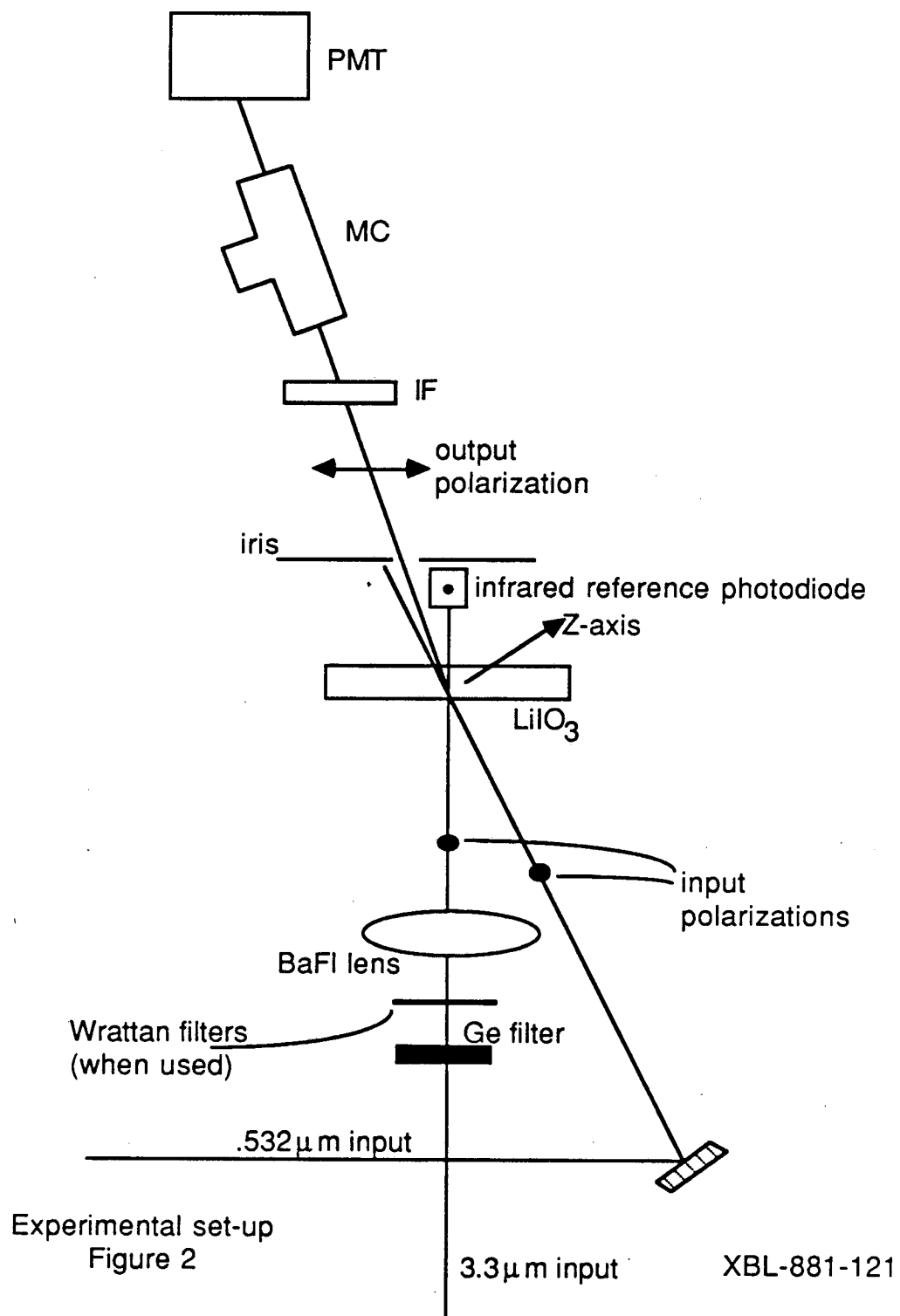


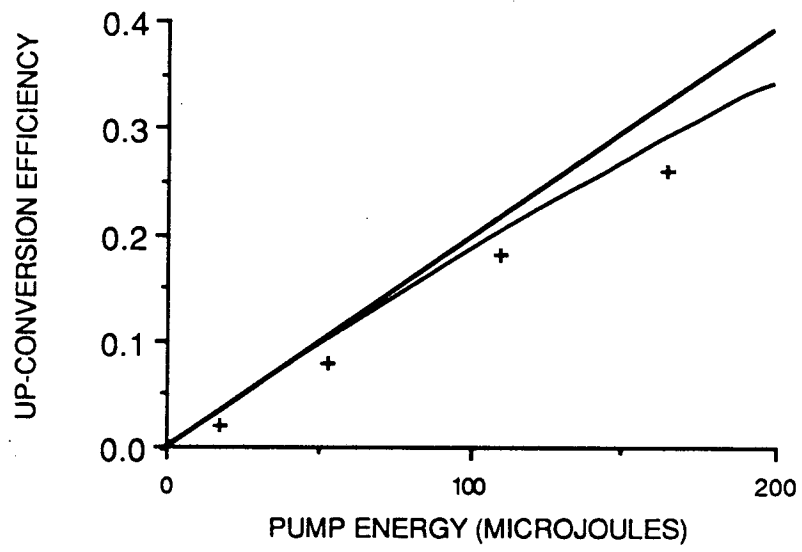


LiIO3 PHASE MATCHING CURVE

Figure 1

XBL-881-120





CONVERSION EFFICIENCY VS. PUMP ENERGY

Figure 3

XBL-881-122

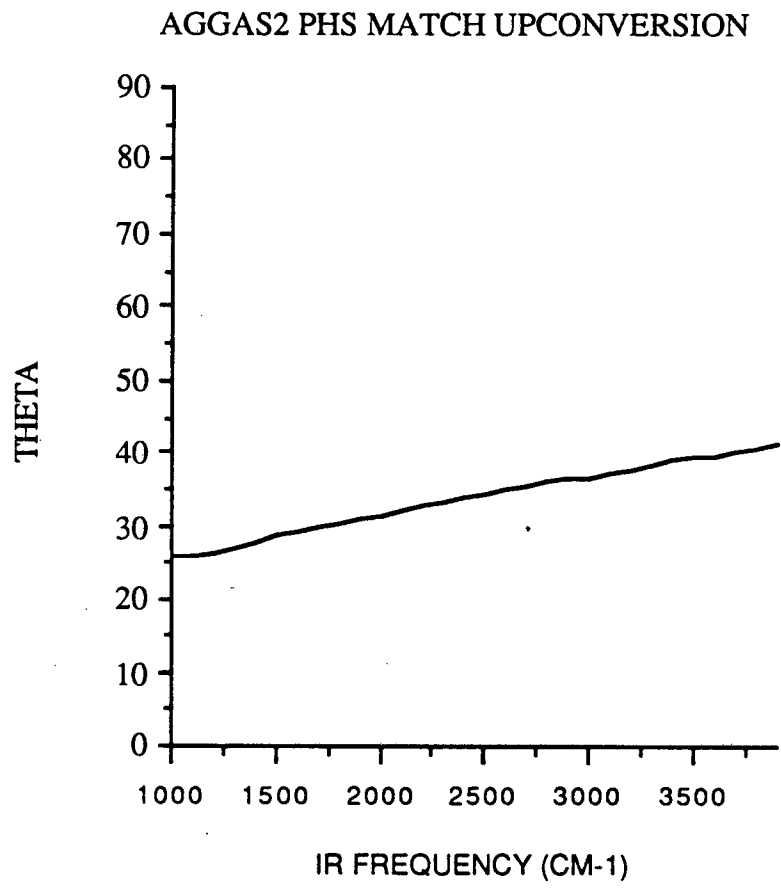


Figure 4

XBL-881-123

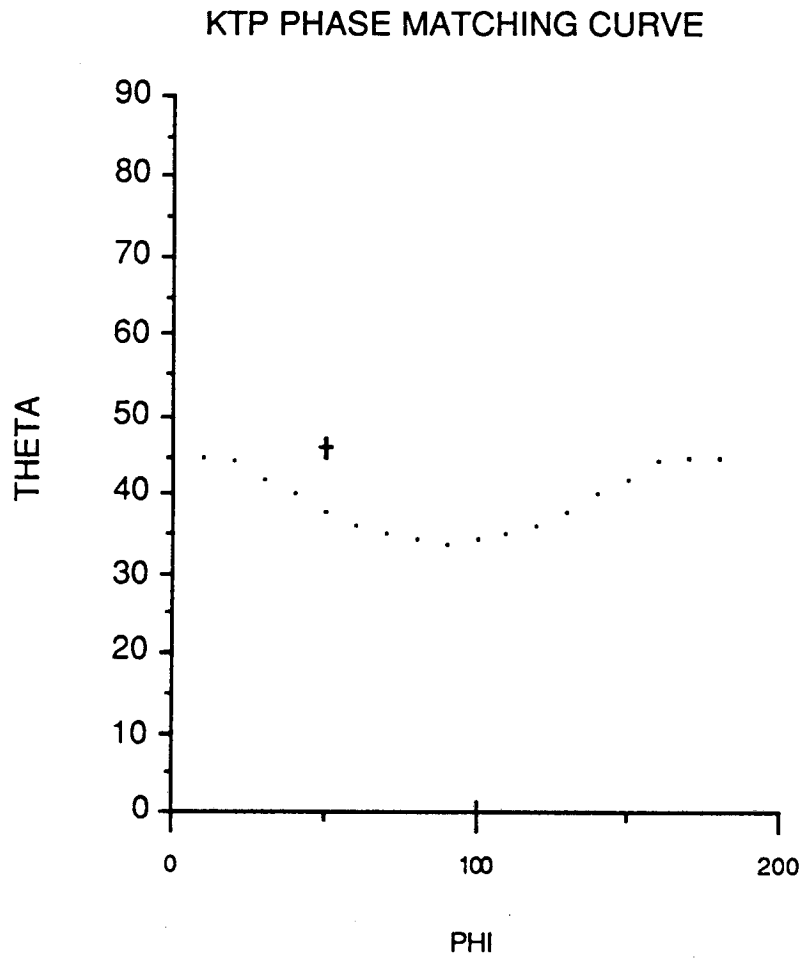
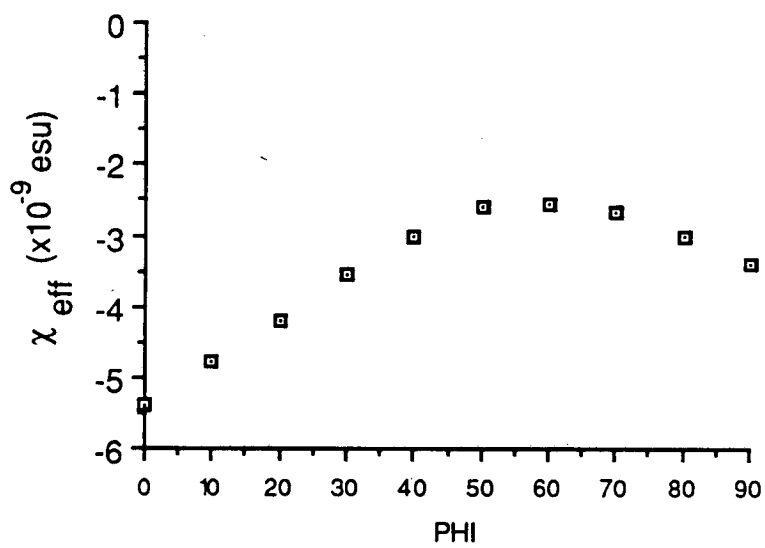


Figure 5

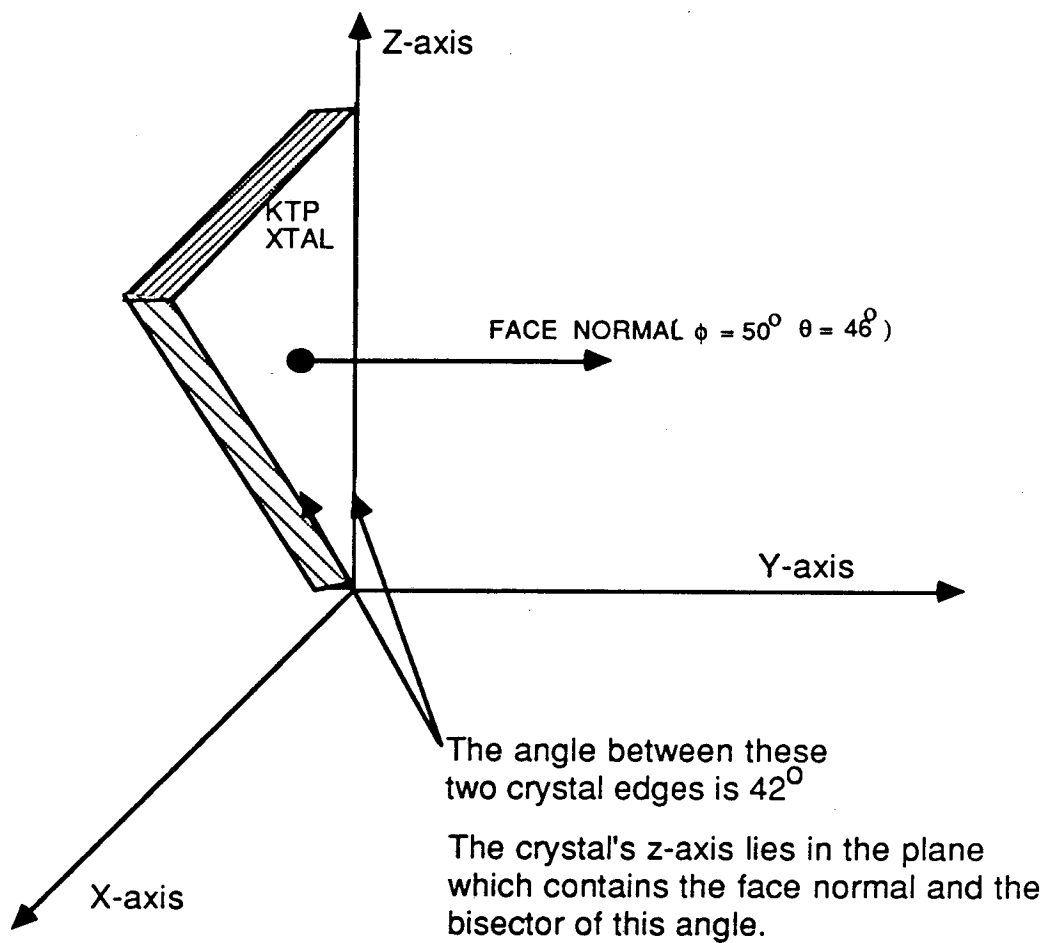
XBL-881-124



EFFECTIVE SUSCEPTIBILITY VS. PHI

Figure 6

XBL-881-125



Crystal Orientation

Figure 7

XBL-881-126

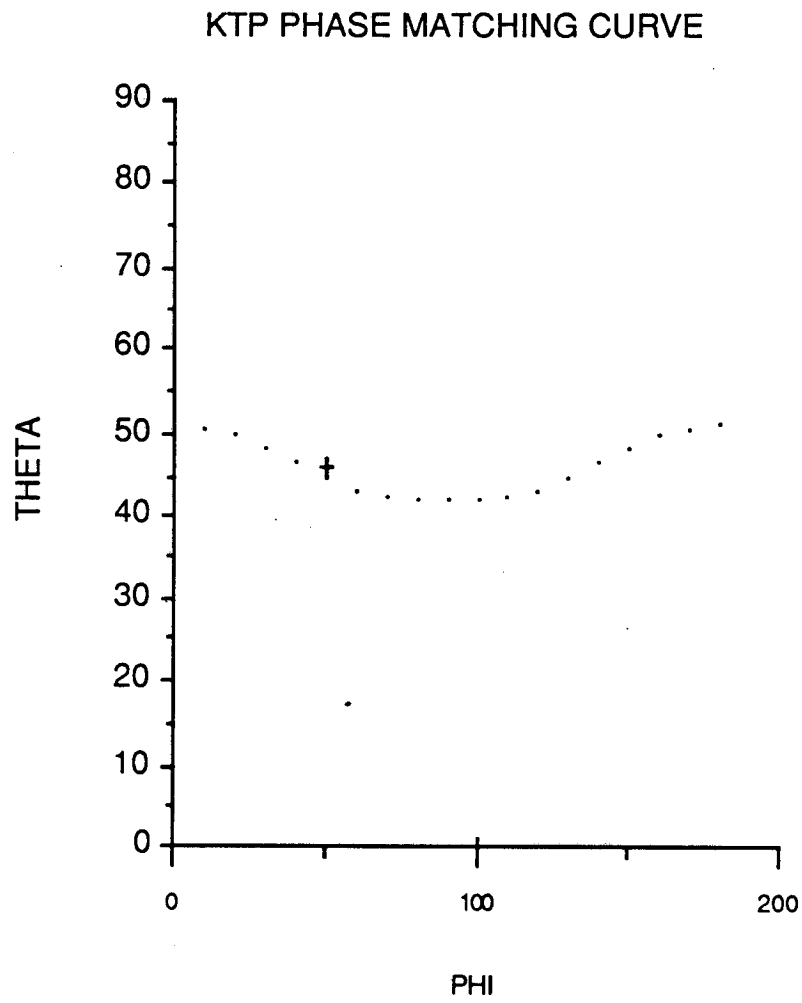


Figure 8

XBL-881-127



## VI. Conclusion

In conclusion, it has been shown that sum-frequency generation is a surface sensitive spectroscopic tool. Surface sum-frequency generation can be used to obtain IR surface spectra without use of elaborate detection schemes or the need for ultra-high vacuum environment necessary for so many other surface tools. The clear spectral response makes it possible to selectively monitor molecular species in chemical reactions. The accessibility of exotic interfaces makes possible in-situ probing of heretofore inaccessible physical interactions at interfaces. There is also the DFG technique for the case where the desired resonances are outside the normal range of parametric IR production.

But the technique has more possibilities. There are other interfaces which can be probed. For example, air/metal, air/semiconductor, and liquid/solid interfaces are also accessible and work is being completed on those interfaces.<sup>1</sup> In particular, SFG is the only technique capable of doing resonant vibrational spectroscopy at the liquid/solid interface.

The short pulse characteristics of the inputs can also be used to perform time-dependent measurements of the molecules at the interface. For example, some kind of pump/probe technique, as is frequently used in picosecond measurements, can be applied to the surface to do  $T_1$  or  $T_2$  measurements. There has been much interest in the surface science community in devising a means to obtain a surface vibrational dephasing time ( $T_2$ ). Due to the fact that molecules adsorbed at different sites on a surface have their vibrational resonances at slightly different positions, the linewidth of a given vibrational resonance will be inhomogeneously broadened.<sup>2</sup> A surface echo technique can then be used to obtain  $T_2$ , as with inhomogeneously broadened resonances in bulk materials. The only difference is that here, two IR pulses are sent to the surface delayed by a time  $T$ , and the re-phasing of the vibrational resonances (which occurs a time  $T$  after the second pulse) can be detected by doing SFG from the re-phased molecules.

Slightly less exotic, though just as important measurements can be done on

molecules measuring their  $T_1$  de-population time. Recent  $T_1$  measurements on certain vibrational resonances in bulk  $\text{CHBr}_3$  suggest that population inversions of 40% are possible with picosecond pulses.<sup>3</sup> This large inversion makes this molecule a likely candidate for surface experiments.

In short, the basic technique has been demonstrated. Given its optical probe capabilities, its ability to do in-situ probing, and its possibilities for time-domain measurements, there are still many potential applications and much new physical information which will be obtained using this technique.

## References

1. P. Guyot-Sionnest, R. Superfine, J.H. Hunt, and Y.R. Shen, submitted to Chem. Phys. Lett.
2. see, for example, G.A. Somorjai, Chemistry in Two Dimensions: Surfaces, (Cornell University Press, Ithaca, New York, 1981).
3. H. Graener, R. Dohlus, and A. Laubereau, Chem. Phys. Lett. 140, 306 (1987).

LAWRENCE BERKELEY LABORATORY  
TECHNICAL INFORMATION DEPARTMENT  
UNIVERSITY OF CALIFORNIA  
BERKELEY, CALIFORNIA 94720